

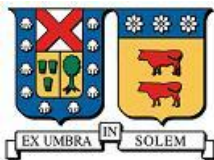
2018

THE LEPTOQUARK HUNTER'S GUIDE AND THE DARK VECTOR DOUBLET MODEL

DIAZ SAEZ, BASTIAN JAIME

<https://hdl.handle.net/11673/47784>

Repositorio Digital USM, UNIVERSIDAD TECNICA FEDERICO SANTA MARIA



Universidad Técnica Federico Santa María.
Departamento de Física.

The Leptoquark Hunter's Guide and the Dark Vector Doublet Model

Bastián Díaz Sáez
Advisor: Alfonso Zerwekh

A thesis submitted in partial fulfillment for the degree of Doctor
in Science, Universidad Técnica Federico Santa María.

November 2018

THESIS TITLE:

THE LEPTOQUARK HUNTER'S GUIDE AND THE DARK VECTOR
DOUBLET MODEL

AUTHOR:

BASTIÁN DÍAZ SÁEZ

A thesis submitted in partial fulfillment for the degree of Doctor
in Science, Universidad Técnica Federico Santa María.

EXAMINATION COMMITTEE:

Dr. Alfonso R. Zerwekh (UTFSM)

Dr. Claudio Dib V. (UTFSM)

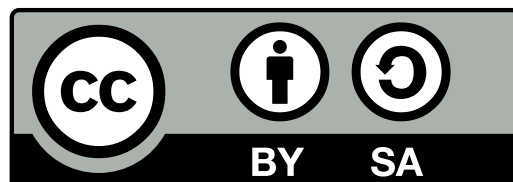
Dr. Diego Aristizabal (UTFSM)

Dr. Marco Aurelio Diaz (PUC)

November 23, 2018

a mi abuela Ema

This work is licensed under a [Creative Commons Attribution-ShareAlike 4.0 International License](https://creativecommons.org/licenses/by-sa/4.0/)



Abstract

The purpose of the first work is to point out that a model-independent search strategy covering all possible leptoquarks is possible and has not yet been fully exploited. To be systematic we organize the possible leptoquark final states according to a *leptoquark matrix* with entries corresponding to nine experimentally distinguishable leptoquark decays: any of {light-jet, b-jet, top} with any of {neutrino, $e/\mu, \tau$ }. The nine possibilities can be explored in a largely model-independent fashion with pair-production of leptoquarks at the LHC. We review the status of experimental searches for the nine components of the leptoquark matrix, pointing out which three have not been adequately covered. To demonstrate the utility of the leptoquark matrix approach we collect and summarize searches with the same final states as leptoquark pair production and use them to derive bounds on a complete set of Minimal Leptoquark models which span all possible flavor and gauge representations for scalar and vector leptoquarks

In the second work of this thesis, we explore an extension to the Standard Model which incorporates a vector field in the fundamental representation of $SU(2)_L$ as the only non-standard degree of freedom. This kind of field may appear in different scenarios such as Compositeness, Gauge-Higgs unification and extradimensional scenarios. We study the model in which a Z_2 symmetry is manifest, making the neutral CP-even component of the new vector field a vectorial dark matter candidate. We constraint the parameter space through LEP and LHC data, as well as from current dark matter searches. We find that the model is highly constrained but a small region of the parameter space can provide a viable DM candidate. Additionally we contrast our predictions on mono- Z , mono-jet and mono-Higgs production with the ones obtained in the well-studied inert Two Higgs Doublet Model. Finally, comment on the implications of perturbative unitarity are presented.

Acknowledgements

Agradezco a todas aquellas personas que me inspiraron y ayudaron en todo este largo proceso del doctorado en física. Parto agradeciendo a mi tutor Alfonso Zerwekh y a mi amigo Felipe Rojas, quienes siempre se mostraron abiertos a ayudarme y a discutir en lo que respecta a nuestros intereses científicos. Agradecer a Jaime y Gloria, mis padres, quienes fueron, son y serán pilares fundamentales en mi vida. Agradezco a mis hermanos nico, nacho y a toda mi familia. Agradezco a Camila Rosas por su apoyo fundamental en los primeros años de esta etapa. A mis colegas y amigos Yolbeiker, Sebastián Norero, Bernardo Fierro, Sebastián Tapia, Cristobal Corral, Pedro Allende, Michael Sanhueza, Francisco Alvarado y Nicolás Pérez. No puedo olvidar a mi hermandad, que siempre está en mi corazón. Finalmente, agradezco a Andrea León, por su incondicionalidad y total apoyo este último tiempo.

La presente tesis fue financiada parcialmente por la Comisión Nacional de Investigación científica y tecnológica CONICYT, Chile, bajo el proyecto No. 21130648 y a la Dirección General de Investigación , Innovación y Postgrado DGIIIP, UTFSM.

Contents

1	Leptoquarks	1
1.1	Introduction	1
1.2	Scalars and Vectors LQs	2
1.3	LQ matrix	4
1.4	Minimal Leptoquark Models	5
1.4.1	Cross section multiplicity and non-trivial branching fractions	6
1.5	Upper bounds on MLQs models	7
1.5.1	$\nu j, \nu b$ and νt	7
1.5.2	eb and μb	9
1.5.3	τj	10
1.6	Conclusions	10
2	Introduction to Dark Matter	11
2.1	Astrophysical Evidence	11
2.2	Standard Cosmology	14
2.3	Standard Model of particle Physics	15
3	Particle Dark Matter	19
3.1	Cold Dark Matter and the WIMP paradigm	19

3.2	Dynamic in the Early Universe	20
3.2.1	The Boltzmann equation	21
3.2.2	Dark Matter Freeze-out	22
3.2.3	Including coannihilations	25
3.3	Dark Matter detection	26
3.3.1	Direct Detection	26
3.3.2	Indirect detection	30
3.3.3	Collider searches	31
4	Dark Matter Models	35
4.1	Theoretical DM Frameworks	35
4.2	Dark Vector Dark Matter	40
5	Experimental constraints	45
5.1	LEP limits	45
5.2	LHC data	46
5.2.1	$H \rightarrow \gamma\gamma$	46
5.2.2	Invisible Higgs decay	49
5.3	Relic Density constraints	50
5.4	Direct Detection limits	52
6	Dark matter phenomenology	55
6.1	Parameter Space Scan	55
6.2	Vector Dark Matter as the only source	57
6.3	Dark matter production at the LHC	59
7	Conclusions	63

A Inert Two Higgs Doublet Model	65
B Vector fields and polarizations	67
C Partial wave amplitudes	69
Bibliography	77

Leptoquarks

1.1 Introduction

Leptoquarks (LQ) are hypothetical particles which couples to a lepton and a quark. They have both color and electric charge, then naturally coupling to gluons. Also they can have weak charges. They appear naturally in different SM extensions: GUT, SUSY with RPV, Technicolor and Quark and lepton compositeness. Further, there is additional motivation for LQs from B meson decays anomalies observed, which could be explained in models with LQs of TeV scale masses. There are many leptoquarks types. In Fig. 1.1 we show a classification following our notation, BRW [1] and from the PDG book [2]. In view of the amazing amount of LQ models,

Scalar LQ	$(SU(3), SU(2))_Y$	BRW	PDG	Vector LQ	$(SU(3), SU(2))_Y$	BRW	PDG
QL triplet	$(3, 3)_{-1/3}$	S_3	S_1^\dagger	$Q^\dagger L$ triplet	$(\bar{3}, 3)_{-2/3}$	U_3	V_1^\dagger
QL singlet	$(3, 1)_{-1/3}$	S_1	S_0^\dagger	$Q^\dagger L$ singlet	$(\bar{3}, 1)_{-2/3}$	U_1	V_0^\dagger
$U^c L$	$(\bar{3}, 2)_{-7/6}$	R_2	$S_{1/2}^\dagger$	$U^{c\dagger} L$	$(3, 2)_{1/6}$	\tilde{V}_2	$\tilde{V}_{1/2}^\dagger$
$D^c L$	$(\bar{3}, 2)_{-1/6}$	\tilde{R}_2	$\tilde{S}_{1/2}^\dagger$	$D^{c\dagger} L$	$(3, 2)_{-5/6}$	V_2	$V_{1/2}^\dagger$
QE^c	$(3, 2)_{7/6}$	R_2	$S_{1/2}^\dagger$	$Q^\dagger E^c$	$(\bar{3}, 2)_{5/6}$	V_2	$V_{1/2}^\dagger$
$U^c E^c$	$(\bar{3}, 1)_{1/3}$	S_1	S_0^\dagger	$U^{c\dagger} E^c$	$(3, 1)_{5/3}$	\tilde{U}_1	\tilde{V}_0^\dagger
$D^c E^c$	$(\bar{3}, 1)_{4/3}$	\tilde{S}_1	\tilde{S}_0^\dagger	$D^{c\dagger} E^c$	$(3, 1)_{2/3}$	U_1	V_0^\dagger
QN^c	$(3, 2)_{1/6}$	\tilde{R}_2	–	$Q^\dagger N^c$	$(\bar{3}, 2)_{-1/6}$	\tilde{V}_2	–
$U^c N^c$	$(\bar{3}, 1)_{-2/3}$	\tilde{S}_1	–	$U^{c\dagger} N^c$	$(3, 1)_{2/3}$	U_1	–
$D^c N^c$	$(\bar{3}, 1)_{1/3}$	S_1	–	$D^{c\dagger} N^c$	$(3, 1)_{-1/3}$	\tilde{U}_1	–

FIGURE 1.1: Minimal leptoquark models (MLQ) classified according to their charges under the SM gauge group.

the goal of our work is the following: to provide a simple organizing principle which makes it straightforward to systematically search for all possible leptoquarks. The idea is that we identify a minimum set of independent final states which must be searched for.

We divide the work in two parts. In the first part we introduce the LQ matrix and show that bounds on the cross sections into each of the 9 final states of the matrix are both efficient and sufficient for searching for all possible LQs. In second one we demonstrate the utility of this approach. We collect the best currently available cross section bounds from LHC searches organized by which element of the LQ matrix they cover and use them to put bounds on a complete set of “Minimal Leptoquark” (MLQ) models. The MLQs include both scalar and vector LQs with all possible flavor, charge and isospin quantum numbers.

1.2 Scalars and Vectors LQs

In this section we summarize some results between scalar and vector LQs: pair-production at the LHC, and the efficiencies from kinematical cuts (from ATLAS and CMS).

Leptoquark Pair production

The leading Feynman diagrams contributing to the LQ pair-production cross section are shown in Fig. 1.2. The gluon-gluon-LQ coupling is fixed by $SU(3)_c$ gauge symmetry. The vector case has a subtlety related to unitarity of theories with massive vectors. A consistent theory must have additional states beyond the LQ with masses not too far above the LQ mass. In the plot we show the contribution to LQ pair-production due to the intermediation of a massive gluon g' . Note that its contribution below 2 TeV is very small, then allowing to neglect it in the leading Feynman diagrams.

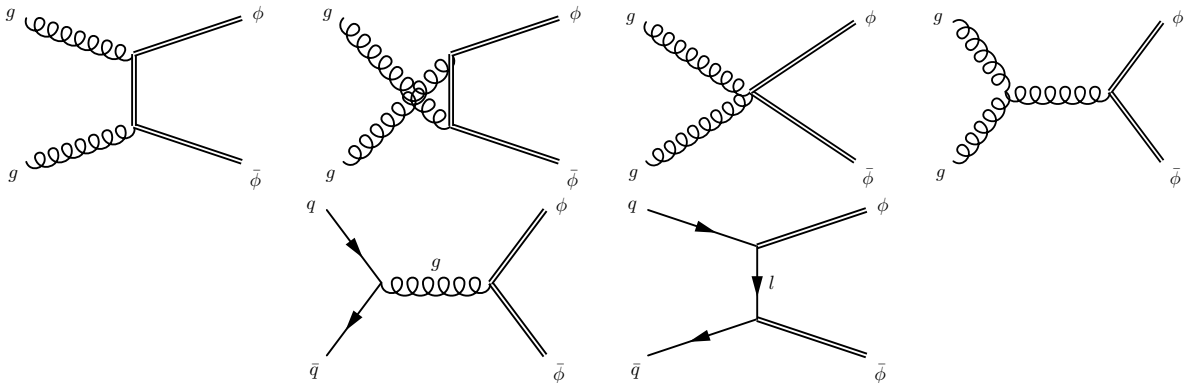


FIGURE 1.2: Diagrams for leptoquark pair production: gluon-initiated (upper row), quark-initiated (lower-left), and diagram proportional to the square of the leptoquark-lepton-quark coupling, λ^2 (lower-right).

In Fig. 1.3 we show the production cross section of a pair of leptoquarks. The red and blue cross section curves will be called the fiducial cross sections: σ_s and σ_v , for the scalar and vector LQ, respectively. The leptoquark pair production is almost model-independent, because QCD gluon-gluon-LQ couplings are expected high enough in comparison to the perturbative value for the free λ couplings. On the other hand, if the free coupling is increased enough to make a difference for pair production it also contributes to single LQ production at the same order in λ and single production will yield a stronger limit.

Efficiencies between scalars and vectors

For experimentalists, the signal under study can depend on many properties such as the spin, mass, charge, etc. We show that the efficiency is almost the same for scalar and vector LQs; The signal efficiency only depends on the LQ mass. The basic reason for this model independence is easy to understand: current LQ bounds already require masses well above 500 GeV and center of mass energies in excess of 1 TeV. Thus leptoquarks are produced with only moderate

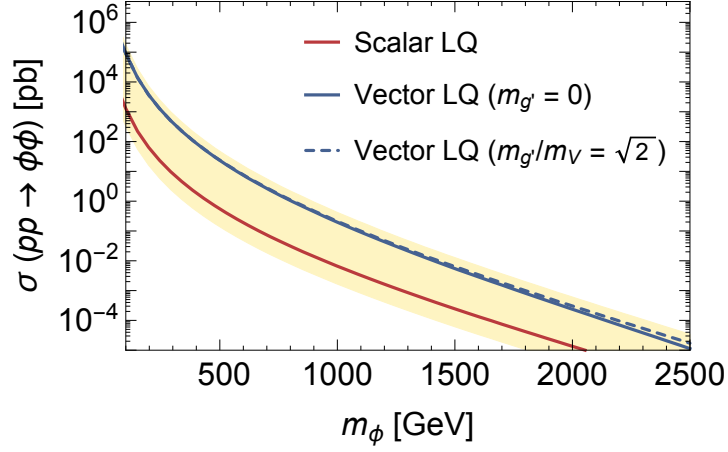


FIGURE 1.3: Pair-production cross section of LQs. Predictions are leading order with K -factors for scalar S and vector V leptoquarks. The cream band is explained in a later section.

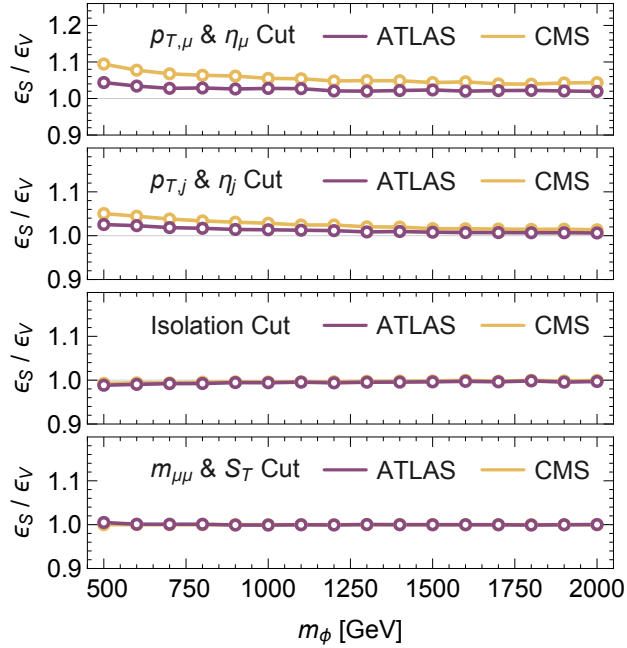


FIGURE 1.4: Ratios of signal efficiencies ϵ_S/ϵ_V for pair-produced scalar and vector LQs with various masses. The LQ decays are to muons and jets. The panels show the relative efficiencies of a series of selection cuts from recent ATLAS and CMS analyses.

boosts. Furthermore they two-body-decay directly to SM particles, yielding highly energetic widely separated SM particles with approximately isotropic distributions. Thus signal efficiencies for standard kinematic cuts are high and only very weakly dependent on any details of the LQ model other than the LQ mass (see Fig. 1.4).

1.3 LQ matrix

Let us think in the possible fermion final states at the LHC. All the light quarks, i.e. u, d, c, s and their antiparticles, all they leave the same trace at the detector, a light jet j . With b -tagging is possible to recognize a jet coming from a b -quark with high accuracy. The t -quark has its own family of traces. Then, we have just three possible signatures from the quark sector: j , b -jet and t -quark. In the leptonic side we use the following criteria. Light leptons, e^\pm, μ^\pm , have similar search strategies, then we consider all those leptons as a unique trace: l, τ^\pm and neutrinos (missing energy) are treated as different and independent final states.

Therefore, we arranged all these LQ final states into a 3×3 matrix which we call the “leptoquark final state matrix”, or simply “LQ matrix” (see Fig. 1.5).

	j	b	t
v			
ℓ			
τ			

FIGURE 1.5: *The Leptoquark Matrix.*

Possible LQ final states

Let us consider the easiest case: the LQ couples just to unique quark-lepton bilinear ql , then the decay to the LQ anti-LQ pair is also unique to the “symmetric” final state $(lq)(\bar{l}\bar{q})$. However, when LQs have multiple decay channels then LQ pair production also produces “asymmetric” final states which are not covered by the classification in terms of a single 3×3 matrix.

$$\begin{aligned} \text{symmetric :} & \quad (lq)(\bar{l}\bar{q}) + (l'q')(\bar{l}'\bar{q}') \\ \text{asymmetric :} & \quad (lq)(\bar{l}'\bar{q}') + (l'q')(\bar{l}\bar{q}) \end{aligned}$$

The two symmetric ones are contained in the LQ matrix classification, the asymmetric ones are not. But here is the point: all LQ which produce asymmetric final states necessarily also produce symmetric final states. Therefore the symmetric final states are sufficient to search for all possible leptoquarks. Symmetric final states can be represented by the LQ matrix.

Then the branching fraction to the quark-lepton pair with the largest coupling lq will dominate the decays, and the branching fraction to the symmetric state $(lq)(\bar{l}\bar{q})$ will be largest in most of the cases.

There are some interesting contrary case to the latter. For example, consider the $SU(2)_{weak}$ singlet scalar leptoquark. It couples to the $SU(2)_{weak}$ doublets q_L and l_L , both of the first generation. The possible four possible final states are $(\nu d)(\bar{\nu}\bar{d}) + (e^-u)(e^+\bar{u}) + (\nu d)(e^+\bar{u}) + (e^-u)(\nu\bar{d})$, each with 25% branching fraction. Here one can use the symmetric LQ matrix final states $(e^-j)(e^+j)$ and $jj\cancel{E}$. The other non-symmetric channels can not be studied with the LQ matrix: $(e^+j)(j\cancel{E})$ and $(e^-j)(j\cancel{E})$. However, even in this case where no single symmetric final state dominates the “easiest” and likely most sensitive search is the symmetric search for $(e^-j)(e^+j)$.

On the other hand, we have done a study for all the experimental searches that has been carried for the final states appearing in the LQ matrix. In Fig. 1.6 we resume all the information we got from ATLAS and CMS searches. The green slots represent the experimental searches where it is possible to get a cross section times branching fraction upper bound on that specific final state. In yellow there is only a lower mass bound on a particular squark model which only allowed us to obtain recast estimates for other models in this channel. Finally, in white are the channels where we did not find any upper bound.

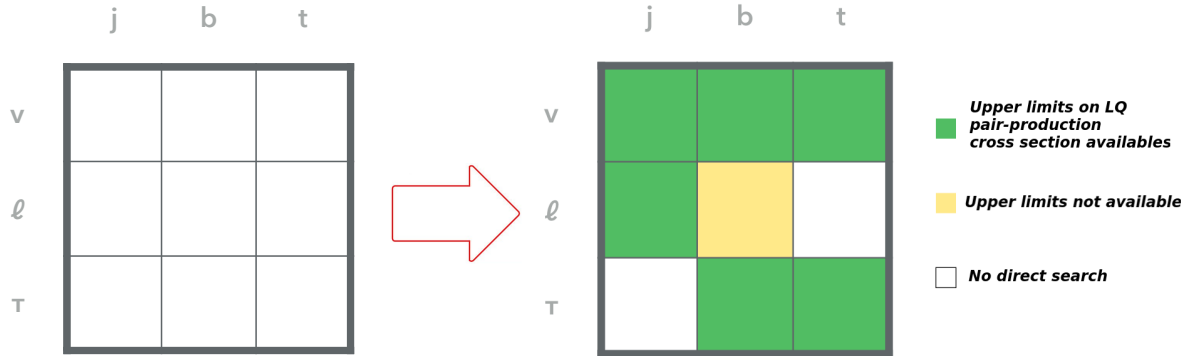


FIGURE 1.6: Summary of the current status of LQ searches at LHC after Runs 1 and 2.

1.4 Minimal Leptoquark Models

The definition of the minimal LQ models is as the follows: each model has one LQ in a single $SU(3)_c \times SU(2)_L \times U(1)_Y$ representation coupling to only one SM lepton-quark fermion bilinear. For each MLQ model we then obtain the lower bound on the mass of the MLQ by comparing the predicted cross section times branching fraction into LQ final states with the upper bound from experiment. To do so we need to determine the cross section times branching fraction into possible symmetric final states for each MLQ.

Let us see the possible MLQ. One generation of fermion fields is

$$Q, U^c, D^c, L, E^c, N^c,$$

where Q and L are the left-handed fields, and the rest of them are right-handed¹. Then, the scalar and vector LQ couple to quark-lepton bilinear in the following way

$$S(\mathbf{QL}) \quad \text{and} \quad V^\mu(\mathbf{Q}\bar{\sigma}_\mu\mathbf{L}), \quad (1.1)$$

where $\mathbf{Q} \in Q, U^c, D^c$ and $\mathbf{L} \in L, E^c, N^c$. $\bar{\sigma}_\mu$ is a vector of 2×2 matrices which contracts the LQ vector index with the fermion spinors. For both scalars and vectors there are 3×3 different possibilities (before considering generation number). Considering the three fermion families, the number of possible MLQ models is 162: $3 \times 3 \times 3 \times 3 \times 2$. We are defining the fields in the mass eigenstates for the quarks and charged leptons. Examples of MLQs models are: $Q_1 L_2$, $Q_3 N_1^c$, $Q_1^{c\dagger} E_2^c$, $Q_3 L_3$ singlet, etc.

1.4.1 Cross section multiplicity and non-trivial branching fractions

In some LQ models can be produced multiple LQs. Additionally, a given LQ can decay to multiple final states. Therefore, taking into account that fact, the total cross section for an specific final state will be given by

$$\sigma(pp \rightarrow LQ\bar{L}\bar{Q} \rightarrow \text{final state}) = \mu \times \sigma_f, \quad (1.2)$$

where σ_f is the fiducial cross section, either scalar or vector, and we define the multiplicity factor as

$$\mu = \sum_i Br(LQ_i\bar{L}\bar{Q}_i \rightarrow \text{final state}), \quad (1.3)$$

where the sum runs over all the LQs in the model which can decay to that final state. μ may be greater than 1 when multiple LQs are produced and less when branching fractions into the final state are nontrivial.

For example, consider the $SU(2)_{weak}$ doublet LQ which couple to the first family of quarks and to electron (positron): $Q_1 E_1^c$. One LQ component couple to (ue^+) , and the another one to (de^+) . Then, the multiplicity factor for $(e^+j)(e^-j)$ is

$$\begin{aligned} \mu &= \sum_i Br(LQ_i\bar{L}\bar{Q}_i \rightarrow (e^+j)(e^-j)) \\ &= Br(LQ_1\bar{L}\bar{Q}_1 \rightarrow (e^+j)(e^-j)) + Br(LQ_2\bar{L}\bar{Q}_2 \rightarrow (e^+j)(e^-j)) = 2. \end{aligned}$$

Then

$$\sigma(pp \rightarrow LQ\bar{L}\bar{Q} \rightarrow (e^+j)(e^-j)) = \mu \times \sigma_f = 2 \times \sigma_s.$$

therefore implying that the cross section for this final state in this model is twice the fiducial cross section.

Let us see another example in which the branching fraction is non-trivial and where the isospin predicts symmetric final states. Consider the scalar isospin singlet MLQ model which couple to the quark third generation and to the first lepton generation: $(U_3 E_1)$. The possible final states is

$$\frac{1}{4} \left[(e^-t)(e^+\bar{t}) + b\bar{b}\cancel{E} + (e^-t)\bar{b}\cancel{E} + (e^+\bar{t})b\cancel{E} \right] \quad (1.4)$$

¹i.e. $Q = (u_L, d_L)$. U^c and D^c are the charge conjugates fields. For example, $D^c = i\sigma_2 b_R^*$.

where the 1/4 indicates that each final state has branching fraction 25%. Again, we focus only on the symmetric case because it does not have neutrinos and is usually more sensitive than the asymmetric one:

$$\sigma(pp \rightarrow LQL\bar{Q} \rightarrow (e^-t)(e^+\bar{t})) = \mu \times \sigma_f = 0.25 \times \sigma_s.$$

In the literature this case is sometimes called $\beta = 1/2$ because the LQ has two different decays with branching fractions $Br \equiv \beta = 1/2$. In the paper you can find more examples.

We summarize all possible μ -factors in Table 1.1 for different MLQ model contributing to the LQ matrix final state.

TABLE 1.1: μ -factors for production and decay $\sigma(pp \rightarrow LQ\bar{L}Q \rightarrow (lq)(\bar{l}\bar{q}))$ in different scalar (upper table) and vectors (lower table) MLQ models. Rows correspond to different final states whereas columns correspond to different MLQ models. A “ \times ” entry indicates that that MLQ model does not contribute to the final state.

$pp \rightarrow SS \rightarrow (lq)(\bar{l}\bar{q})$	QL triplet	QL singlet	U^cL	D^cL	QE^c	U^cE^c	D^cE^c	QN^c	U^cN^c	D^cN^c
(νj)	1.25	0.25	1	1	\times	\times	\times	2	1	1
(νb)	0.25	0.25	\times	1	\times	\times	\times	1	\times	1
(νt)	1	\times	1	\times	\times	\times	\times	1	1	\times
$(ej), (\mu j), (\tau j)$	1.25	0.25	1	1	2	1	1	\times	\times	\times
$(eb), (\mu b), (\tau b)$	1	\times	\times	1	1	\times	1	\times	\times	\times
$(et), (\mu t), (\tau t)$	0.25	0.25	1	\times	1	1	\times	\times	\times	\times
$pp \rightarrow VV \rightarrow (lq)(\bar{l}\bar{q})$	$Q^\dagger L$ triplet	$Q^\dagger L$ singlet	$U^{c\dagger}L$	$D^{c\dagger}L$	$Q^\dagger E^c$	$U^{c\dagger}E^c$	$D^{c\dagger}E^c$	$Q^\dagger N^c$	$U^{c\dagger}N^c$	$D^{c\dagger}N^c$
(νj)	1.25	0.25	1	1	\times	\times	\times	2	1	1
(νb)	1	\times	\times	1	\times	\times	\times	1	\times	1
(νt)	0.25	0.25	1	\times	\times	\times	\times	1	1	\times
$(ej), (\mu j), (\tau j)$	1.25	0.25	1	1	2	1	1	\times	\times	\times
$(eb), (\mu b), (\tau b)$	0.25	0.25	\times	1	1	\times	1	\times	\times	\times
$(et), (\mu t), (\tau t)$	1	\times	1	\times	1	1	\times	\times	\times	\times

1.5 Upper bounds on MLQs models

In this section we constraint the LQs masses from each MLQ model following the leptoquark matrix. In the paper [3] you will find all the references of ATLAS and CMS papers.

1.5.1 $\nu j, \nu b$ and νt

Searches for pair-produced scalar LQs decaying into $(\nu j)(\nu j)$, $(\nu b)(\nu b)$ and $(\nu t)(\nu t)$ final states are identical to those for pair-produces squarks. In Fig. 1.7 we show diagrammatically the equivalence of the search for the case of LQs and \tilde{b} squarks pair-production. This decay is identical only in the limit in which the neutralino $\tilde{\chi}_1^0$ is taken to be massless. Thus, constraints on squarks can be directly applied to $S_{\nu q}$ and viceversa. Such a translation has already been performed by ATLAS. Immediately we obtain the strongest 95% C.L. limits by applying squark bound from CMS Runs 2 analyses, $m_{S_{\nu j}} \geq 1.05$ TeV, $m_{S_{\nu b}} \geq 1.175$ TeV, and $m_{S_{\nu t}} \geq 1.07$ TeV.

In order to recast the limits to any MLQ model, we digitize the temperature plot for the observed 95% C.L. upper limit on the light squark pair production cross section from searches at CMS, setting neutralino mass to zero. In Fig. 1.8 we show the digitized cross section limits as

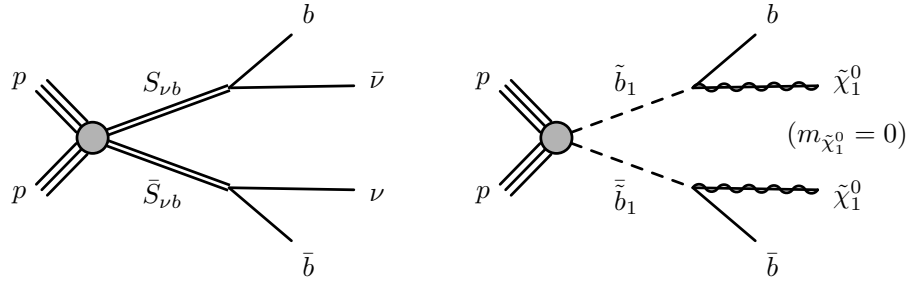


FIGURE 1.7: Diagrams for the process $pp \rightarrow S_{\nu b} \bar{S}_{\nu b} \rightarrow (b\bar{\nu})(\bar{b}\nu)$ (left) and the corresponding SUSY process $pp \rightarrow \tilde{b}_1 \tilde{b}_1 \rightarrow (b\tilde{\chi}_1^0)(\bar{b}\tilde{\chi}_1^0)$ (right). For massless neutralinos the final-states and kinematic distributions of the two processes are identical. Similar identifications can be made for other $S_{\nu q}$ and squark searches. Here the “1” subscripts are the usual SUSY notation for lightest b-squark and lightest neutralino.

the black solid curve. The colored lines in the same plot show the theoretical cross sections of different MLQs that can decay into $(\nu j)(\nu j)$ final states. The curves are labeled with the cross sections given in terms of the μ -factor times the relevant fiducial cross section, σ_S or σ_V , for scalar or vector LQs respectively. The intersects (dotted black lines) of the cross section curves with the experimental bound correspond to the lower mass bounds obtained in the different models. We obtain the bounds 630 GeV, 1 TeV, 1.1 TeV, and 1.2 TeV for scalar leptoquarks with μ -factors of 0.25, 1, 1.25, and 2, respectively, and 1.4 TeV and 1.7 TeV for vector leptoquarks with μ -factors of 0.25 and 1, respectively.

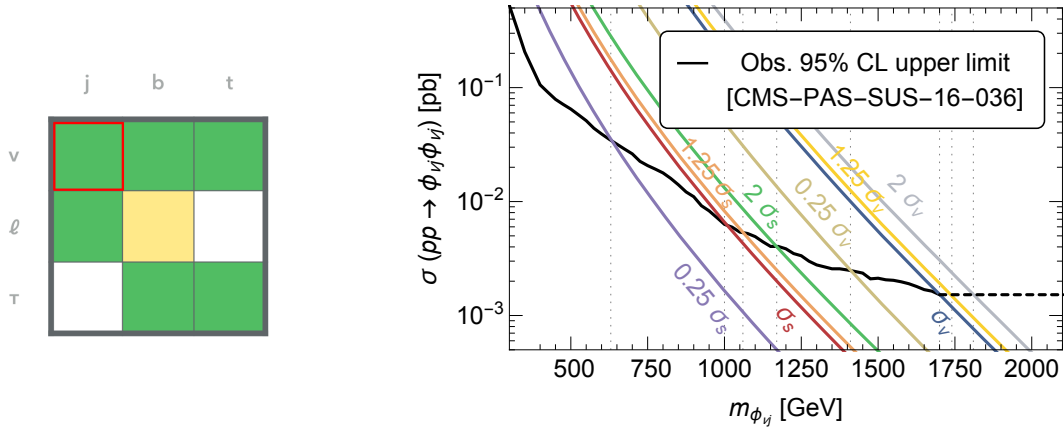


FIGURE 1.8: (left) Bounds on scalar and vector MLQs which decay into $(\nu j)(\nu j)$ final states. (right) Corresponding slot in the LQ-matrix.

	$U^c L, D^c L, U^c N^c, D^c N^c$	$Q N^c$	$Q L$ triplet	$Q L$ singlet
$S_{\nu j}$	$\times 1$	$\times 2$	$\times 1.25$	$\times 0.25$
σ_{prod}				
$m_{S_{\nu j}}$	≥ 1 TeV	≥ 1.2 TeV	≥ 1.1 GeV	≥ 630 GeV
	$U^{c\dagger} L, D^{c\dagger} L, U^{c\dagger} N^c, D^{c\dagger} N^c$	$Q^\dagger N^c$	$Q^\dagger L$ triplet	$Q^\dagger L$ singlet
$V_{\nu j}$	$\times 1$	$\times 2$	$\times 1.25$	$\times 0.25$
σ_{prod}				
$m_{V_{\nu j}}$	≥ 1.7 TeV	$(\geq 1.8$ TeV)	$(\geq 1.75$ TeV)	≥ 1.4 TeV

FIGURE 1.9: 95% C.L. lower limit on the mass of scalars (above) and vectors (below) from MLQs.

The CMS search stopped at 1.7 TeV and therefore we cannot obtain reliable experimental bounds on heavier leptoquark candidates. To get an estimate, we extrapolated the experimental

bound on the cross sections as independent of LQ mass for masses larger than 1.7 TeV (shown as the black dotted line). It seems reasonable to guess that the cross section limit flattens out for large LQ masses because signal efficiencies from very heavy LQs approach saturation. This allows us to recast bounds on vector leptoquarks of 1.75 TeV and 1.8 TeV for μ -factors of 1.25 and 2 respectively. Referring to the row labeled $S_{\nu j}$ and $V_{\nu j}$ in 1.1 we can then associate the mass bounds corresponding to different μ -factors to the different MLQ models. These bounds are summarized in the Fig. 1.12. Mass bounds in parenthesis are estimated bounds obtained using our extrapolated experimental cross section limits. Mass bounds without parenthesis are rigorous, they rely only on the cross section bounds published by the experiments.

1.5.2 eb and μb

To constraint the MLQs models we use the SUSY with RPV searches data. The final-state signature and kinematic distributions of pair-produced squarks which decay via the Yukawa coupling $\tilde{d}^{c\dagger}QL$, where $\tilde{d}^{c\dagger}$ couple like a LQ, are identical to production and decay of scalar LQs. The process searched for is $pp \rightarrow \tilde{t}_1\tilde{t}_1$ where \tilde{t}_1 decays into the final states (eb) or (μb) with at least one b -tag. Then, we take the strongest bounds from ATLAS search at 13 TeV at the special points where the decays are 100% to (eb) or 100% to (μb) . S_{eb} and $S_{\mu b}$ are excluded up to 1.5 TeV and 1.4 TeV with 95% C.L., respectively. Additionally, we assume that the signals regions do not depend on the LQ mass for even heavier LQs. In Fig. 1.12 we show our extrapolation for a wide LQ masses, and in the Table 1.11 are shown the estimated bounds.

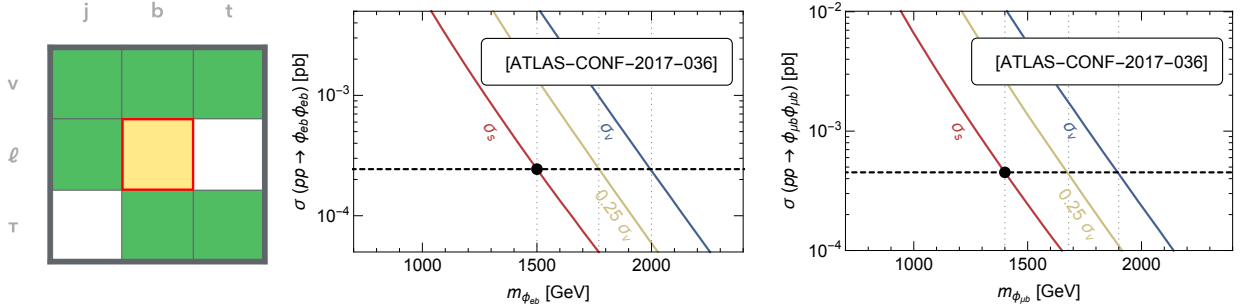


FIGURE 1.10: Bounds on scalar and vector MLQs which decay into $(eb)(eb)$ final states (left), $(\mu b)(\mu b)$ (middle). (right) Corresponding slot in the LQ-matrix.

		$D^c L, D^c E^c, Q E^c, (QL \text{ triplet})$
S_{eb}	σ_{prod}	$\times 1$
	$m_{S_{eb}}$	$\geq 1.5 \text{ TeV}$
$S_{\mu b}$	σ_{prod}	$\times 1$
	$m_{S_{\mu b}}$	$\geq 1.4 \text{ TeV}$

		$D^{c\dagger} L, D^{c\dagger} E^c, Q^\dagger E^c$	$Q^\dagger L \text{ triplet}, Q^\dagger L \text{ singlet}$
V_{eb}	σ_{prod}	$\times 1$	$\times 0.25$
	$m_{V_{eb}}$	$(\geq 2.0 \text{ TeV})$	$(\geq 1.8 \text{ TeV})$
$V_{\mu b}$	σ_{prod}	$\times 1$	$\times 0.25$
	$m_{V_{\mu b}}$	$(\geq 1.9 \text{ TeV})$	$(\geq 1.7 \text{ TeV})$

FIGURE 1.11: 95% C.L. limit on the LQs mass for different MLQ models.

1.5.3 τj

We are not aware of any dedicated searches for these final states. However, given the similarity of this final state with the well-covered $(\tau b)(\tau b)$ final state and given that SM backgrounds are small at large invariant masses we expect that a designated search will obtain bounds on leptoquarks masses which are comparable to those for the $(\tau b)(\tau b)$ case.

	j	b	t
v			
ℓ			
T			

FIGURE 1.12: Corresponding slot in the LQ-matrix. No dedicated search has been carried in this channel.

1.6 Conclusions

Leptoquarks occur in many new physics scenarios and could be the next big discovery at the LHC. We have focused on both scalar and vector LQ pair production, comparing their production cross sections and efficiencies at the LHC, founding big differences in their production cross section because of the LQs spin, and resulting in efficiencies very similar at ATLAS and CMS detector (in the worst cases less than 10% of differences). The searches were organized by what we called *the leptoquark matrix*: it leads to nine distinct final states to be searched for. We have found strong bounds from existing searches (6 of the 9 cases). The bounds on LQ masses oscillates between 600 GeV to around 2 TeV, where the highest masses bound are generally for vector LQs.

It is worth to motivate the experimental collaborations to publish bounds on the cross section times branching fraction as a function of LQ mass for each of these final states. We also note that even in the cases where cross section bounds as a function of mass have been published it would be useful if the search range could be extended as far as possible in LQ mass. We plead that experimenters publish bounds on leptoquark cross sections as functions of mass for as wide a range of leptoquark masses as possible. Such bounds are essential for reliable recasts to general leptoquark models.

For leptoquarks with large couplings single (and off-shell) production can become important and potentially yield stronger lower bounds on LQ masses. This is especially true when the large coupling is to first generation quarks with their large parton distribution functions. For LQs related to the recent hints for new physics from B meson decays the interesting range of couplings is $10^{-2} \leq \lambda \leq 1$. The LQ matrix is also convenient for organizing the possible single LQ production final states.

Introduction to Dark Matter

It is amazing the complexity and differences in the physics of the smallest and the biggest scales. On one hand, the physics of small things is governed by the rules of *quantum mechanics*, where the inherent probability and statistical behaviour is underlying all the microscopic phenomena. On the other hand, *general relativity* has been very successful guiding us in the discovery of many astrophysical phenomena, such as mercury perihelium, gravitational lensing and the recently discovered gravitational waves, and in the description of the evolution of our Universe. More surprisingly is the deep connection among the fundamental interactions of nature and laws that governs the macroscopic world. Therefore, it is tempting from the most fundamental level to answer some big-scale issues, such as the famous problem of *dark matter* (DM). Of course, other paths to address astrophysical problems has been proposed, such as Modified Newtonian Dynamics (MOND), and it is worth to explore all these possibilities too.

In this chapter we will review the main astrophysical and cosmological evidences of DM, along to present the main features of both Standard Models: Λ CDM model and Particle Physics one. From the latter, we will review the motivation for new physics at the Fermi-scale and how those proposals relates to the DM problem.

2.1 Astrophysical Evidence

In the 30's, the astronomer Fritz Zwicky did observations on the Coma Cluster¹, and he could infer through gravitational effects that something non-luminous (dark) would must to be in there. This inference was made because the galaxies in the cluster were moving too fast for the cluster to be bound together by the visible matter. Though the idea of DM would not be accepted for another fifty years, Zwicky wrote that the galaxies must be held together by some *dunkle materie* (dark matter). About 90% of the mass of the Coma cluster is believed to be in the form of DM.

Over the years, more data supported the existence of this new exotic kind of matter in another observations, even at different distances scales. In the following, we resume the different kind of observations supporting the evidence of DM²:

- **Galactic scale.** Stars in galaxies orbiting a common center move more rapidly than they must to. This is what is called *rotation curves*. Observing rotation curves usually exhibit

¹The Coma Cluster, also known as Abell 1656, is a large cluster of galaxies that contains over 1000 identified galaxies. The Cluster is at approximately 100 Mpc (321 million ly).

²There is additional evidence supporting DM both on subgalactic and inter-galactic scales. For a review of this see [4].

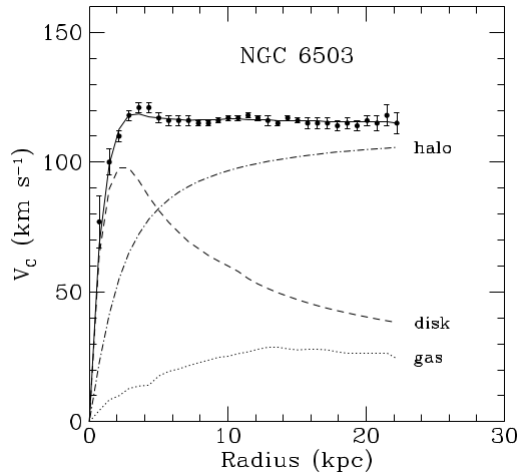


FIGURE 2.1: Dwarf spiral galaxy (NGC 6503) rotation curve located at 5.27 Mpc from the Milky way.

a characteristic flat behavior at large distances, i.e. our towards, and even far beyond, the edge of the visible disk (see Fig. 2.1). The fact that the velocity of the stars is approximately constant implies the existence of a spherical *halo* with mass and density obeying $M(r) \sim r$ and $\rho \sim 1/r^2$. The total amount of DM present in a galaxy is difficult to quantify since we do not know to what distances halos extend and there is no concordance on the DM distribution in the inner regions of the galaxy.

- **Cluster of galaxy scales.** As we mentioned above, the cluster galaxy velocities was the first evidence of DM (F. Zwicky). Furthermore, gravitational lensing is an effect which allows to infer the potential well and thus the mass of the cluster. For instance, the right-side pictures in Fig. 2.3 show the distortion of the light coming from the Abell and the MS2137.3-2353 clusters: the left-side of the figure shows the spectra in X-rays in which the gravitational lensing is not visible, while in the right side the lens is notorious). The other powerful evidence that we have at this scales is the two colliding cluster of galaxies, most known as Bullet Cluster.
- **Cosmological scales.** This evidence come from the information in the Cosmic Microwave Background (CMB). The WMAP analysis data have shown the abundance of baryon in the Universe to be $\Omega_b h^2 = 0.024 \pm 0.001$, a number which is consistent with the predictions from Big Bang Nucleosynthesis (BBN), $0.018 < \Omega_b h^2 < 0.023$, whereas the abundance of DM is $\Omega_{DM} h^2 = 0.14 \pm 0.02$. Additionally, besides the cosmological data from CMB, the three-dimensional matter power spectrum $P(k)$ through the Sloan Digital Sky Survey (SDSS) has used to complement the existence of DM in the Universe.
- **N-body simulations.** The most widely adopted approach to the problem of large-scale structure formation involves the use of N-body simulations. This has shown that the existence of *Cold Dark Matter* (CDM) in the Universe is indispensable for the structure formation in the earliest eras of the universe. In chapter 3 we will study in more details the origin and consequences of the CDM paradigm.

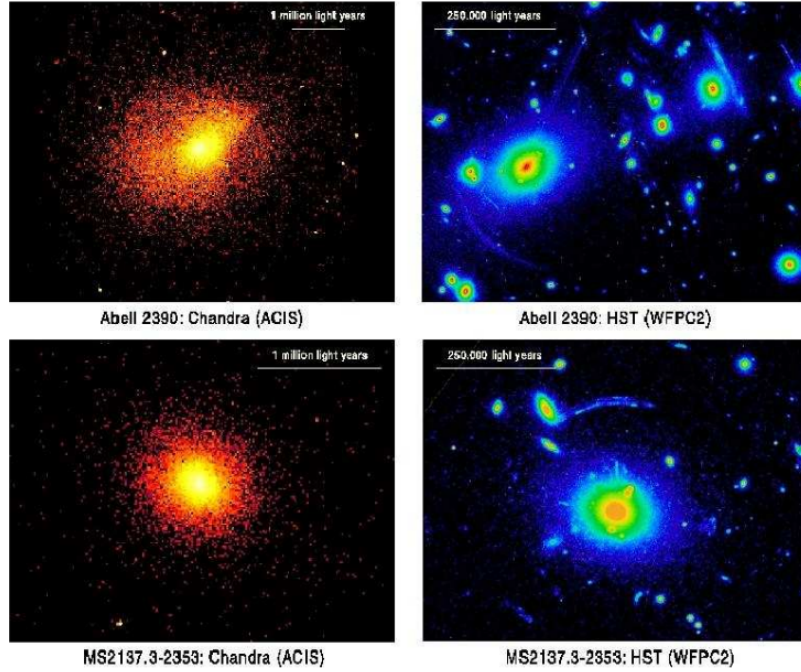


FIGURE 2.2: Chandra X-ray (left) and Hubble Space Telescope Wide Field Planetary Camera 2 optical (right) images of Abell 2390 ($z = 0.230$) and MS2137.3-2353 ($z = 0.313$) [5]. Note the clear gravitational arcs in the Hubble images.

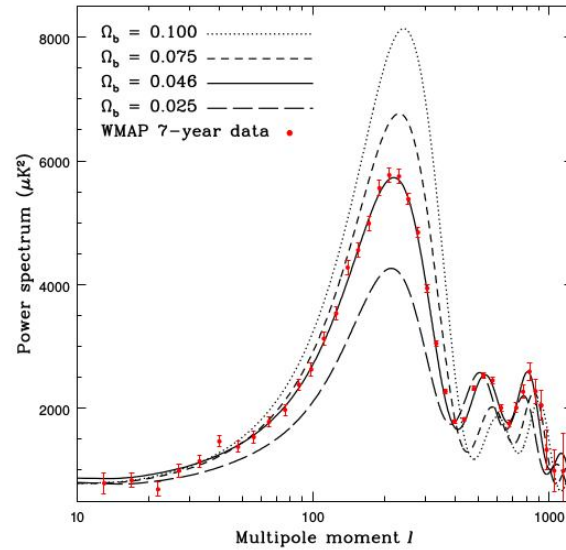


FIGURE 2.3: The power spectrum of the cosmic microwave background radiation temperature anisotropy in terms of the angular scale (or multipole moment). The data shown comes from the WMAP [6] and the dashed and pointed curves correspond to different barionic matter densities.

2.2 Standard Cosmology

The *Big Bang* scenario has become the paradigm of the modern cosmology. It describes the Universe as a system evolving from a highly compressed state existing around 10^{10} years ago. This picture has its roots in the discovery of Hubble's law from astronomical data, and though the decades it has evolved in complexity. The model has been very successful in the prediction of a lot of things, such as the abundance of elements, large scale structure, relic background radiation and many other properties of the Universe. The model is based on Einstein equations

$$R_{\mu\nu} - \frac{1}{2}g_{\mu\nu}R = 8\pi G_N T_{\mu\nu} - \Lambda g_{\mu\nu}, \quad (2.1)$$

where $R_{\mu\nu}$ and R are, respectively, the Ricci tensor and scalar (obtained by contraction of the Riemann curvature tensor). $g_{\mu\nu}$ is the metric tensor, G_N is Newton's constant, $T_{\mu\nu}$ is the energy-momentum tensor, and Λ is the so-called cosmological constant. This equation relates the geometry of the spacetime (left-hand side) to the energy-matter content (right hand-side) of the Universe.

To solve the Einstein equations one has to specify the symmetries of the problem. Based on observations at large distances, such as the Cosmic Microwave Background (CMB) or galaxy surveys at scales ~ 100 Mpc³, the Universe seems uniform: *homogenous* and *isotropic*. These two facts together are known as the *Cosmological Principle*, and are the starting point to solve Einstein equations. The immediate consequence of the cosmological principle can be expressed in the line element as

$$ds^2 = -dt^2 + a(t)^2 \left(\frac{dr^2}{1 - kr^2} + r^2 d\Omega^2 \right), \quad (2.2)$$

where $a(t)$ is the so called *scale factor* and k is a constant parametrizing the spatial curvature of the Universe. It can take the values $k = -1, 0, +1$, which corresponds to have a open, flat and closed Universe, respectively.

The Einstein equation can be solved with this metric, giving as a result the well-known Friedmann equation

$$H^2 = \frac{8\pi G_N}{3} \rho_{tot} - \frac{k}{a^2}, \quad (2.3)$$

where H is the Hubble parameter given by

$$H(t) \equiv \frac{\dot{a}(t)}{a(t)}, \quad (2.4)$$

and ρ_{tot} is the total average energy density of the universe. A recent estimate of the present value of $H_0 = 100h \text{ km s}^{-1} \text{ Mpc}^{-1}$, where h is a constant used to keep track of how uncertainties in H_0 propagate into other cosmological parameters, and its value is given by $h \sim 0.67 \pm 0.01$. A flat Universe ($k = 0$) corresponds to the following *critical density* today

$$\rho_{c,0} = \frac{3H^2}{8\pi G_N} \quad (2.5)$$

$$= 1.9 \times 10^{-29} h^2 \text{ grams cm}^{-3} \quad (2.6)$$

$$= 1.1 \times 10^{-5} h^2 \text{ protons cm}^{-3}. \quad (2.7)$$

³Spheres with diameters larger than ~ 100 Mpc centered in any place of the Universe should contain, roughly, the same amount of matter.

To see more explicitly the other cases of curvature depending of the value of the total density, we introduce the *parameter densities* Ω_i , which are defined as the density of some specie relative to the critical density:

$$\Omega_i(t) \equiv \frac{\rho_i(t)}{\rho_c(t)}. \quad (2.8)$$

It is also customary to define that $\Omega = \sum_i \Omega_i$. The Friedmann equation can be rewritten in terms of the total parameter density as

$$\Omega - 1 = \frac{k}{H^2 a^2}. \quad (2.9)$$

The sign of the spatial curvature of the Universe k is therefore determined by whether Ω is greater than, equal to, or less than one (see Table 2.1).

TABLE 2.1: Classification of cosmological models based on the value of the average density, ρ , in terms of the critical density ρ_c .

$\rho < \rho_c$	$\Omega < 1$	$k = -1$	open
$\rho = \rho_c$	$\Omega = 1$	$k = 0$	flat
$\rho > \rho_c$	$\Omega > 1$	$k = 1$	closed

Considering the different species in the Universe, i.e. radiation (r), matter (m), curvature (k) and dark energy (Λ), the Friedmann equation can be recast in the following way

$$\frac{H^2}{H_0^2} = \Omega_r a^{-4} + \Omega_m a^{-3} + \Omega_k a^{-2} + \Omega_\Lambda, \quad (2.10)$$

where we have used the conventional normalization for the scale factor $a_0 \equiv 1$ (today). Observations such as TypeIA supernovae, CMB and Large-scale structure have shown that the actual values for the species is⁴

$$|\Omega_k| < 0.01, \quad \Omega_r = 9.4 \times 10^{-5}, \quad \Omega_m = 0.32, \quad \Omega_\Lambda = 0.68. \quad (2.12)$$

The matter splits into 5% ordinary matter (barionic matter) and 27% dark matter:

$$\Omega_b = 0.05, \quad \Omega_c = 0.27. \quad (2.13)$$

Considering that the different species scales with a different power in the scale factor, it is possible to distinguish different epochs in the Universe dominated by only one source (see Fig. 2.4).

2.3 Standard Model of particle Physics

The Standard Model of elementary particles (SM) is a four-dimensional *Quantum Field Theory* (QFT) which includes all the forces, except gravity, and all the known elementary fermions:

⁴Sometimes these values are given considering the constant h defined above ($h \sim 0.67 \pm 0.01$). For example, for our purposes the most useful quantity is

$$\Omega_m h^2 = 0.1415 \pm 0.0019, \quad (2.11)$$

where $\Omega_b h^2 = 0.02226 \pm 0.00023$ and $\Omega_c h^2 = 0.1186 \pm 0.0020$.

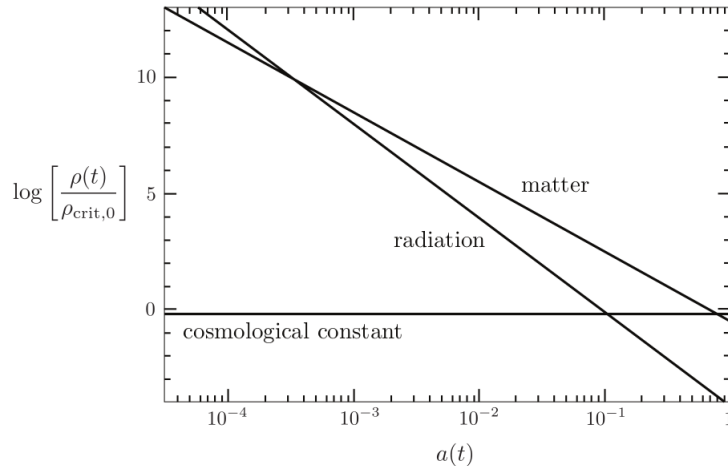


FIGURE 2.4: Evolution of the energy densities in the Universe as a function of the scale factor.

leptons and *quarks*. The model is based on $SU(3)_c \times SU(2)_L \times U(1)_Y$ gauge symmetry. The $SU(3)_c$ gauge group describes the gluon fields, which along with the quarks is known as *Quantum ChromoDynamics* (QCD). $SU(2)_L \times U(1)_Y$ is the *Electroweak gauge symmetry* (EW), and it contains the weak and electromagnetic mediators in a unified way. Both quarks as leptons may feel the EW interactions.

The inclusion of the Higgs field into the SM is motivated in order to have a consistent renormalizable and unitary QFT massive spin-1 fields (weak mediators). The parametrization of the mass acquisition by some of the electroweak gauge bosons is thorough of what is known as the *Higgs mechanism*. It undergoes through a phase transition, breaking spontaneously the electroweak symmetry of the theory by the vacuum expectation value of the neutral component of the Higgs field, realizing the following pattern

$$SU(3)_c \times SU(2)_L \times U(1)_Y \rightarrow SU(3)_c \times U(1)_Q. \quad (2.14)$$

This spontaneous symmetry breaking results in the generation of the massive W^\pm and Z gauge bosons as well as the massive scalar Higgs boson. Complementary, the scalar doublet can be used to generate almost all the fermion masses: *Yukawa sector*. In view of the lack of the counterpart right-chiral neutrino, it is not possible to include a mass term for it, remaining massless at tree level.

The electroweak scale

The Higgs mechanism has been very attractive for two reasons. The first one is that it is the minimal way to generate the masses for the weak force mediators in a renormalizable way. This minimality respects custodial symmetry, making the ρ -parameter very close to the unity, and making the electroweak radiative corrections to be allowed by the experimental data. The second important reason is that a light Higgs boson helps to unitarize the elastic scattering amplitudes of the gauge bosons at high energies ($E \gg M_W$). This is, the Higgs boson participates in the electroweak elastic scattering amplitudes at all levels in perturbation theory canceling the $\sim E^2$ grow energy behavior. This means that if the Higgs boson were not discovered, one would have expected a new strong dynamics at the TeV scale.

After EWSB, the tree level Higgs boson mass is related to the Fermi-scale (energy scale around 256 GeV) through

$$m_H = \sqrt{\lambda}v = \frac{\sqrt{\lambda}}{\sqrt{G_F\sqrt{2}}}. \quad (2.15)$$

Any quantum correction to m_H implies immediately a quantum correction on G_F . The problem with the Higgs mechanism appears when we think the SM valid perturbatively up to very high energies, let say near the Planck scale M_{Pl} . The Higgs boson mass is unstable under radiative corrections. This means that because there is no symmetry protecting the Higgs mass, the radiative corrections are additive. In fact, at one-loop level, the corrections to the Higgs mass are of the form $m_H^2 = m_0^2 + \delta m_H^2$, where

$$\delta m_H^2 = \left[\frac{1}{4} (9g^2 + 2g'^2) - 6y_t^2 + 6\lambda \right] \frac{\Lambda^2}{32\pi^2}, \quad (2.16)$$

and y_t is the top Yukawa coupling (we have neglected the contribution from lighter fermions), g and g' are the coupling constants of $SU(2)_L$ and $U(1)_Y$ gauge groups, and λ is the Higgs self-interaction parameter. We have assumed a common cut-off Λ to regulate the momentum integrals. Thus, the *natural* value of the Higgs mass is the cut-off Λ of the theory. In order for the EWSB scale v to be much lower than the cut-off (M_{Pl}) we need a delicate cancellation between this quantum correction and the bare parameters of the model: the bare parameters of the Higgs potential have to be adjusted to one part in $\sim 10^{15}$. This is a *fine-tuning problem*, and makes the theory “*unnatural*”.

Over the years, this naturalness problem has motivated the construction of many extensions to the SM, most of them based on two reasoning at the TeV scale: weakly-interacting Higgs model (e.g. Supersymmetry) and a new Strong Dynamics (e.g. Compositeness). Curiously, in most of this extensions a massive color-singlet neutral particle arises, making it a *dark matter candidate*. Therefore, it seems reasonable to link the expected new electroweak physics to the astrophysical problem of dark matter. In the next chapter we will develop the details of the WIMP paradigm and we will review through the Boltzmann equation how the decoupling of dark matter occurred in the early Universe, leading to the observed relic density today.

Particle Dark Matter

In this chapter we will review the basic particle physics paradigm which governs the dark matter (DM) problem: the Cold Dark Matter paradigm along one of the most popular candidates to be a DM particle, the *weakly interacting massive particle* (WIMP). We will derive the Boltzmann equation after some assumptions, giving rise to the WIMP miracle. After settled this framework, we will review the main features of the three dark matter experiments today: direct detection, indirect detection and collider experiments.

3.1 Cold Dark Matter and the WIMP paradigm

On quite general grounds, one expect the DM particle to be cold, it means that they must to be non-relativistic (and thus massive) since the universe was approximately one year old, otherwise, relativistic particles, such as Standard Model neutrinos, would exceed the escape velocity of clumping baryons and thus could not produce gravitational wells needed for structure formation. Numerical simulations of structure formation in the early universe have supported this fact, requiring non-relativistic (cold) dark matter at the epoch of structure formation. Additionally, DM must to be non-baryonic, i.e. carrying neither electric not color charges. Dynamical systems, such as cluster collisions, shows that dark matter basically does not interact at the astrophysical scales. This implies that the dark matter must to be weakly interacting, with the constraint $\sigma/m < 1.24 \text{ cm}^2\text{g}^{-1}$. The last general requisite is to be stable (long lived), with a lifetime exceeding the age of the universe. These set of ingredients (non-relativistic and with no electric/color charge) make what is called the Cold Dark Matter (CDM) paradigm. It is believed that approximately 84.54% of matter in the Universe is DM, with only a small fraction being the ordinary baryonic matter that composes stars, planets and living organisms.

Generally, DM relics are considered to be produced in the very early universe in two distinct ways: (i) thermal and (ii) non-thermal processes. The thermal production is the idea that DM was in thermal equilibrium with SM particles in the very beginning of the Universe, i.e., the reactions going from the dark sector to the standard model and back again were at equal rates. On the other hand, non-thermal production refers to processes taking place outside of the thermal equilibrium, and the resulting relics are called non-thermal relics. In the first class of processes, at some moment in the early universe the rate of the own expansion of the universe grew up to

¹Self-interacting DM with a cross section in the range $0.1 < \sigma/m < 10 \text{ cm}^2\text{g}^{-1}$ (scales of dwarf galaxies) can be very beneficial in order to alleviate the small scale structure problems. Two long-standing puzzles of the collisionless cold DM paradigm are "cusp-vs-core" and the "too-big-to-fail" problems. However, some of the methods and assumptions utilized to obtain these results have been questioned in the recent literature and the actual limit could be less stringent.

the level of the collision rates among the two kind of sectors and then happened what is known as freeze-out. This last idea means that from that moment until today, the comoving density of dark matter is constant. In the second case, the relic production can happen from boson field coherent motion or from out-of-equilibrium decays of heavier states. Typically, dark matter relics which were created from a thermal processes and decoupling of the rest of the particles in the early universe are said to be WIMPS (Weakly Interacting Massive Particle). This class of particles have a range of masses in the range between a few GeV and some TeV, and they interacts through the weak force only.

In what follows we will describe thermal equilibrium and the evolution of DM density in the early universe under some assumptions.

3.2 Dynamic in the Early Universe

The beginning of the universe is taught hotter and denser than today, and the amounts of DM particles and the rest of the plasma must have been in equal numbers: there was a thermodynamic equilibrium (through mechanisms like pair production or collisions interactions of other particles). This means the annihilation process of SM particles and DM particles happened in the same proportion as the reverse process. See left diagram of Fig. 3.1. The number of particles must have been so high that generated an environment where the amount of particles per second were destroyed was equal to the amount of particles were created.

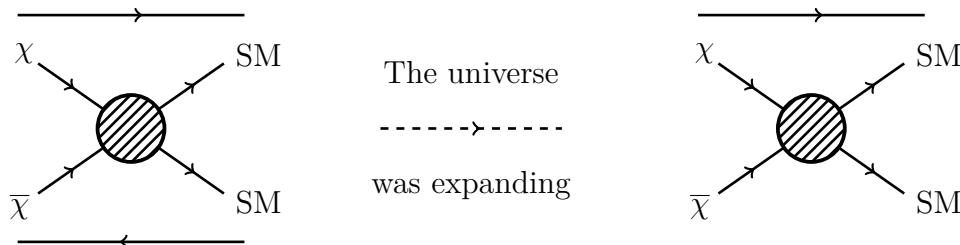


FIGURE 3.1: Scheme of the thermodynamic equilibrium in the early Universe.

However, as the Universe was expanding and cooled, the thermodynamics equilibrium was broken and two things occurred:

- The lightest particles did not had enough kinetic energy (thermal energy) to produce DM particles through interactions.
- The expansion of the universe started to dilute the number of particles doing less frequently the interaction between them.

Therefore, we can ask now, how did evolve the number of particles as the universe expand? The formal tool to describe the evolution beyond thermal equilibrium is the *Boltzmann equation*.

3.2.1 The Boltzmann equation

The first important quantity to consider in an expanding Universe is the number of galaxies per proper volume as measured by a comoving observer: $n(t)$. The only dependence of this quantity on time and not in the spatial directions is a consequence of the cosmological principle. We can start the analysis thinking in a Universe where the number of particles is conserved for a fixed volume ($V \propto a^3$). This implies that in an expanding Universe, the number density of particles is diluted with time ($n_i \propto a^{-3}$). Therefore, in the absence of interactions, the number density of particles evolves as

$$\frac{dn_i}{dt} + 3n_i \frac{\dot{a}}{a} = 0. \quad (3.1)$$

To include the effects of interactions we add a collision term to the r.h.s. of eq. (3.1)

$$\frac{1}{a^3} \frac{d(n_i a^3)}{dt} = C_i [\{n_j\}]. \quad (3.2)$$

The form of the collision term will depend specifically on the interaction process to be considered. Because the interaction between three particles is very unlikely, we can think of scattering and annihilation processes of two particles and simple particle decay. For example, let us consider the following process

$$1 + 2 \Leftrightarrow 3 + 4. \quad (3.3)$$

In this process, particles of species 1 and 2 annihilate each other to produce particles of species 3 and 4, and vice versa. For example, let us see how the number density of particles of species 1 changes in time. The rate of change of n_1 depends on how fast the particles are annihilated versus how fast they are being produced. This can be described in the following way

$$\frac{1}{a^3} \frac{d(n_1 a^3)}{dt} = -\alpha n_1 n_2 + \beta n_3 n_4 \quad (3.4)$$

The first term in the r.h.s. of eq. (3.4) describes the annihilation of particles and the second term describes the production process. We know from QFT that the annihilation term must be proportional to the cross section, but in this case the cross section may depend on the relative velocity v of particles 1 and 2. Therefore, the parameter $\alpha = \langle \sigma v \rangle$ is the thermally averaged cross section, where the bracket denotes the average over v . We can find the value of the parameter β considering the case when the system is in chemical equilibrium. When this happens the interaction term is zero, and β is

$$\beta = \alpha \left(\frac{n_1 n_2}{n_3 n_4} \right)_{\text{eq}}, \quad (3.5)$$

where n_i^{eq} is the equilibrium number density. The Boltzmann equation is

$$\frac{1}{a^3} \frac{d(n_1 a^3)}{dt} = -\langle \sigma v \rangle \left[n_1 n_2 - \left(\frac{n_1 n_2}{n_3 n_4} \right)_{\text{eq}} n_3 n_4 \right]. \quad (3.6)$$

It can be written in a simplified form when we suppose that $n_1 = n_2 = n$ and the species 3 and 4 are in equilibrium n_{eq}

$$\frac{dn}{dt} + 3Hn = -\langle \sigma v \rangle \left(n^2 - (n^{\text{eq}})^2 \right). \quad (3.7)$$

In order to understand the game between the abundance of some species in relation to others and the Universe expansion, we can rewrite this equation in terms of the abundances: $N_i = n_i/s$

(remember that the number of particles in a covolume is constant provided the interactions do not destroy nor created them). For example, let us trace the abundance of the specie 1, N_1 :

$$\frac{d \ln(N_1)}{d \ln a} = -\frac{\Gamma_1}{H} \left[1 - \left(\frac{N_1 N_2}{N_3 N_4} \right)_{\text{eq}} \frac{N_3 N_4}{N_1 N_2} \right]. \quad (3.8)$$

where $\Gamma_1 = n_2 \langle \sigma v \rangle$ ² is the interaction rate per particle, the fraction Γ_1/H represent the interaction efficiency and the parenthesis in the r.h.s of eq. (3.8) characterize the deviation from equilibrium. As long as $\Gamma \gg H$ the natural state of the system is chemical equilibrium (basically this measures if particles interact frequently enough or is the expansion of the universe so fast that particles never encounter each other). Under this scenario we consider a simple example: suppose we start with $N_1 \gg N_1^{\text{eq}}$ (while $N_i \sim N_i^{\text{eq}}, i = 2, 3, 4$). The r.h.s. of eq. (3.8) is negative, therefore particles of species 1 are being destroyed and N_1 is reduced towards the equilibrium value N_1^{eq} . By the other hand, if $N_1 \ll N_1^{\text{eq}}$, the r.h.s. of eq. (3.8) is positive, this means that particles of species N_1 are being created and N_1 is driven towards N_1^{eq} . In both cases the system tend to the chemical equilibrium. However, when $\Gamma < H$, this means the number of particles of specie 1 is not enough to interact with each other, the r.h.s. of eq. (3.8) is suppressed and the density of particles would *freeze-out* at this point turning into a constant relic density $N_1 = \text{constant}$. On the study of DM in early Universe we can observe the same type of evolution for relic abundance. In the next subsection we will study the freeze-out of DM in the early universe using the Boltzmann equation.

3.2.2 Dark Matter Freeze-out

To study of the evolution of the DM densities as the universe temperatures drops one must to make some assumptions about the nature of the DM particles. Considering this we will use the hypothesis of the WIMP as a candidate for DM. This framework states that the DM particles are massive and interacts very weakly to themselves and to the Standard Model particles. The first consequence of this is that the abundance of DM particles is traced to reactions which consider the interaction of just two DM particles. More than two DM particles interacting in the same vicinity is too unlikely³.

WIMPs were in close contact with the rest of the cosmic plasma at high temperatures, but then experienced freeze-out at a critical temperature T_f . The idea is to solve the Boltzmann equation for such a particle, determining the epoch of freeze-out and its relic abundance. We start the analysis considering that heavy DM particles X and their antiparticles \bar{X} annihilate each other to produce two lights SM particles ℓ and $\bar{\ell}$

$$X + \bar{X} \leftrightarrow \ell + \bar{\ell}. \quad (3.9)$$

Assuming that there is no asymmetry between DM particles and their antiparticles \bar{X} , we have $n_X = n_{\bar{X}}$. The second assumption is that the light particles are tightly coupled to the cosmic plasma, so that throughout the evolution of the system they maintain their equilibrium densities $n_\ell = n_\ell^{\text{eq}}$. The Boltzmann equation of the form (3.6) for the evolution of the number of WIMPs

²For a process of the form $1 + 2 \leftrightarrow 3 + 4$, we would write the interaction rate of species 1 as $\Gamma_1 = n_2 \langle \sigma v \rangle$, where n_2 is the density of the target species 2 and v is the average relative velocity of 1 and 2. The interaction rate of species 2 would be $\Gamma = n_1 \langle \sigma v \rangle$.

³In the SIMP (Strongly Interacting Massive Particles) paradigm processes such as $DM + DM + DM \leftrightarrow SM + SM$ are more likely to occur due to the high coupling among DM particles.

in a co-moving volume, where $N_X = n_X/s$ and $N_X^{eq} = n_X^{eq}/s$ is

$$\frac{dN_X}{dt} = -s\langle\sigma v\rangle \left[N_X^2 - (N_X^{eq})^2 \right]. \quad (3.10)$$

In the non-relativistic limit one has that

$$N_X^{eq} = \frac{g}{s} \left(\frac{M_X T}{2\pi} \right)^{3/2} e^{-M_X/T}. \quad (3.11)$$

where M_X is the DM mass. Since most of the interesting dynamics will take place when the temperature is of order the particle mass, $T \sim M_X$, it is convenient to define a new measure of time

$$x = \frac{M_X}{T}, \quad (3.12)$$

because it will compare the temperature to the DM mass, and the freeze-out state starts for $x \sim 1$. To write the Boltzmann equation in terms of x rather than t , we note that

$$\frac{dx}{dt} = -\frac{1}{T} \frac{dT}{dt} x = -\frac{1}{T} \frac{dT}{da} \frac{da}{dt} x \simeq Hx, \quad (3.13)$$

where we have used that $T \sim a^{-1}$, then

$$\frac{dN_X}{dx} = -\frac{\lambda}{x^2} \left[N_X^2 - (N_X^{eq})^2 \right], \quad (3.14)$$

where we have defined

$$\lambda = \frac{2\pi^2}{45} g_{*s} \frac{M_X^3 \langle\sigma v\rangle}{H(M_X)}. \quad (3.15)$$

Eq. (3.14) is known as the *Riccati equation*. g_{*s} counts the number of relativistic degrees of freedom, and it is derived from the thermodynamics describing the state of the universe⁴. Also we assumed that in this epoch the universe is dominated by radiation, where $H = H(M_X)/x^{25}$ and $t = 1/2H$.

Fig. 3.2 shows the result of a numerical solution of eq. (3.14) for two different values of λ . At very high temperatures, $x < 1$, we have $N_X \approx N_X^{eq} \simeq 1$. However, at low temperatures, $x \gg 1$ the equilibrium abundance becomes exponentially suppressed, $N_X^{eq} \sim e^{-x}$. Ultimately, X -particles will become so rare that they will not be able to find each other fast enough to maintain the equilibrium abundance. We find that freeze-out happens at about $x_f \sim 10$. This is when the solution of the Boltzmann equation starts to deviate significantly from the equilibrium abundance. The final relic abundance, $N_X^\infty = N_X(x = \infty)$, determines the freeze-out density of dark matter. Well after freeze-out, N_X will be much larger than N_X^{eq} according to Fig. (3.2). Thus at late times (when $x > x_f$), we can drop N_X^{eq} from Boltzmann equation, which turns into

$$\frac{dN_X}{dx} \simeq -\frac{\lambda N_X^2}{x^2}. \quad (3.16)$$

Integrating from $x = x_f$ to $x = \infty$ we find

$$\frac{1}{N_X^\infty} - \frac{1}{N_X^{x_f}} = \frac{\lambda}{x_f}. \quad (3.17)$$

⁴The entropy density can be written $s = \frac{2\pi^2}{45} g_{*s}(T)T^3$.

⁵In a radiation-dominated universe we have that $H = 1.66g_*^{1/2}T^2/M_P$, where $M_P = 1.22 \times 10^{19}$ GeV. It follows that $H(m) = 1.66g_*^{1/2}m^2/M_P = Hx^2$.

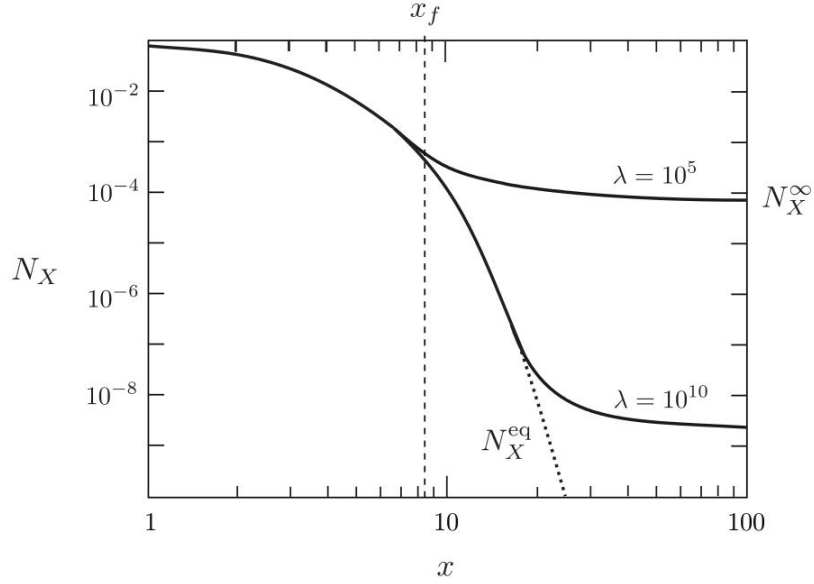


FIGURE 3.2: Abundance of dark matter particles as the temperature drops below the DM mass.

Because $N_X^\infty \ll N_X^{x_f}$, we have

$$N_X^\infty \simeq \frac{x_f}{\lambda}. \quad (3.18)$$

Of course, this still depends on the unknown freeze-out time (or temperature) x_f . Eq. (3.18) predicts that the freeze-out abundance N_X^∞ decreases as the interaction rate λ increases. This result is consistent with the fact that λ is proportional to the average annihilation cross section $\langle\sigma v\rangle$, which measure the probability of interaction between DM and the lighter particles. If the averaged cross section is low then is less probable the annihilation of DM, generating an enhancement in the abundance.

WIMP miracle

Now, if we consider that the number of WIMPs is conserved after the freeze-out we can relate the freeze-out abundance of DM to the dark matter density today. If the critical density is given by $\rho_{c,0}$, the actual dark matter parameter density is

$$\Omega_X \equiv \frac{\rho_{X,0}}{\rho_{c,0}} \quad (3.19)$$

$$\equiv \frac{M_X n_{X,0}}{3M_{pl}^2 H_0^2} = \frac{M_X N_{X,0} s_0}{3M_{pl}^2 H_0^2} = \frac{M_X N_X^\infty s_0}{3M_{pl}^2 H_0^2} \quad (3.20)$$

Substituting $N_X^\infty = x_f/\lambda$ and $s_0 \equiv s(T_0)$. This expression can be recast using the measured values at the present time

$$\Omega_X h^2 \sim 0.1 \left(\frac{x_f}{10}\right) \left(\frac{10}{g_*(M_X)}\right)^{1/2} \frac{10^{-8} \text{GeV}^{-2}}{\langle\sigma v\rangle} \quad (3.21)$$

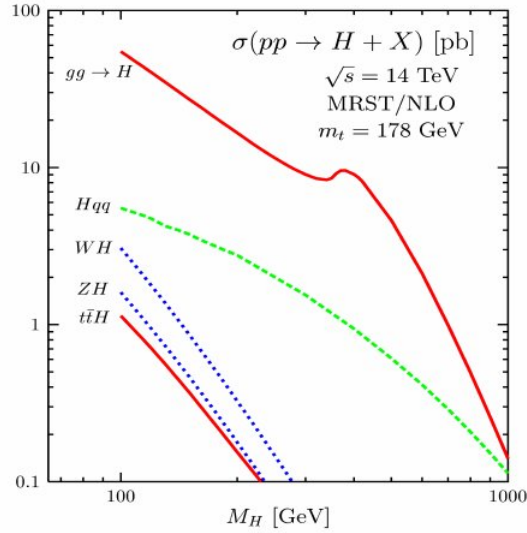


FIGURE 3.3: Dominant Standard Model Higgs production cross-sections at the LHC. Cross-sections were computed to QCD next-to-leading-order.

This reproduces the observed DM density if

$$\sqrt{\langle\sigma v\rangle} \sim 10^{-4}\text{GeV}^{-1} \sim 0.1\sqrt{G_F} \quad (3.22)$$

Equivalently, from natural units we have that $1 \text{ eV}^{-1} = 1.97 \times 10^{-7}\text{m}$, then it follows that $\langle\sigma v\rangle \sim 10^{-8} \text{ GeV}^{-2} = 10^{-36} \text{ cm}^2 = 1\text{pb}$.

The fact that a thermal relic with a cross section characteristic of the weak interaction (see Fig. 3.3 with a Higgs mass of 125 GeV) gives the right dark matter abundance is an astonishing success for particle physics. This is known as the WIMP miracle.

3.2.3 Including coannihilations

If one or more particles have a mass similar mass to the relic particle and share a quantum number with it, the standard calculation of relic density fails. In this case, it is necessary to take into account more processes into the Boltzmann equation. Let us consider N particles X_i ($i = 1, \dots, N$) with masses m_i and internal degrees of freedom (statistical weights) g_i . Also assume that $m_1 \leq m_2 \leq \dots \leq m_{N-1} \leq m_N$, and that the lightest particle is protected against decay thanks to some symmetry (i.e. R-parity or KK-parity, for neutralinos or Kaluza-Klein particles, respectively.). We will also denote the lightest particle by X_1 . In this new scenario the Boltzmann equation becomes

$$\frac{dn}{dt} + 3Hn = - \sum_{i,j=1}^N \langle\sigma_{ij}v_{ij}\rangle (n_i n_j - n_i^{eq} n_j^{eq}), \quad (3.23)$$

where n is the number density of the relic particle given by $n = \sum_{i=1}^N n_i$, due to the fact that the decay rate of particles, X_i , other than the lightest is much faster than the age of the Universe. As before, the number density in thermal equilibrium is given by

$$n_i^{eq} = \frac{g_i}{(2\pi)^3} \int d^3\mathbf{p}_i f_i, \quad (3.24)$$

where $f_i = e^{-E_i/T}$ is the Maxwell-Boltzmann distribution. Additionally,

$$\sigma_{ij} = \sum_X \sigma(X_i X_j \rightarrow X_{SM}), \quad (3.25)$$

is the total annihilation rate for $X_i X_j$ annihilations into a Standard Model particle. The relative velocity is given by

$$v_{ij} = \frac{\sqrt{(p_i \cdot p_j)^2 - m_i^2 m_j^2}}{E_i E_j} \quad (3.26)$$

where p_i and E_i being the four-momentum and energy of particle i . The thermal average is defined with equilibrium Maxwell-Boltzmann distributions given by

$$\langle \sigma_{ij} v_{ij} \rangle = \frac{\int d^3 \mathbf{p}_i d^3 \mathbf{p}_j f_i f_j \sigma_{ij} v_{ij}}{\int d^3 \mathbf{p}_i d^3 \mathbf{p}_j f_i f_j}. \quad (3.27)$$

These kind of models which consider a hierarchy of new particles in which the lightest is the DM particle can be implemented in the software MicrOMEGAS which takes into account the Boltzmann eq. (3.23) and gives the relic density for each point of the model parameter space.

3.3 Dark Matter detection

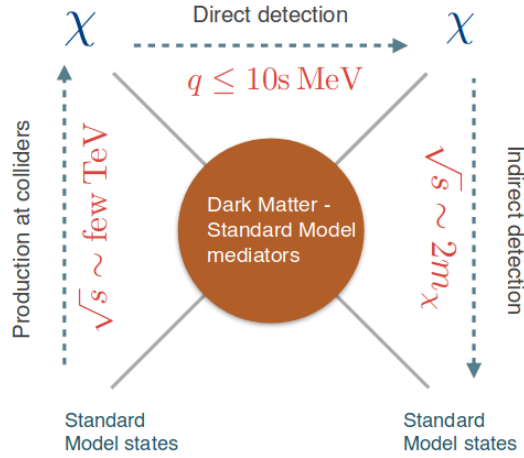


FIGURE 3.4: The three types of dark matter detection. From left to right is direct detection, from up to down indirect detection and from bottom to top is the expected collider production. In the center the mediators can be either SM or new particles.

Particle dark matter signatures are expected to be seen in three different ways: direct and indirect detection, and in collider experiments. In Fig. 3.4 is shown these types of DM searches in a pictorial way. Note that the energies involved vary from one search to another.

3.3.1 Direct Detection

Direct detection (DD) experiments aim to observe low-energy recoils (typically a few keVs) of nuclei induced by interactions with particles of dark matter, which (in theory) are passing through

the earth. After such a recoil, the nucleus will emit energy as, e.g., scintillation light or phonons, which is then detected by sensitive apparatus. It is expected that the elastic scattering of WIMPs with masses of (10 - 1000) GeV would produce nuclear recoils in the range of (1 - 100) keV.

To unambiguously identify such low-energy interactions, a detailed knowledge on the signal signatures, the particle physics aspects and nuclear physics modelling is mandatory. The calculation of event rates in direct detection experiments, the DM density, the halo velocity distribution in the Milky Way and the WIMP-nucleon scattering cross section are required. The rate is approximately given by

$$R \sim \sum_i N_i n_\chi \langle \sigma_{i\chi} \rangle, \quad (3.28)$$

where the index i runs over nuclei species present in the detector and the amount of them in it is given by

$$N_i = \frac{\text{Detector mass}}{\text{Atomic mass of species } i}. \quad (3.29)$$

The second important quantity is the local WIMP density given by

$$n_\chi \equiv \frac{\text{WIMP energy density}}{\text{WIMP mass}}, \quad (3.30)$$

and, finally, $\langle \sigma_{i\chi} \rangle$ corresponds to the cross section for the scattering of WIMPs off nuclei of species i averaged over the relative WIMP velocity with respect to the detector. The scattering DM-nucleus can be classified by two important characteristics: elastic or inelastic scattering and spin-dependent or spin-independent scattering:

- **Elastic and inelastic scattering:** The elastic scattering of a WIMP off of a nucleus in a detector is simply the interaction of the WIMP with a nucleus as a whole, causing it to recoil, ideally often enough to measure the recoil energy spectrum in the target. As we will detail below, the spectrum of recoils is exponential with typical energies of 50 keV. Current experiments can detect recoils of considerably lower energy, as low as 1-10 keV. Inelastic scattering, on the other hand, is not observed by the recoil of a target nuclei. Instead, the WIMP interacts with orbital electrons in the target either exciting them, or ionizing the target. Alternatively, the WIMP could interact with the target nuclei leaving it in an excited nuclear state. This process leaves the signature of a recoil followed by the emission of a photon a nanosecond, or so, later. Such signatures have to compete with backgrounds of natural radioactivity, however.
- **Spin-Dependent and Spin-Independent Scattering:** WIMP scattering off of nuclei is commonly discussed in the context of two classes of couplings. First, axial-vector (spin dependent) interactions result from couplings to the spin content of a nucleon. The cross sections for spin-dependent scattering are proportional to $J(J+1)$ rather than the number of nucleons, so little is gained by using heavier target nuclei. For scalar (spin-independent) scattering, however, the cross section increases dramatically with the mass of the target nuclei, and typically dominates over spin-dependent scattering in current experiments which use heavy atoms as targets.

Prediction of event rates

From classical kinematics, the energy transferred to the recoiling nucleus is

$$E_R = \frac{p^2}{2m_N} = \frac{\mu_N^2 v^2}{m_N} (1 - \cos \theta), \quad (3.31)$$

where p is the momentum transfer, θ is the scattering angle in the WIMP-nucleus center-of-mass frame, m_N is the nuclear mass and μ_N correspond to the WIMP-nucleus reduced mass. The velocity distribution of DM in the galaxy can be approximately to the Maxwell-Boltzmann one, whose velocity dispersion is 270 km s^{-1} (to compare, the escape velocity from the galaxy is 544 km s^{-1}). If we assume that $m_{DM} = m_N = 100 \text{ GeV}$, and the mean velocity is $\langle v \rangle = 220 \text{ km s}^{-1} = 0.75 \times 10^{-3} c$, the mean recoiling energy is

$$\langle E_R \rangle = \frac{1}{2} m_{DM} \langle v \rangle^2 \sim 30 \text{ keV} \quad (3.32)$$

Assuming a local DM density of $\rho_0 = 0.3 \text{ GeV cm}^{-3}$, the number density of WIMPS is $n_0 = \rho_0 / m_{DM} = 3 \times 10^{-3} \text{ cm}^{-3}$, and their flux on Earth is

$$\phi_0 = n_0 \times \langle v \rangle = \frac{\rho_0}{m_{DM}} \times \langle v \rangle = 6.6 \times 10^4 \text{ cm}^{-2} \text{ s}^{-1}. \quad (3.33)$$

Assuming an electroweak scattering cross section, from (3.28) the rate of events will be

$$R \sim N \times \phi_0 \times \sigma \sim 0.13 \text{ events kg}^{-1} \text{ year}^{-1}. \quad (3.34)$$

Input from particle and nuclear physics

In a more technical way, the differential recoil spectrum resulting from DM interactions can be written as

$$\frac{dR}{dE}(E, t) = \frac{\rho_0}{m_{DM} m_N} \int_{v_{min}}^{v_{max}} \vec{v} \cdot f(\vec{v}, t) \frac{d\sigma}{dE}(E, v) d^3v, \quad (3.35)$$

where m_{DM} is the DM mass and m_N is the nucleus mass. The DM velocity v is defined in the rest frame of the detector. Also, the equation accounts for the local DM density ρ_0 and the WIMP velocity distribution $f(\vec{v}, t)$ in the detector reference frame. The WIMP-nucleus differential cross-section $\frac{d\sigma}{dE}(E, v)$ can be expressed as the sum of a spin-independent (SI) and spin-dependent (SD) terms (if DM is a scalar the SD term will be zero):

$$\frac{d\sigma}{dE_R} = \frac{m_N}{2\mu_N^2 v^2} \left[\sigma_{SI} F_{SI}^2(E_R) + \sigma_{SD} F_{SD}^2(E_R) \right], \quad (3.36)$$

where F_{SI} and F_{SD} are the nuclear form factors, and σ_{SI} and σ_{SD} are the cross sections in the zero momentum transfer limits given by

$$\sigma_{SI} = \frac{4\mu_N^2}{\pi} [Z f_p + (A - Z) f_n]^2, \quad (3.37)$$

$$\sigma_{SD} = \frac{16\mu_N^2}{\pi} \frac{J + 1}{J} [a_p \langle S_p \rangle + a_n \langle S_n \rangle]^2. \quad (3.38)$$

f_p, f_n and a_p, a_n are the effective WIMP-couplings to neutrons and protons in the spin-independent and spin-dependent case, respectively. These parameters depend on the details of DM nature and interactions with SM particles, and they are not known *a priori*. They are usually expressed as a function of the WIMP-proton cross section σ_p . $\langle S_{p,n} \rangle = \langle N | S_{p,n} | N \rangle$ are the expectation values of the total proton and neutron spin operators in the limit of zero momentum transfer, and they have to be determined by using detailed nuclear model calculations.

Input from astrophysics

In eq. (3.35) we have seen that the rate of WIMP-nucleus collision requires data from DM velocity distribution $f(\vec{v})$ and the local dark matter density profile ρ_0 . In the so-called standard halo model (SHM), which describes an isotropic, isothermal sphere of collisionless particles with density profile $\rho(r) \propto r^{-2}$, the local density is assumed to $\rho_0 = 0.3 \text{ GeVcm}^{-3}$, and the velocity distribution is Maxwellian

$$f(\vec{v}) = \frac{1}{\sqrt{2\pi}\sigma_v} \exp\left(-\frac{v^2}{2\sigma_v^2}\right), \quad (3.39)$$

where the velocity dispersion is related to the local circular speed v_c as $\sigma_v = \sqrt{3/2}v_c$. Since the velocity distribution extends to infinity in the SHM, it has to be truncated at the measured local escape velocity v_{esc} , such that $f(\vec{v}) = 0$ for $v > v_{esc} = 544 \text{ km s}^{-1}$.

Experiments and limits

In this last 30 years there have been operating many direct detection experiments whose goal are to find direct evidence of DM. These experiments mostly use either cryogenic or noble liquid detector technologies. Cryogenic detectors operating at temperatures below 100 mK, detect the heat produced when a particle hits an atom in a crystal absorber such as germanium. Noble liquid detectors detect scintillation and ionization produced by a particle collision in liquid xenon or argon. Cryogenic detector experiments include: CDMS, CRESST, EDELWEISS, EURECA. Noble liquid experiments include ZEPLIN, XENON, DEAP, ArDM, WARP, DarkSide, PandaX, and LUX, the Large Underground Xenon experiment. Both of these techniques focus strongly on their ability to distinguish background particles (which predominantly scatter off electrons) from dark matter particles (that scatter off nuclei).

In Fig. 3.5 (left) we show cross section upper limits (until the year 2012) and projections as a function of the DM mass from a plethora of experiments mentioned above. The dominant neutrino component background for different WIMP mass correspond to the yellow region in below, and they contribution depend on the zone of the WIMP mass. At lower masses, neutrinos coming from correspond to both atmospheric and to diffuse supernova neutrino background (DSNB). In Fig. 3.5 (right) we show the recent published results from XENON1T experiment, along with the most competitive, LUX (red line) and PandaX-II (blue line). We can appreciate that some experiments have improved their sensitivities appreciable. In this thesis we use the most stringent limits until today: XENON1T.

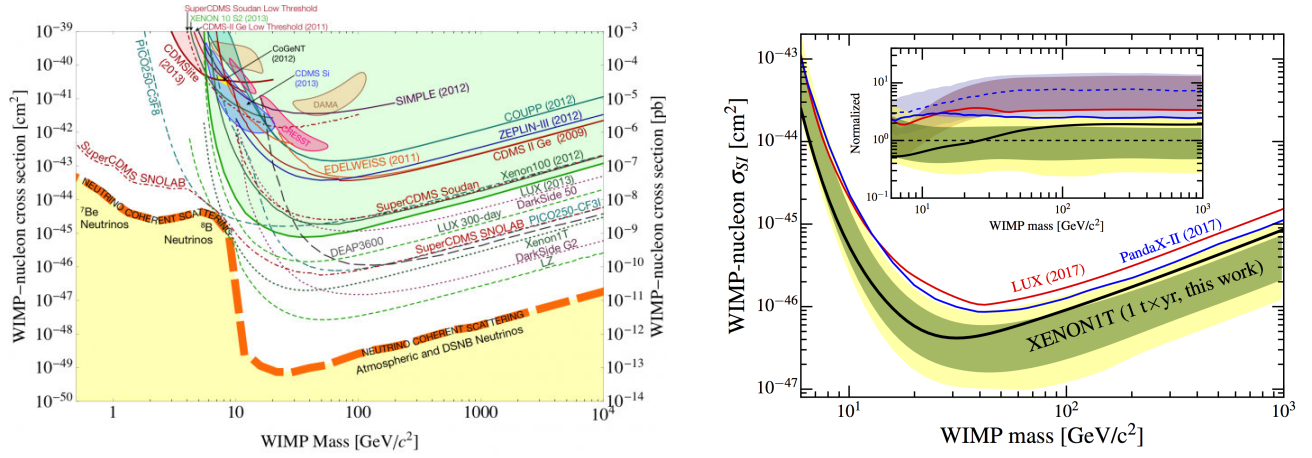


FIGURE 3.5: (left) WIMP discovery limit (thick dashed orange) compared with past limits (solid curves) and projections (dashed lines). The dominant neutrino components for different WIMP mass regions are labeled. The filled regions identify possible signal regions associated with data from CDMS-II Si (light blue, 90% C.L.), CoGeNT (yellow, 90% C.L.), DAMA/LIBRA (tan, 99.7% C.L.), and CRESST (pink, 95.45% C.L.) experiments. (right) 90% C.L. upper limit on the spin-independent WIMP-nucleon cross section from the XENON1T most recent published results [7]. The limit (black line) is shown as a function of the WIMP mass together with XENON1T 1- and 2σ sensitivity bands (green and yellow bands, respectively), and most recent results from LUX (red line) and PandaX-II (blue line).

3.3.2 Indirect detection

Indirect detection experiments search for products of the self-annihilation or decay of dark matter particles in outer space. These products may be a pair of either high-energy neutrinos, photons, charged leptons or proton/antiprotons. In this case, such particles would then propagate in the galaxy and reach us. Promising sources are usually the most dense regions, such as the galactic center, the inner halo of our galaxy, the centro of the Sun. However, sometimes the denser regions are not the better places to look for signals, because of the high astrophysical background. Therefore, it may happen that the best detection opportunities do not come from this regions, but from places with the best signal to background ratio.

There are three kind of experiments trying to identify some signal over the background: space satellites (e.g. Fermi-LAT, PAMELA), ground based (e.g. HESS, MAGIC, MILAGRO, VERITAS), and underground based detectors (e.g. IceCube, Super-K, Antares). The energy range sensitivity depends on the detector. For instance, FERMI satellite has an excellent sensitivity to gamma rays spanning a range of energies from 30 MeV to 300 GeV, or the HESS telescope has a good sensitivity mainly between 10 GeV and 10 TeV. Until now none signal has been detected, therefore upper bounds on DM annihilation cross section has been put.

The flux of dark matter annihilation products is proportional to the number of annihilations per unit time, per unit volume, $\sigma v n^2(r) \equiv \sigma v \rho^2(r)/m_{DM}^2$, where σv is the annihilation cross section multiplied by the velocity, $n(r)$ and $\rho(r)$ are the number and the mass density of a DM particle, respectively, and r is the distance from the galactic center. The flux is also proportional to the spectrum of secondary particles of species, i , per annihilation, $\frac{dN_i}{dE}$. The flux observed is found by integrating the density squared along the line-of-sight connecting the observer (the

Earth) to the Galactic center. Including all factors, the observed flux can be written as

$$\Phi_i(\psi, E) = \Delta\Omega \frac{dN_i}{dE} \frac{\langle\sigma v\rangle}{4\pi m_{DM}^2} \bar{J}_{\Delta\Omega}, \quad (3.40)$$

where $\Delta\Omega = 4\pi A$ (the area of the detector) and $\bar{J}_{\Delta\Omega}$ is called "J-factor" of the source, and is given by

$$\bar{J}_{\Delta\Omega} \equiv \frac{1}{8\pi} \int dr d\Omega \rho(\vec{r})^2 \quad (3.41)$$

The J-factors of different sources characterize the relative size of their expected annihilation signals. For example, the dwarf satellite galaxies of the Milky Way have J-factors in the neighborhood $J \sim 10^{17-20} \text{ GeV}^2/\text{cm}^5$. Other example is the region within 1 degree of the Milky Way's center which has $J \sim 10^{22} \text{ GeV}^2/\text{cm}^5$.

In what follows we show some examples of data constraints from indirect detection in neutrinos (ICECUBE) and from high energy gamma rays (EGRET and GLAST). In Fig. 3.6 (a) is shown the upper limits on the average annihilation cross section from the Galactic halo given by IceCube collaboration. In the picture is also shown the preferred regions for PAMELA data, and the region including Fermi data for annihilation to $\tau^+\tau^-$. Additionally, neutralinos can annihilate into monoenergetic gamma-ray lines via the processes $\chi\chi \rightarrow \gamma\gamma$. Fig. 3.6 (b) shows the expected gamma-ray flux as a function of the DM mass from the Galactic center from neutralino annihilations. The upper limits correspond to the solid (EGRET) and dashed (GLAST) lines.

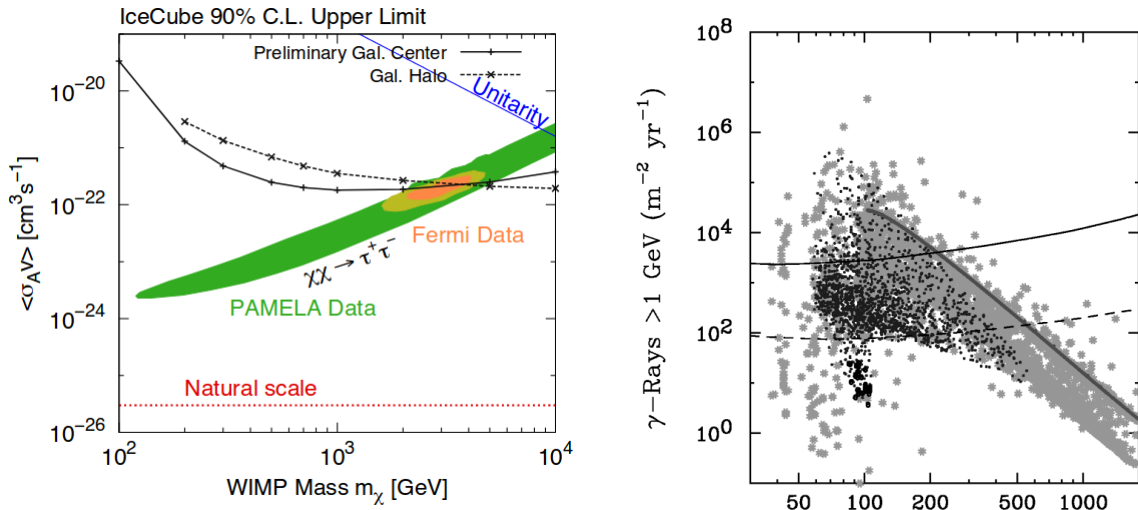


FIGURE 3.6: (left) Constraints on the DM annihilation cross section from ICECUBE's observation of the Galactic Halo, comparing with the fit regions of charged CRs. (right) Gamma-rays flux above 1 GeV per square meter per year from the Galactic center from neutralino annihilations. A NFW halo profile has been used. For each point, the thermal relic density is below the maximum value allowed by WMAP. The solid and dashed lines are the limit from the EGRET experiment and predicted sensitivity for GLAST, respectively. The various shadings refer to different scenarios of supersymmetry breaking.

3.3.3 Collider searches

Collider experiments have shown to be very useful to constraint DM particle models. However, these constraints are highly model dependent, therefore is impossible to completely describe the

reach of colliders in the search for particle dark matter. There has been different observables to search for something invisible at colliders. Single events with an imbalance in the outgoing states is what usually referred as missing energy. It refers to energy that is not detected in a particle detector, but it is expected due to the laws of conservation of energy and momentum. Neutrinos are the typical particles that are not detected in collider experiments, and in that way it is possible to trace an imbalance in the energy/momentum of the total outgoing particles. In fact, as we review below, the W^\pm boson was discovered showing some imbalance in the momentum of the outgoing particles.

In order to make a strategy to study dark matter signals at collider, it is necessary to have some background in the kinematics that has been used to search for new physics. In the following we review the kinematic that was necessary to discover the W^\pm bosons, and finally we sketch some important points in the search for dark matter at LEP and LHC.

W -boson at SPS

The discovery of the charged-current interactions (1983) at Super Proton Synchrotron (SPS) at CERN involved to deal with missing energy in the analyzed events. This is because once the W^\pm bosons were produced, they may decay to a charged lepton and its corresponding neutrino, i.e. $W^\pm \rightarrow l^\pm + \nu_l$ (of course, there are also hadron channels). How can the W^\pm mass be reconstructed?. Let us see some of kinematic of this kind of processes.

First, the transverse momentum is the momentum in the orthogonal direction to the beam, $p_T \equiv \vec{p}_T = \vec{p} \sin \theta$, where θ is the angle measured from the beam line. With this, one defines the transverse energy $E_T = \sqrt{|\vec{p}_T|^2 + m^2}$, which in the limit of vanishing mass one has $E_T = p_T$. The missing transverse momentum in an event with visible momenta is given by

$$p_T^{miss} \equiv \vec{p}_T^* = - \sum_i \vec{p}_T, \quad (3.42)$$

where i index runs for all the visible particles. Equivalently, the missing transverse energy (MET) is the magnitude of it, i.e. $E_T^{miss} \equiv \cancel{E}_T = |\vec{p}_T^*|$. Now, let us move to the W -boson decay kinematics.

In the W^\pm rest frame we have $|\vec{p}_l| = |\vec{p}_\nu| = \frac{M_W}{2}$, and $|\vec{p}_l^T| \leq \frac{M_W}{2}$. In the laboratory frame we know that the W system can be boosted only along the z axis, and the p_e^T distribution is conserved. The mass determination of the W bosons was done by two methods:

- *Lepton E_T spectrum* (Fig. 3.7(a)). It peaks at $M_W/2$. One must to compare the experimental data to Monte Carlo (MC) prediction. Note that there are some events with $E_T > M_W/2 \sim 40$ GeV, and this is because some W^\pm bosons can be produced with a little transverse momentum.
- *Transverse mass* (Fig. 3.7(b)). The invariant transverse mass is defined as

$$M_T^2 = (E_T^e + E_T^\nu)^2 - (p_T^e + p_T^\nu)^2 \quad (3.43)$$

$$= 2E_T^e E_T^\nu (1 - \cos \theta) \leq M_{inv}^2, \quad (3.44)$$

where we have neglected the electron and neutrino masses. In the last line we have emphasized that the transverse mass is always less or equal to the invariant mass of the system

lepton plus neutrino (the W mass). The maximum transverse mass is when the electron and neutrino going out back-to-back, and that occurs if $p_T(W) = 0$, then $M_T = 2E_T^e = M_{inv}$. Only these events show the maximum transverse mass, allowing to determine the W mass.

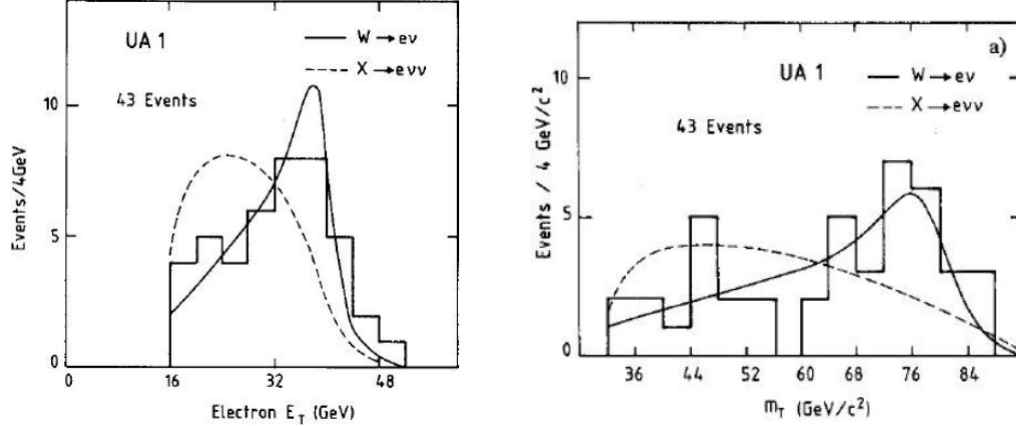


FIGURE 3.7: Two methods used to discover the W^\pm mass at UA1 experiment at SPS. The left figure shows the lepton missing energy transverse spectrum, and the right one the transverse mass of the events.

DM signatures at LEP and LHC

Dark matter searches at LEP has been searched for a long time. For example, if the DM candidate is sufficiently light, Z or Higgs bosons may decay invisibly to such particles with a non-zero branching fraction. At LEP, there has been searched for single photon events (mono-photons) over the background $e^+e^- \rightarrow Z \rightarrow \nu\bar{\nu}$, where ν are the SM neutrinos, with an additional photon radiated off of the initial state. For instance, in SUSY frameworks there is allowed the decay $Z \rightarrow \tilde{\chi}_1^0 + \tilde{\chi}_2^0$, where $\tilde{\chi}_1^0$ and $\tilde{\chi}_2^0$ are the lightest neutralinos. Until now, none event over the background has been seen, then stringent bounds on the Z boson decay has been set. In this thesis we use these limits to constraint our vectorial DM model.

Also, at the LHC there have been different searches for DM signals. For instance, DM double production accompanied by an Initial State Radiation (ISR) of some SM particle, such as a gluon or a photon, is expected to be seen. The ingoing particles (partons) have practically zero transverse energy (momentum), therefore, in the production of DM, by conservation, we expect some imbalance in the p_T final state. Due to the search simplicity and high cross section, the most used topology of DM search is mono-jet + \cancel{E}_T ⁶. This correspond to the following partonic process

$$q\bar{q} \rightarrow \chi\bar{\chi} + g, \quad qg \rightarrow \chi\bar{\chi} + q, \quad g\bar{g} \rightarrow \chi\bar{\chi} + g. \quad (3.45)$$

Other signals are mono-photon, mono- W/Z , mono-Higgs (for a review of LHC DM detection see [9]). Usually, to optimize the signal-to-background ratio, searches commonly use kinematical event selection criteria in different observables, such as a minimum value in the transverse momentum of the visible particle. Interestingly, there are some models, such as the i2HDM and the one that we study in this thesis, which give these kind of signals without the necessity of an ISR.

⁶The name mono-jet is misleading, because the probability to produce just one highly energetic jet is in fact rather low [8].

Finally, if the DM mass is below $M_H/2$, the Higgs may decay to a pair of DM particles. Combinations of the various direct searches for invisible Higgs decays have been performed by both ATLAS [10] and CMS [11]. The resulting upper bounds at 95% C.L. on the invisible branching ratio are $Br_{inv} < 0.25$ and $Br_{inv} < 0.24$, respectively.

In view of the many ways to study dark matter at the LHC, it seems legitimate to ask which one of them is the most promising and how are the details of expected distributions. There is no single correct answer to those questions. There are different theoretical approaches to study particle dark matter, and each approach has its (dis)advantage over others. In the next chapter we will review the different theoretical approaches and we will establish the model that this thesis is on.

Dark Matter Models

From the theoretical particle physics point of view, dark matter can be studied basically in three frameworks: *Effective field theory*, *Simplified models* and *Complete models*. In this chapter we will review the main aspects of each line, and some comments about the limitation of some approach over the others. As this thesis relies on a vector DM simplified model, we will sketch some frameworks in this direction: vector Higgs portal and EW vector multiplets. After that, we develop the theoretical framework of the $SU(2)_L$ vector doublet model, which is the focus of this thesis.

4.1 Theoretical DM Frameworks

As it is sketch in Fig. 4.1, from less to more complete dark matter theoretical frameworks, they can be resumed as the following

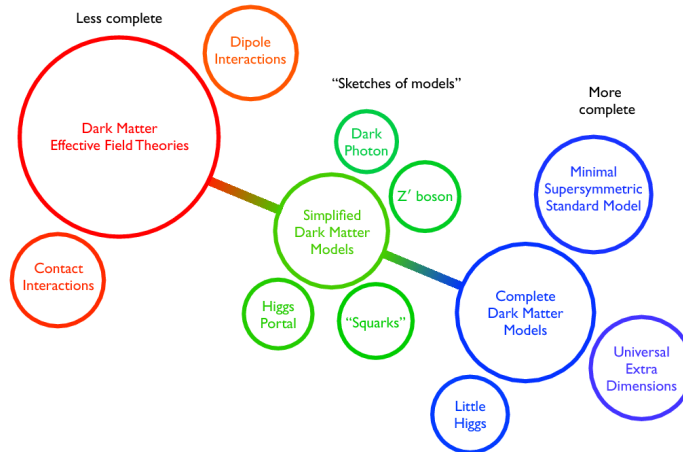


FIGURE 4.1: Particle DM theory space.

- *Effective Field Theory (EFT) approach* (see e.g. [12–19]). This description is based on writing down all the possible non-renormalizable operators between two DM fields and the Standard Model particles up to dimension six and classifying them according to the DM particle type. These operators arise after integrating out heavy mediators and are therefore

suppressed by an UV-scale Λ . For instance, for a scalar DM field χ one has

$$\mathcal{L} = \sum_i \mathcal{O}_i^{2+n}(SM) \frac{|\chi|^2}{\Lambda^n} \quad (4.1)$$

where $\mathcal{O}_i^{2+n}(SM)$ are operators of mass dimension $2 + n$ in the SM fields. Each operator is characterized by the only two parameters: the effective suppression scale Λ and the DM mass m_{DM} . One interesting point is that the lowest dimension operators can only involve the Higgs field, justifying for example the study of scenario like the *Higgs portal* one. The EFT approach is completely UV model-independent.

- *Simplified models* (see e.g. [20–24]). In this description the mediators are included in the model, and the operators in the Lagrangian usually are renormalizables. There are a lot of models in this line: Higgs portals, dark photons, extended-Higgs sectors, etc.. Both scalar and fermion dark matter has been the most explored in this line by their simplicity (for a classification see [25]). However, it has been shown that vector bosons may perfectly play the role of dark matter, most of them motivated from hidden gauge sectors [26–35]. This approach is not completely UV model-independent and generally is an *effective description*.
- *Complete Models*. Most of these frameworks are well-motivated by the Naturalness problem in the SM. However, under some conditions, usually these frameworks contain a dark matter candidate. The main theoretical alternatives considering those characteristics are supersymmetry (SUSY) [36], extra large dimensions [37], little Higgs model [38] and from a linear sigma model [39]. For example, in some SUSY theories the DM candidate (LSP) appears as a consequence of the existence of a R -parity, and typically this particle is the neutralino.

What advantages and limitations has one approach over others?, it depends on the studied context. EFT description is only justified whenever there is a clear separation between the energy scale of the process to describe and the scale of the underlying microscopic interactions (cut-off energy). In other words, EFT is valid as long as the energy scale of the process involving the DM and the SM particles is small compared to the energy scale associated to the heavy mediator. Usually, EFT works very well in the contexts of DD and ID because of the typical small momentum transfer (see Chapter 3.3). However, experiments which involve processes at higher energies, such as the LHC experiments, the EFT approach should be handled with care because the characteristic energy processes scales can be as high as the cut-off validity of the model [15, 16].

On the other hand, simplified approach becomes useful when the mediator is relatively heavy as the DM particle. The mediators can be eventually be produced on-shell and contribute significantly to processes other than the original ones considered within the EFT context [15, 16]. In other words, considering mediators makes it possible to consider different kinematic distributions and optimize the experimental sensitivity for each case. It should be noted that there is no simple way to translate an exclusion limit obtained within the EFT approach to models with a light mediator [21]. Other good reason to consider the simplified models comes from a theoretical point of view. It is quite natural to assume that the DM particle is comparable in mass to the particle responsible for its interactions. In particular it turns out to be very difficult to obtain the required DM relic abundance if the mediator is too heavy, challenging one of the primary motivations for LHC DM searches. In the presence of a light mediator, on the other hand, the relic abundance can be readily reproduced [40].

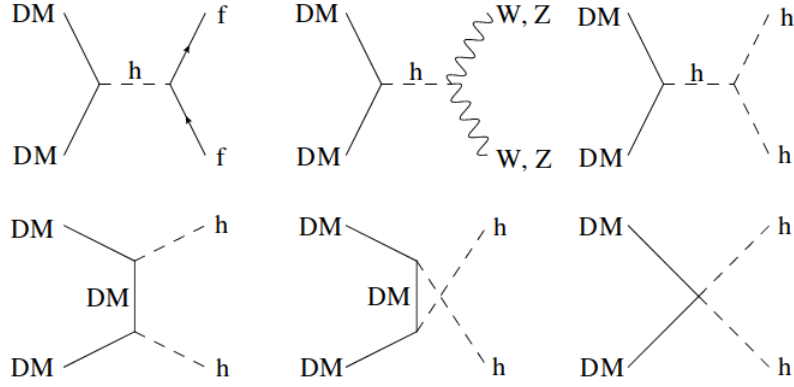


FIGURE 4.2: Feynman diagrams for dark matter annihilation in a Higgs portal.

With respect to UV-models, to test a complete theory seems not easy. For instance, SUSY contains 105 parameters, but can be reduced to the well known *phenomenological Minimal Supersymmetric Model* or pMSSM which uses *only* 19 parameters. It takes into account information from all aspects of particle physics, incorporating constraints from the measured characteristics of the Z and Higgs boson, b -quark physics, astrophysics as well as direct searches for DM at underground facilities and SUSY particles at the LHC. Still, even when working with a Complete model seems more complex than an EFT or a Simplified Model, the motivation relies in their theoretical framework. It is important to mention that it is always possible to map the constraints from a Complete Model to a Simplified model (although highly challenging), and not to an EFT, because the latter one can have multiple UV-completions.

Finally, Complete Models assures you that you have all the degrees of freedom necessary to make the complete phenomenology. Instead, Simplified Models and EFT approaches may be too simplified in their description, in the sense that they could neglect additional states (beyond the mediators), couplings, or hidden relations between the different parameters, therefore losing some information in the phenomenology. Even worse is that eventually both EFT and Simplified models have a bad UV-behavior, resulting in perturbative unitarity violation (see e.g. [41]).

Vector Dark Matter Higgs portal

New fields which are not charged under the electroweak SM gauge group and communicate with the SM Higgs boson only are said to belong to a hidden sector, and the Higgs sector acts as a portal between the SM and the new sector. The Higgs sector of the SM enjoys the feature to have the possibility to couple new degrees of freedom through the dimension-4 interaction term

$$V_{portal} = \lambda_{h\chi} |\phi|^2 |X|^2, \quad (4.2)$$

where ϕ and X represent the SM Higgs doublet and the dark matter field, respectively. For example, one portal which considers a SM singlet vector dark matter has the following Lagrangian

$$\mathcal{L} = -\frac{1}{4} F_{\mu\nu} F^{\mu\nu} + \frac{1}{2} m^2 X_\mu X^\mu + \frac{\lambda_{h\nu}}{4} \phi^\dagger \phi X_\mu X^\mu + \frac{\lambda}{4} (X_\mu X^\mu)^2, \quad (4.3)$$

where X_μ represent the vector dark matter. After electroweak symmetry breaking, the neutral

component of the doublet Higgs field is shifted to $h \rightarrow v + h/\sqrt{2}$ with $v = 256$ GeV, and the physical mass for the vector DM particle is given by

$$M_V^2 = m^2 + \frac{1}{2}\lambda_{hv}v^2. \quad (4.4)$$

The relic abundance of the DM particles is obtained through the s-channel annihilation via the exchange of the Higgs boson, through the DM in the t and u channels, and a contact diagram (see Fig. 4.2). For example, the annihilation cross section into light fermions of mass m_f is given by

$$\langle\sigma_f v\rangle = \frac{\lambda_{hv}^2 m_f^2}{48\pi} \frac{1}{(4M_V^2 - m_h^2)^2}. \quad (4.5)$$

From this expression one can note that the DM annihilation becomes much more efficient around the Higgs pole, $M_H \sim 2M_V$, which implies a fall in the relic density in that specific region. In order to study the relic density values for all the parameter space running the Boltzmann equation, we implemented the Lagrangian 4.3 into LanHEP, CalcHEP and in MicrOMEGAS software. In Fig. 4.3 (a) is shown the relic density as a function of the DM mass for a fixed coupling constant $\lambda_{hVV} = 1$. The saturation occurs at low and high masses, and it is clearly the inverted peak at the half of the Higgs mass (resonant annihilation). In Fig. 4.3 (b) is shown a 2D-projection showing the values of relic density for all the points of the model. We note that masses of a few GeV oversaturates due to the small annihilation cross section. As the DM mass increases, the abundance start to diminish, until to reach the hard interface near $M_H/2$, where an abrupt change in color is made (very small denominator in the annihilation cross section 4.5). The last important point to mention is that is clear from this figure that for small couplings the annihilation cross section also diminish, resulting in a high relic density (red color).

Furthermore, the spin-independent cross section is given by [30]

$$\sigma_{V-N}^{SI} = \frac{\lambda_{hv}^2}{16\pi M_H^4} \frac{m_N^4 f_N^2}{(M_V + m_N)^2}, \quad (4.6)$$

where m_N is the nucleon mass and f_N parametrized the Higgs-nucleon coupling. There exist different estimation of this last factor (e.g. from Lattice result $f_N = 0.326$ [42]). In view that σ_{V-N}^{SI} is bounded from above by the experiments (e.g. XENON,LUX), there is a maximum value allowed for the pair (M_V, λ_{hv}) .

Weakly interacting dark matter

Another way to provide a dark matter candidate is through the introduction of color-singlet electroweak multiplets, such as singlet, doublet, triplet, etc., under the $SU(2)_L$ gauge group and with some hypercharge (see [25, 44]). These multiplets are called generically *Minimal Dark Matter*, and they may be either scalars or fermions. In order to have a good DM candidate it is assumed that the electroweak multiplet has a certain hypercharge such that the neutral state be the lightest. Sometimes additional *discrete* symmetries are imposed in order to stabilize the lightest state such as R -parity or Z_2 . For instance, for scalar and fermion DM the following extensions to the SM are considered

$$\mathcal{L} = \mathcal{L}_{SM} + c \begin{cases} \bar{\chi} (i\not{D} + M) \chi \\ |D_\mu \chi|^2 - M^2 |\chi|^2 \end{cases} \quad (4.7)$$

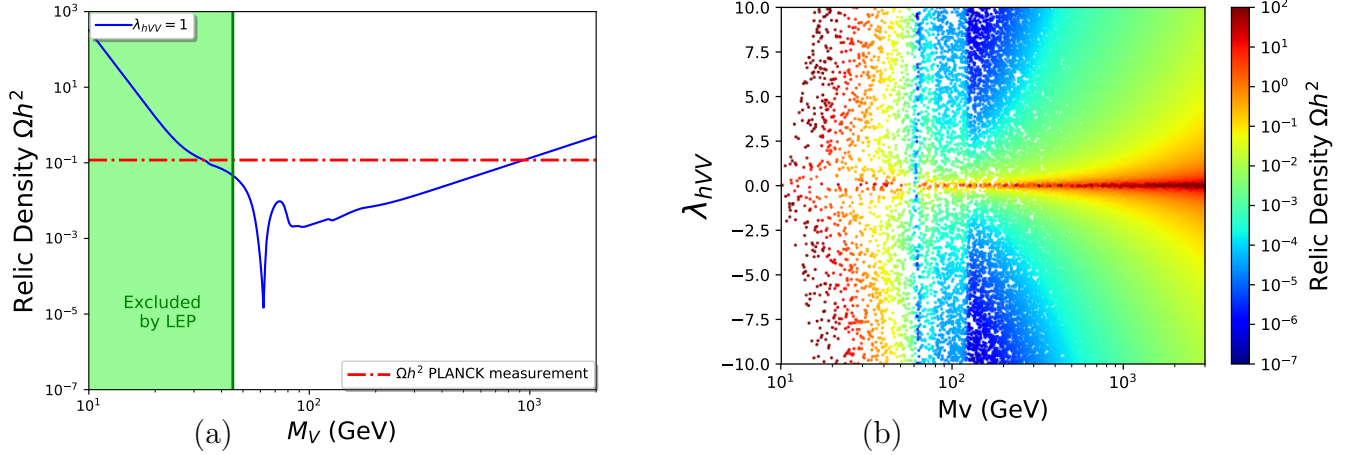


FIGURE 4.3: (left) Relic density for different dark matter masses in the singlet vector case. The red dashed line correspond to the PLANCK measurements [43]. (right) Color plot for the relic density as a function of the parameter space in $(M_V, \lambda_{h\nu})$.

where D is the gauge-covariant derivative, $c = 1/2$ for a real scalar or a Majorana fermion and $c = 1$ for a complex scalar or a Dirac fermion, and M is the tree-level mass of the particle. Quantum corrections may generate a mass splitting ΔM among the electroweak multiplet states [44].

According to vectorial DM, there have been shown different proposals of electroweak multiplet which carries a neutral state as a good dark matter candidate, such as multiplets transforming in the adjoint representation [45], and in the fundamental one in the context of 331 models [46, 47] and in Gauge-Higgs unification framework [48]. For example, the model studied in [45] contains three vectorial states: the neutral one V^0 and two charged V^\pm . A feature of this models is that the mass splitting is radiatively generated, pushing up the charged ones around ~ 200 MeV above the neutral one. If such a splitting would not exist then there would be degeneracy among the three states, making the charged ones stable and then introducing cosmological problems.

One of the problems of dealing with vector fields is that the longitudinal polarization grows indefinitely with the energy, threatening unitarity principles (for details of this point see appendix B and C). It is important to be aware of the limitations of models containing vector fields. In order to tame growing amplitudes energy behavior, UV-completion are needed motivated by gauge principles. The other way to UV-complete the model is to think the new vectors as composite states of a new underlying strong sector (e.g. Walking technicolor and Compositeness frameworks).

In this thesis we focus in an extension to the SM in which we introduce an electroweak vector doublet which enters with the same quantum numbers as the SM Higgs doublet. The model contains four new states, two neutrals and two charged, and they couples to the SM electroweak mediators i.e., Z , W^\pm and the photon, and to the Higgs boson. The model could be considered as a framework in between the Higgs portal and the weakly interacting DM models. Finally, the interaction of this new multiplet with the Higgs field makes that the degeneracy among the states be broken at tree level.

4.2 Dark Vector Dark Matter

We extend the SM by introducing a new set of vector fields transforming in the fundamental representation of $SU(2)_L$ with hypercharge $1/2$ ¹:

$$V_\mu = \begin{pmatrix} V_\mu^+ \\ V_\mu^0 \end{pmatrix} = \begin{pmatrix} V_\mu^+ \\ \frac{V_\mu^1 + iV_\mu^2}{\sqrt{2}} \end{pmatrix}, \quad (4.8)$$

The most general Lagrangian containing this new vectors with operators up to dimension four is:

$$\begin{aligned} \mathcal{L} = & -\frac{1}{2}(D_\mu V_\nu - D_\nu V_\mu)^\dagger (D^\mu V^\nu - D^\nu V^\mu) + M_V^2 V_\mu^\dagger V^\mu \\ & + \lambda_2(\phi^\dagger \phi)(V_\mu^\dagger V^\mu) + \lambda_3(\phi^\dagger V_\mu)(V^{\mu\dagger} \phi) + \lambda_4(\phi^\dagger V_\mu)(\phi^\dagger V^\mu) \\ & + \alpha_1 \phi^\dagger D_\mu V^\mu + \alpha_2 (V_\mu^\dagger V^\mu)(V_\nu^\dagger V^\nu) + \alpha_3 (V_\mu^\dagger V^\nu)(V_\nu^\dagger V^\mu) \\ & + ig\kappa_1 V_\mu^\dagger W^{\mu\nu} V_\nu + i\frac{g'}{2}\kappa_2 V_\mu^\dagger B^{\mu\nu} V_\nu + h.c. \end{aligned} \quad (4.9)$$

where $B^{\mu\nu}$ is the abelian $U(1)_Y$ field strength, and $W^{\mu\nu} = W^{\mu\nu a} \frac{\tau^a}{2}$ is the non-abelian $SU(2)_L$ field strength. In principle, all the free parameters, λ_i , α_i for $i = 1, 2, 3$ may be complex. The parameters κ_1 and κ_2 are analogous to the well-known anomalous couplings in the context of vector leptoquark models.

Due to the Lorentz representation of the new set of vector, it is not possible to couple the new vector boson to the standard fermions with renormalizable operators. For example, let us suppose a Lorentz invariant Yukawa-like coupling between SM first generation of leptons and the vector doublet. Then, consider the following vector and axial vector couplings,

$$\mathcal{L} \supset \bar{L}\gamma^\mu (g^V - g^A\gamma^5) e_R V_\mu \quad (4.10)$$

where g^V and g^A are unknown coupling constants. Considering the chirality projectors $P_{L,R}$, the Lagrangian (4.10) may be rewritten as

$$\begin{aligned} \mathcal{L} &= (\bar{\nu}_e \quad \bar{e}) P_R \gamma^\mu (g^V - g^A \gamma^5) P_R e V_\mu \\ &= (\bar{\nu}_e \quad \bar{e}) \gamma^\mu (g^V - g^A \gamma^5) P_L P_R e V_\mu \\ &= 0 \end{aligned}$$

where in the second line we have used the property $\{\gamma^\mu, \gamma^5\} = 0$, and in the last line we have used that $P_L P_R = 0$. This fact can be extrapolated straightforwardly to all SM fermions.

On the other hand, the model allows a dimension three operator which is the only one linear in V_μ . In principle, this term would introduce a mixing between the SM gauge bosons and the new vector states. However, it is possible to set up its corresponding coupling constant (α_1 in (4.9)) to zero because an accidental Z_2 symmetry appears in the Lagrangian. Due to the new symmetry this choice is technically natural in the sense of t'Hooft. Therefore, in this limit and at the renormalizable level, the new vector sector only communicates to the SM through the

¹For an explicit UV-realization of this kind of vectors see [49]. The authors show the appearance of $SU(2)_L$ massive vector doublet as the spontaneously breaking of a $U(3)_W$ gauge symmetry to the G_{SM} by some new scalar sector.

electroweak gauge bosons, the photon and SM-Higgs boson. As a consequence, the flavour sector is untouched at tree level.

Finally, the terms in the last line of (4.9) are allowed by the symmetry. However the value of their coupling constant (κ_1 and κ_2) are not fixed by the symmetries. In this paper, we work in the simplified case where $\kappa_1 = \kappa_2 = 1$. This choice is consistent with the hypercharge assigned to V_μ and agrees with what happen in vector leptoquarks models, where the ultra-violet gauge completion and unitarity arguments fixes the values of those parameters to one [50]. In other words, if we allow for values different to one, there appear the coupling among the photon A_μ and the two neutral vector V^1 and V^2 , implying the latter fields now get an electric charge.

As we explained above, in the limit when α_1 vanish, the model acquires an additional Z_2 discrete symmetry allowing the stability of the lightest odd particle (LOP). If the LOP happens to be a neutral component of V_μ (as it must be for cosmological reasons) then it constitutes a good DM candidate. In this case, the Lagrangian (4.9) reduces to:

$$\begin{aligned}
\mathcal{L} &= -\frac{1}{2} (D_\mu V_\nu - D_\nu V_\mu)^\dagger (D^\mu V^\nu - D^\nu V^\mu) + M_V^2 V_\mu^\dagger V^\mu \\
&- \alpha_2 (V_\mu^\dagger V^\mu)(V_\nu^\dagger V^\nu) - \alpha_3 (V_\mu^\dagger V^\nu)(V_\nu^\dagger V^\mu) - \lambda_2 (\phi^\dagger \phi)(V_\mu^\dagger V^\mu) \\
&- \lambda_3 (\phi^\dagger V_\mu)(V^{\mu\dagger} \phi) - \frac{\lambda_4}{2} [(\phi^\dagger V_\mu)(\phi^\dagger V^\mu) + (V^{\mu\dagger} \phi)(V_\mu^\dagger \phi)] \\
&+ i \frac{g'}{2} V_\mu^\dagger B^{\mu\nu} V_\nu + ig V_\mu^\dagger W^{\mu\nu} V_\nu.
\end{aligned} \tag{4.11}$$

The Lagrangian 4.11 contain six free parameters² which we labelled as $\lambda_2, \lambda_3, \lambda_4$ for quartic coupling involving interactions between SM-Higgs field and the new vector field, a mass term M_V , and α_2, α_3 for quartic couplings of pure interactions among the vector fields. These latter self-interacting terms are not relevant for the experimental constraints and dark matter phenomenology done in this paper, therefore from now on we will not consider them, However, self-interacting particle dark matter can be relevant in related fields such as astrophysical structures [51].

After EWSB the tree level mass spectrum of the new sector is

$$M_{V^\pm}^2 = \frac{1}{2} [2M_V^2 - v^2 \lambda_2], \tag{4.12}$$

$$M_{V^1}^2 = \frac{1}{2} [2M_V^2 - v^2 (\lambda_2 + \lambda_3 + \lambda_4)], \tag{4.13}$$

$$M_{V^2}^2 = \frac{1}{2} [2M_V^2 - v^2 (\lambda_2 + \lambda_3 - \lambda_4)], \tag{4.14}$$

For phenomenological purposes we will work in a different base of free parameters

$$M_{V^1}, \quad M_{V^2}, \quad M_{V^\pm}, \quad \lambda_L, \tag{4.15}$$

where $\lambda_L = \lambda_2 + \lambda_3 + \lambda_4$ is the coupling controlling the interaction between the SM Higgs and V^1 (see Fig. (4.4)). This parameter will be very important in the constraints and phenomenological study.

It is convenient to write the quartic coupling and the mass parameter as a function of the new

²We assume that all the free parameters are real, otherwise, the new vector sector may introduce CP-violation sources. In this work we do not deal with that interesting possibility.

free parameters

$$\begin{aligned}\lambda_2 &= \lambda_L + 2 \frac{(M_{V_1}^2 - M_{V_{\pm}}^2)}{v^2}, & \lambda_3 &= \frac{2M_{V_{\pm}}^2 - M_{V_1}^2 - M_{V_2}^2}{v^2}, \\ \lambda_4 &= \frac{M_{V_2}^2 - M_{V_1}^2}{v^2}, & M_V^2 &= M_{V_1}^2 + \frac{v^2 \lambda_L}{2}.\end{aligned}\quad (4.16)$$

For future convenience, it will be useful to introduce

$$\lambda_R \equiv \lambda_2 + \lambda_3 - \lambda_4 = \lambda_L + \frac{2(M_{V_2}^2 - M_{V_1}^2)}{v^2}, \quad (4.17)$$

which is not a new free parameter, but it is the effective coupling constant which governs the HV^2V^2 interaction.



FIGURE 4.4: Feynman diagram coupling two DM particles to the Higgs Boson.

It is important to mention that because the new vector fields have the same quantum numbers as the SM-Higgs field, the two neutral vectors have opposite CP-parities. However, we can switch their parity just by making a change of bases $V_\mu \rightarrow iV_\mu$ and then re-label each field as $V_\mu^1 \rightarrow V_\mu^2$ and $V_\mu^2 \rightarrow V_\mu^1$ and still obtain the same phenomenology. Therefore, without loss of generality, we will choose V_μ^1 as the LOP, turning it into our Dark Matter candidate. Following the same line, to make sure that V_μ^1 is the lightest state of the new sector, we can find some restrictions that the quartic couplings must follow to satisfy this condition. Considering this, we can stress that

$$\begin{aligned}M_{V_2}^2 - M_{V_1}^2 > 0 &\quad \Rightarrow \quad \lambda_4 > 0, \\ M_{V_{\pm}}^2 - M_{V_1}^2 > 0 &\quad \Rightarrow \quad \lambda_3 + \lambda_4 > 0.\end{aligned}\quad (4.18)$$

In order to have a weakly interacting model, we set that all the coupling parameters must satisfy

$$|\lambda_i| < 4\pi \quad \wedge \quad |\alpha_j| < 4\pi \quad (i = 2, 3, 4; \quad j = 2, 3). \quad (4.19)$$

Finally, we want to make a comment about the Lagrangian structure. Beyond the vectorial character of the new fields, the Lagrangian shares an equivalent spectrum and couplings to the most well-known inert Two Higgs Doublet Model (i2HDM) [52–54]. In view of the similarities, in some parts of the phenomenology we used to compare both models. For more details about the i2HDM, see appendix A.

Model implementation

We implemented this model using the LanHEP [55] package and we used CalcHEP [56] and micrOMEGAS [57–59] for collider and DM phenomenology calculations, respectively. We included

effective vertex Hgg and $H\gamma\gamma$ and we performed a cross-check of the gauge invariance implementation calculating several $2\rightarrow 2$ processes in both gauges (Unitary and 'tHooft - Feynman gauge) using `CalcHEP` [56] program. The Dark Matter phenomenology was made with the `micrOMEGAs` [57–59] package. This program solves the Boltzmann equation numerically and calculate all of the relevant annihilation cross sections involved in the process using the `CalcHEP` program. `micrOMEGAs` consider as well the followign effects:

- The case $M_{V^1} < M_W, M_Z$ takes into account the annihilation into 3-body final state from VV^* or 4-body final state from V^*V^* ($V = W^\pm, Z$).
- The co-annihilation effects are present when the mass split among the DM and the other particles is small. We took into account the $V^1 - V^2$, $V^1 - V^\pm$ and $V^2 - V^\pm$ cases.
- The spin-independent cross section of DM scattering off the proton.

Experimental constraints

There are many experimental ways to constraint a theoretical model, and in this chapter we concentrate in the following ones: LEP searches for both SM gauge boson invisible decay and SUSY particles, LHC measurements on the Higgs decay to both diphoton and invisible, Relic density bounds by WMAP and Planck satellite, and finally direct detection (DD) by the strongest bounds until now given by XENON1T experiment. We do not impose bounds from indirect detection because they are weaker than DD.

5.1 LEP limits

Considering that the coupling between the SM gauge bosons and the dark sector is fixed by gauge invariance, the only way to avoid deviations from precise LEP-I constraints on W and Z widths [60] [61] is to demand that the channels $Z \rightarrow V^1V^2, V^+V^-$ and $W^\pm \rightarrow V^1V^\pm, V^2V^\pm$ are kinematically not open. This leads to the following conditions on the masses

$$\begin{aligned} M_{V^1} + M_{V^\pm} &> M_{W^\pm}, & M_{V^2} + M_{V^\pm} &> M_{W^\pm}, \\ M_{V^1} + M_{V^2} &> M_Z, & 2M_{V^\pm} &> M_Z. \end{aligned} \tag{5.1}$$

On the other hand, bounds on supersymmetric particles searches at LEP has been very useful to constraint other models beyond SM. In particular, LEP-II limits on neutralinos and charginos has been used to constraint the inert doublet model (i2HDM) [62, 63]. Although there are some differences in the number of Feynman diagrams and the spin involved in the processes, the kinematical efficiencies among the two result to be quite similar, allowing to recast the experimental bounds.

In view of the identical topologies in the processes of the i2HDM and our model, it seems natural to extend the LEP bounds to our vectorial case. The concern is whether the efficiencies of the vectorial signals are similar to the SUSY ones. In the case of neutral state production, the process $e^+e^- \rightarrow Z \rightarrow V^1V^2$ shows a distribution more isotropic and similar to neutralinos, because both cases, having intrinsic spin, have the ability to conserve angular momentum. Scalars, on the other hand, which are produced through the same topology than the vector ones, $e^+e^- \rightarrow Z \rightarrow H^0A^0$, are produced in p -waves, making the scalars to have large transverse momentum. Additionally, as it has been shown in [62], the angular differences between SUSY signals and the scalar ones are even more reduced when are added the decay products of their respective new states. Therefore, we expect similar efficiencies among our signals and SUSY ones, allowing to recast LEP-II bounds.

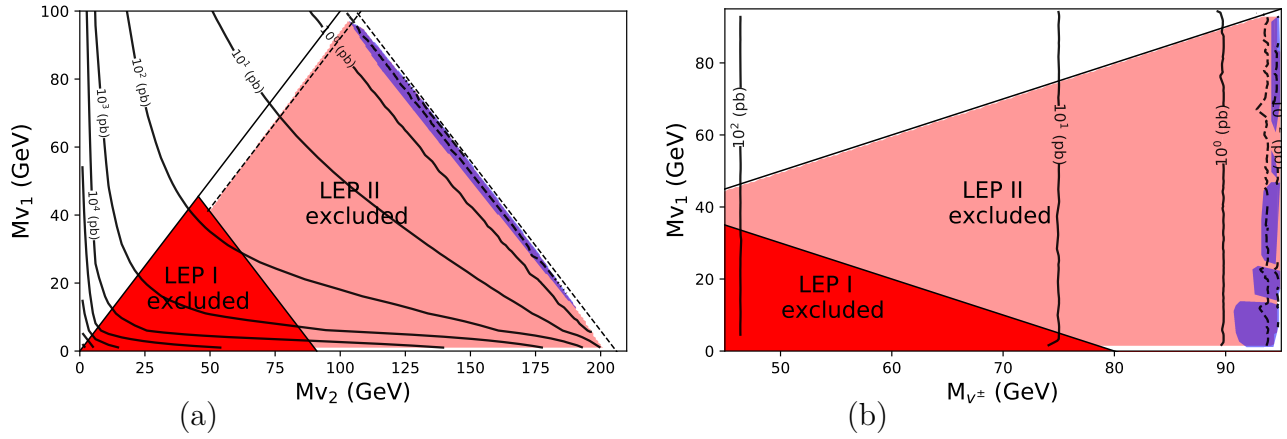


FIGURE 5.1: (a) Allowed mass region for neutral vectors based on 95% C.L. upper-limits on $e^+e^- \rightarrow \tilde{\chi}_1^0 \tilde{\chi}_2^0$ cross section at $\sqrt{s} = 189$ GeV [64]. The solid black contour lines indicate the production cross section $e^+e^- \rightarrow V^1 V^2$ at LEP. The red(blue) zones are forbidden (allowed) by LEP-II data. The red shaded region is excluded by LEP-I data on the Z boson width (see 5.1). (b) Allowed mass region for charged and neutral vector based on 95% C.L. upper-limits on $e^+e^- \rightarrow \tilde{\chi}_1^+ \tilde{\chi}_2^-$ cross section at $\sqrt{s} = 189$ GeV [65]

In Fig. 5.1(a) we show the recast limits from neutralinos searches at LEP-II to our model [64]. The allowed region is a small narrow blue area close to the LEP energy threshold. The exclusion region is notoriously higher than the scalar case [62] because the production cross section for vectors present an enhancement through their longitudinal polarization, compared to the scalar case (see 6.4). The resulting excluded region is

$$M_{V1} < 100 \text{ GeV} \ \& \ M_{V2} < 200 \text{ GeV} \ \& \ \Delta M_{12}^- > 8 \text{ GeV} \ \& \ \Delta M_{12}^+ < E^{LEP} - 8 \text{ GeV} \quad (5.2)$$

where $\Delta M_{12}^\mp \equiv M_{V2} \mp M_{V1}$ and E^{LEP} is the maximum LEP center of mass energy (189 GeV).

Additionally, charginos searches [65] also put strong constraints on the charged vector states V^\pm . As it is shown in Fig. 5.1(b), the limit on the charged vectorial mass results to be

$$M_{V^\pm} \lesssim 93 \text{ GeV}. \quad (5.3)$$

5.2 LHC data

5.2.1 $H \rightarrow \gamma\gamma$

The Higgs boson has multiples decay channels, but the cleanest one at the LHC is when it decays to two photons. Actually, the strongest signature for the Higgs discovery was from this channel. In the SM there is no interaction between the Higgs and photons at tree level, however, at one-loop level the former can decay into a pair of photons considering charged gauge bosons W^\pm and fermions as internal particles. Equivalently, the DVDM introduces two more diagrams at one loop which must to be taken into account (see Fig. 5.2) in order to quantify the modifications in observables such as the Higgs decay width into two photons. In what follows, we calculate the contributions of these new diagrams to the Higgs decay width, and then we contrast our theoretical results with the strong restrictions from measurements on this channel [66].

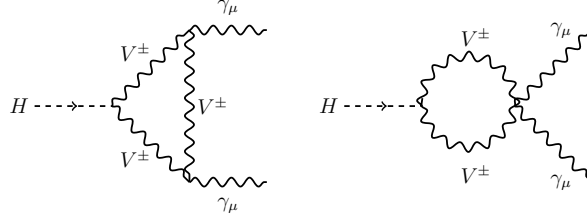


FIGURE 5.2: One-loop contributions from the charged vectors V^\pm on the Higgs decay into two photons

In order to get the Higgs decay width in DVDm, we must to start by the invariant amplitude. Note that the matrix element can be written as [67]

$$\mathcal{M} = \frac{e^2 g}{(4\pi)^2 M_W} F(k_1 \cdot k_2 g^{\mu\nu} - k_2^\mu k_1^\nu) \epsilon_\mu(k_1) \epsilon_\nu(k_2), \quad (5.4)$$

where k_1 and k_2 are the four-momentum for the respective photon final states, and $\epsilon_\mu(k)$ is the corresponding photon polarization. F is a function that depends on the masses of the particles and couplings involved in the respective loop. For example, in the SM these functions are very well known, and their values are

$$F = \sum_f N_c Q_f^2 F_{1/2}(\beta_f) + F_1(\beta_W), \quad (5.5)$$

where N_c is the color factor (1 for leptons and 3 for quarks), and $\beta_f \equiv 4M_f^2/M_H^2$ and $\beta_W \equiv 4M_W^2/M_H^2$. The functions in 5.5 are given by

$$F_{1/2}(\beta_f) = -2\beta_f [1 + (1 - \beta_f)f(\beta_f)], \quad (5.6)$$

$$F_1(\beta_W) = 2 + 3\beta_W + 3\beta_W(2 - \beta_W)f(\beta_W), \quad (5.7)$$

where

$$f(\beta) = \begin{cases} \arcsin(1/\beta)^2 & \text{for } \beta \geq 1, \\ -\frac{1}{4} \left[\ln \frac{1+\sqrt{1-\beta}}{1-\sqrt{1-\beta}} - i\pi \right]^2 & \text{for } \beta < 1. \end{cases} \quad (5.8)$$

Therefore, once determined the F factor, one is able to get the decay width through the expression

$$\Gamma(H \rightarrow \gamma\gamma) = |F|^2 \left(\frac{\alpha}{4\pi} \right)^2 \frac{G_F M_H^3}{8\sqrt{2}\pi}. \quad (5.9)$$

The goal now is to get the to determine the new F factor coming from the diagrams Fig. 5.2. The procedure was done using Wolfram Mathematica software (the loop factors were worked with OneLoop package). The result is given by

$$F_V = \frac{\lambda_2}{2} \left(\frac{v}{M_{V^\pm}} \right)^2 F_1(\beta_V), \quad (5.10)$$

where λ_2 is the coupling of the new charged bosons V^\pm to the Higgs boson, and M_{V^\pm} is the mass of it. Adding the new contribution to the SM F -factor, and using (5.9), we find that the Higgs decay width to two photons at one loop level is given by

$$\Gamma(H \rightarrow \gamma\gamma) = \frac{\alpha^2 M_H^3}{256\pi^3 v^2} \left| \sum_i N_{ci} Q_i^2 F_{1/2}(\beta_i) + F_1(\beta_W) + \frac{\lambda_2}{2} \left(\frac{v}{M_{V^\pm}} \right)^2 F_1(\beta_V) \right|^2. \quad (5.11)$$

We consider the most recent limit coming from the $\sqrt{s} = 13$ TeV ATLAS Higgs data analysis [66] to set restrictions on the parameter space. The new contributions respect to the SM are parametrized as the ratio of the branch ratios between our model and the SM

$$\frac{Br^{BSM}(H \rightarrow \gamma\gamma)}{Br^{SM}(H \rightarrow \gamma\gamma)} = \mu^{\gamma\gamma} = 0.99 \pm 0.14. \quad (5.12)$$

The new contributions to $\mu^{\gamma\gamma}$ are governed by the parameters λ_2 and $M_{V\pm}$ or, equivalently, by λ_L and the difference of masses between M_{V^1} and $M_{V\pm}$, as previously shown in eq.(4.16).

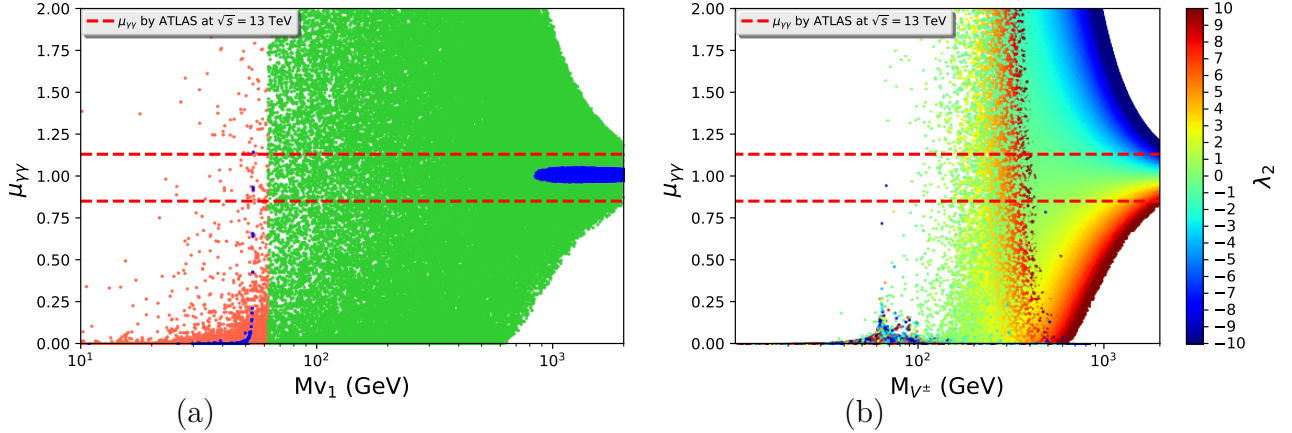


FIGURE 5.3: a) Diphoton rate $\mu^{\gamma\gamma}$ vs DM mass M_{V^1} in two regions: the pink region correspond to $M_{V^1} \leq M_H/2$, where $H \rightarrow V^1V^1$ channel is open, and the green one to $M_{V^1} > M_H/2$, where $H \rightarrow V^1V^1$ channel is closed. The blue color represents relic saturation. b) Color map for diphoton rate as a function of the parameter λ_2 and the charged vector mass $M_{V\pm}$. The horizontal dashed red lines represent the global signal strength coming from $\sqrt{s} = 13$ TeV ATLAS Higgs data analysis (5.12). These plots take into account perturbativity restrictions (4.19).

In Fig.(5.3)(a) we present the diphoton rate as a function of the DM mass M_{V^1} where the parameter space was divided in two regions: the pink points ($10 \leq M_{V^1} \leq M_H/2$) represent the zone where the decay mode $H \rightarrow V^1V^1$ is open making the decay mode $H \rightarrow \gamma\gamma$ very low and therefore pushing $\mu^{\gamma\gamma}$ under the experimental limit for most of the points, and the green points ($M_{V^1} > M_H/2$) the zone where the decay mode $H \rightarrow V^1V^1$ is closed. In both regions we show in blue the points which are consistent with the observed amount of DM. We also present a color map of the parameter λ_2 as a function of the diphoton rate vs charged vector mass $M_{V\pm}$ in Fig.(5.3)(b). In both cases the horizontal red lines represent the global signal strength coming from $\sqrt{s} = 13$ TeV ATLAS Higgs data analysis (5.12).

We can notice that diphoton rate constraints are very restrictive ruling out an important amount of the parameter space mostly when $|\lambda_2|$ takes big values in the region $M_{V\pm} \gtrsim 400$ GeV. However, for higher masses such as $M_{V\pm} \gtrsim 1$ TeV, still there is a region where $\mu^{\gamma\gamma}$ is within the experimental limit for high couplings, e.g. $|\lambda_2| > 5$. Another interesting feature of the results is related to the reaching of DM saturation. In the low mass region ($\lesssim 60$ GeV) the points that could give the correct abundance given by PLANCK is practically all ruled out, surviving a very small fraction of points. On the other hand, the high mass region which saturates the PLANCK limit matches perfectly with the $\mu^{\gamma\gamma}$ measurements where ($|\lambda_2| < 2$) and ($M_{V\pm} - M_{V^1} \lesssim 20$ GeV) values are preferred.

5.2.2 Invisible Higgs decay

The Higgs boson is one of the portals connecting the dark sector with the SM, however there is an important restriction that we need to worry about. When $M_{V^1} \leq M_H/2$, the SM-Higgs boson can decay into Dark Matter particles, which translate into invisible decays. On the other hand, both ATLAS and CMS experiments at the LHC has been searching for Higgs invisible decays at $\sqrt{s} = 7, 8$ and 13 TeV, putting the restrictive upper limit

$$Br(H \rightarrow \text{inv}) < 24\%, \quad (5.13)$$

at 95% of confidence level [?]. In this section we interpret the CMS upper bound as the maximum possible branching ratio of the Higgs boson into dark matter particles, i.e.

$$Br(H \rightarrow V^1 V^1) \equiv \frac{\Gamma(H \rightarrow V^1 V^1)}{\Gamma_{SM} + \Gamma(H \rightarrow V^1 V^1)} < Br_{inv}^{max}, \quad (5.14)$$

where $Br_{inv}^{max} = 24\%$ and Γ_{SM} corresponds to the the full decay width of the SM Higgs. In the center of mass frame, the expression for the decay width is

$$\Gamma(H \rightarrow VV) = \frac{p_f}{32\pi^2 M_H^2} \int \sum_{pol} |\mathcal{M}|^2 d\Omega, \quad (5.15)$$

where sum runs over the polarizations of the vector final states, and the tree momentum is given by

$$p_f = \frac{m_H}{2} \sqrt{1 - \frac{4M_V^2}{m_H^2}}. \quad (5.16)$$

The amplitude is given by

$$\mathcal{M} = \Gamma_{\mu\nu} \epsilon^\mu(k_1) \epsilon^\nu(k_2), \quad (5.17)$$

where $\Gamma_{\mu\nu} = -2i\lambda_L M_W s_W g_{\mu\nu}/e$. For simplicity, we define $\gamma \equiv 2\lambda_L M_W s_W/e$. The square amplitude is

$$\sum_{pol} |\mathcal{M}|^2 = \gamma^2 \sum_{pol} \epsilon_\mu(k_1)^* \epsilon^\nu(k_2)^* \epsilon_\mu(k_1) \epsilon^\nu(k_2) \quad (5.18)$$

Using the relation

$$\sum_{pol} \epsilon_\mu(k)^* \epsilon_\nu(k) = -g_{\mu\nu} + \frac{k_\mu k_\nu}{k^2}, \quad (5.19)$$

we have

$$\sum_{pol} |\mathcal{M}|^2 = \gamma^2 \left(-g_{\mu\nu} + \frac{k_{1\mu} k_{1\nu}}{k_1^2} \right) \left(-g_{\mu\nu} + \frac{k_{2\mu} k_{2\nu}}{k_2^2} \right) \quad (5.20)$$

$$= \gamma^2 \left(2 + \frac{(k_1 \cdot k_2)^2}{M_V^4} \right). \quad (5.21)$$

In the c.m. reference, we have

$$k_1 \cdot k_2 = \frac{1}{2} (M_H^2 - 2M_V^2) \quad (5.22)$$

$$= \frac{1}{2} \sqrt{M_H^4 \lambda(M_V^2, M_V^2; M_H^2) + 4M_V^4}, \quad (5.23)$$

where

$$\lambda(x, y; z) = \left(1 - \frac{x}{z} - \frac{y}{z}\right)^2 - 4\frac{xy}{z^2}. \quad (5.24)$$

In the regime when both final states are on-shell we have $k_1^2 = k_2^2 = M_V^2$. After some algebra we get

$$\frac{1}{2} \sum_{pol} |\mathcal{M}|^2 = \frac{\gamma^2}{2} \left(3 + \frac{\lambda(M_V^2, M_V^2; M_H^2)}{4} \left(\frac{M_H}{M_V}\right)^4\right) \quad (5.25)$$

where we have divided by two because of the identical particles in the final state. Finally, the decay width is given by

$$\Gamma(H \rightarrow V_1 V_1) = \frac{M_W^2 \lambda_L^2}{8\pi g^2 M_H} \left(3 - \frac{M_H^2}{M_{V_1}^2} + \frac{1}{4} \frac{M_H^4}{M_{V_1}^4}\right) \sqrt{1 - \frac{4M_{V_1}^2}{M_H^2}} \quad (5.26)$$

where g is the weak coupling constant. Replacing 5.26 into 5.14 we get the following bound on λ_L

$$|\lambda_L| < \left(\frac{8\pi \Gamma_{SM} g_w^2 M_H \left(\frac{1}{B_{inv}^{\max}} - 1\right)^{-1}}{M_W^2 \left(3 - \frac{M_H^2}{M_{V_1}^2} + \frac{1}{4} \frac{M_H^4}{M_{V_1}^4}\right) \sqrt{1 - 4M_{V_1}^2/M_H^2}} \right)^{1/2} \quad (5.27)$$

This bound is extremely restrictive because allows only very small values of λ_L ¹. For example, when M_{V_1} is close to $M_H/2$ (~ 60 GeV), relation (5.27) sets $\lambda_L \lesssim 0.03$. This constraints is complementary to the one given by Higgs diphoton decay, which strongly constrained dark matter masses below $M_H/2$, eliminating almost completely the region $M_{V_1} \leq M_H/2$.

The case described above was based on the assumption that the sole channel contributing to the Higgs invisible decay is $H \rightarrow V^1 V^1$. However, when $M_{V_2} < M_H/2$, the channel $H \rightarrow V^2 V^2$ can also contributes to the invisible Higgs decay provided that $\Delta M = M_{V_2} - M_{V_1}$ is small enough (of the order of a few GeV or less), to forbid V^2 to decay into V^1 and a detectable pair of fermions. Considering that $\lambda_R = \lambda_L + \frac{2(M_{V_2}^2 - M_{V_1}^2)}{v^2}$, and in this case, $M_{V_2} \approx M_{V_1}$, then $\lambda_L \approx \lambda_R$. Therefore, in this case the limit on λ_L can be easily modified.

Finally, in the case of a small $V^\pm - V^1$ mass split, the channel $H \rightarrow V^\pm V^\mp$ may also contributes to the Higgs invisible decay channel. However, LEP limits 5.3 put very strong constraints on the allowed masses of the charged vectors, then making the Higgs decay into the on-shell charged vectors kinematically forbidden.

5.3 Relic Density constraints

As we mentioned in section 4 our model has a 6-dimensional parameter space but only four free parameters are relevant for our study: three physical masses of the vector fields ($M_{V_1}, M_{V_2}, M_{V^\pm}$) and λ_L , the parameter which regulates the coupling between the SM-Higgs boson and a pair of V^1 . In order to show a general qualitative description of the DM relic density $\Omega_{DM} h^2$ as a function

¹This strong constraint in the coupling among the Higgs boson and the dark matter is also shown in the i2HDM [68] with similar results.

of the parameter space we fix some of them and perform a scan over the more relevant ones. The results should be in agreement with the most recent relic density value given by PLANCK [43,69], i.e.

$$\Omega_{\text{DM}}h^2 = 0.1184 \pm 0.0012. \quad (5.28)$$

To simplify the analysis we consider $M_{V^2} = M_{V^\pm}$ (equivalently to fix $\lambda_3 = \lambda_4$ (see 4.14)). In this scenario, once we fix the mass difference $\Delta M = M_{V^2} - M_{V^1}$, then the two relevant parameters are M_{V^1} and λ_L . We will present two characteristic scenarios which we will refer to as: a) *quasi-degenerate* case, where $\Delta M = M_{V^2} - M_{V^1} = 1$ GeV, and b) the *non-degenerate* one, in which $\Delta M = M_{V^2} - M_{V^1} = 100$ GeV. In Fig. 5.4 we present a 2-dimensional parameter space where we show $\Omega_{\text{DM}}h^2$ as a function of the DM mass M_{V^1} for different λ_L values in the two scenarios mentioned above. The horizontal red dashed line corresponds to the central value of the relic density measured by PLANCK.

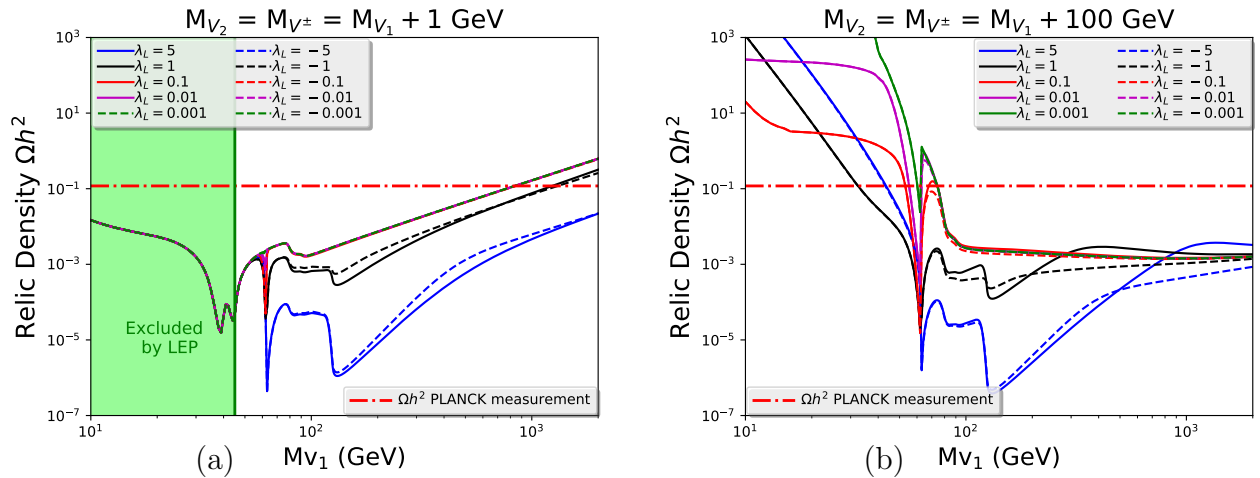


FIGURE 5.4: Relic density $\Omega_{\text{DM}}h^2$ as a function of M_{V^1} for different values of λ_L in a quasi-degenerate scenario (a) where $M_{V^2} = M_{V^\pm} = M_{V^1} + 1$ GeV and a non-degenerate scenario (b) where $M_{V^2} = M_{V^\pm} = M_{V^1} + 100$ GeV. The horizontal red line corresponds to the central value of the relic density measured by PLANCK. The green area indicates the excluded region by LEP measurements.

The first important aspect we can appreciate of these results is that there are two regions that fulfill the DM budget. The first saturation zone happens between $30 < M_{V^1} < 80$ GeV in the non-degenerate scenario as shown in Fig.(5.4)(b). In this case the main annihilation mechanism is through the s-channel Higgs boson exchange which is controlled by the λ_L coupling. Interestingly, there is a considerable area of overabundance for small values of M_{V^1} even for large values of λ_L . Of course, this region must be excluded as non physical.

As it is shown Fig.(5.4)(a), the second saturation region takes place in the quasi-degenerate scenario when $M_{V^1} > 830$ GeV. In this zone the interaction between the DM and the longitudinal polarization of W^\pm and Z boson becomes dominant. This interaction is modulated by λ_i quartic couplings which in turn depend on the mass difference among the new vectors as it is shown in eq.(4.16). When ΔM is small the λ_i become small enough to produce a suppression in the annihilation average cross section for these channels pushing the DM abundance up to reach the saturation limit, even when the (co)annihilation effects are present which become subdominant. In contrast, in the non-degenerate cases the annihilation of DM is more efficient due to the large values of λ_i which results in the asymptotically flat behavior of abundance for high DM mass values.

The overabundance seen in the non-degenerate scenario for small values of M_{V^1} completely disappears in the quasi-degenerate case due to effects of (co)annihilation which introduces new sources of annihilation of DM, pushing the abundance below the PLANCK experimental limit. When $M_{V^1} \sim 40$ and $M_{V^1} \sim 45$ GeV we can note the effects of resonant (co)annihilation through $V^1 V^\pm \rightarrow W^\pm$ and $V^1 V^2 \rightarrow Z$ channels respectively that manifests on Fig.(5.4)(a) as two inverted peaks.

At exactly $M_{V^1} \sim 62.5$ GeV the resonant annihilation through the Higgs boson take place as we can see in both scenarios as a deep peak. After that resonance we observe three points where the abundance of DM decreases considerably. This happens markedly at $M_{V^1} \sim 80$ GeV through the opening channel $V^1 V^1 \rightarrow W^+ W^-$ and more tenuously at $M_{V^1} \sim 90$ GeV through $V^1 V^1 \rightarrow ZZ$. Finally at $M_{V^1} \sim 125$ GeV the opening of $V^1 V^1 \rightarrow HH$ take place corresponding to the reduction of DM relic density through s-channel Higgs boson.

One can also observe that in the case of $\Delta M = 100$ GeV, for M_{V^1} below 65 GeV, DM co-annihilation is suppressed and the relic density is equal or below the experimental limit only for large values of λ_L ($\lambda_L > 0.1$) which are excluded by LHC limits on the invisible Higgs decay.

Finally it is easy to notice that for larger values of λ_L the abundance of DM decreases, however, is important to stress that there is a slight difference for the case in which λ_L takes positives and negatives values after $M_{V^1} \sim 62.5$ GeV. This behavior is due interference effect between the s-channel Higgs boson exchange diagram and and those involving gauge bosons.

5.4 Direct Detection limits

We consider as well whether our model is consistent with the limits coming from XENON1T [70] experiment studying the rescaled spin independent proton-DM scattering cross section

$$\hat{\sigma}_{SI} = (\Omega_{DM}/\Omega_{\text{PLANCK}}) \times \sigma_{SI}(V^1 p \rightarrow V^1 p) \quad (5.29)$$

, which allows us to take into account the case when the vector V_1 contribute only partially to the total amount of DM. This approach is useful to take into account other sources that can contribute to fulfill the DM budget. We present the $\hat{\sigma}_{SI}$ as a function of the DM mass for several values of λ_L in the quasi-degenerate and non degenerated scenario as we shown in Fig. 5.5. The green area, shown in both plots is the excluded region from the direct detection (DD) experiment and the soft red color in Fig. 5.5(a) is excluded by LEP data.

The σ_{SI} is through the t-channel with the Higgs boson as a mediator, therefore we can notice immediately that λ_L plays an important roll which is scale the strength of the interaction between DM and nucleus of ordinary matter. In the quasi-degenerated scenario the asymptotically flat behavior of the $\hat{\sigma}_{SI}$ for $M_{V^1} > 100$ GeV can be explained because as M_{V^1} take higher values, the cross section σ_{SI} is decreasing, however this effect is compensated by the fact that there is more abundance of DM as the value of M_{V^1} is increasing. This can be checked in Fig. 5.4(a). On the other hand, in the non-degenerate scenario the $\Omega_{DM} h^2$ is relatively constant after the DM annihilation channel $V^1 V^1 \rightarrow HH$ is opened (see Fig. 5.4(b)), therefore, as the value of DM mass is increasing the $\hat{\sigma}_{SI}$ is taking smaller values.

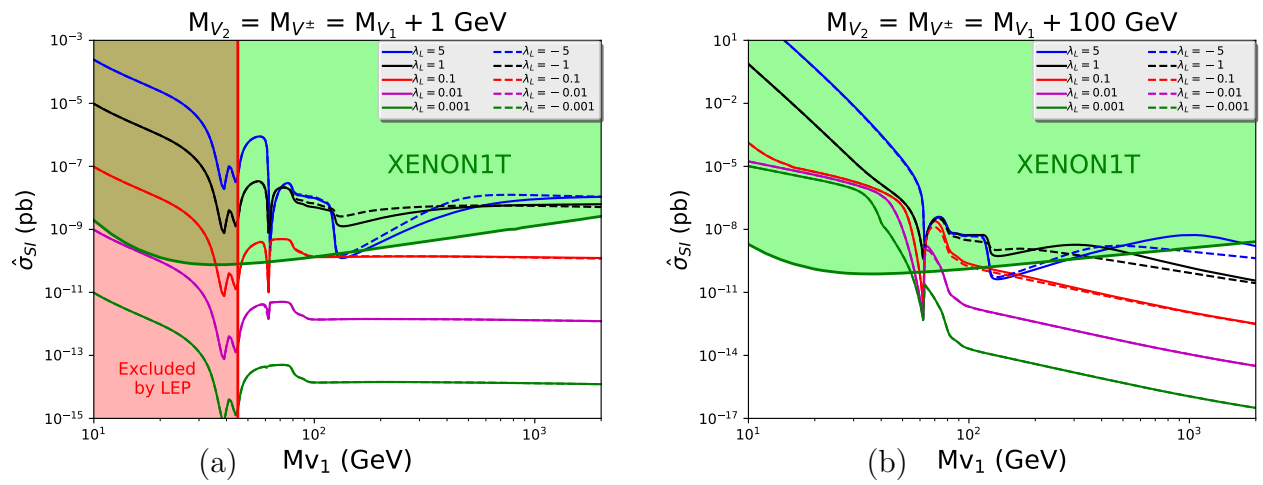


FIGURE 5.5: Rescaled spin independent direct detection cross section $\hat{\sigma}_{SI}$ versus M_{V_1} and the XENON1T constraint for several values of λ_L . The red-shaded region in the left frame is excluded by LEP data.

Dark matter phenomenology

After having explored separately LEP, LHC, PLANCK and XENONT1T constraints on the vector doublet model (DVDM), it is necessary to get together all of them into a unique analysis in order to see the viability and how well this kind of DM can account for the relic density of dark matter in the Universe. Additionally, one important thing which could play a special role in discriminating between DM models via collider observables are missing transverse energy ($\mathbf{E}_T^{\text{miss}}$) and some kinematical properties of the SM particles produced in association with DM particles. For example, at the LHC mono-jet signatures are events with high transverse momentum p_T and a large $\mathbf{E}_T^{\text{miss}}$. These kind of signatures are considered to be a "discovered channel" for DM.

In this chapter we focus our attention in a full parameter space of the model applying all the constraints studied in the previous chapter. Additionally, we highlight the parameter points at which the DVDM gives the correct relic density (saturation), and we compare the DM cross section and the missing energy distribution shapes for mono-jet, $-Z$ and $-Higgs$ signals of the vector DM in the model presented in this work and the resulting from the well-studied model inert Two Higgs Doublet Model (i2HDM) [52, 54, 71–74], which has a very similar coupling and states structure, but the new states are spinless

6.1 Parameter Space Scan

The previous description provides us with a qualitative overview of the parameter space. However, in order to have a deeper understanding of the model we perform a random scan using 7 million points of the most relevant parameters that have direct interference in the phenomenology of dark matter. The range of the parameters used in the scan are summarized in Table (6.1).

TABLE 6.1: Range of the 4-dimensional parameter space.

Parameter	min value	max value
M_{V1} [GeV]	10	2000
M_{V2} [GeV]	10	2000
$M_{V\pm}$ [GeV]	10	2000
λ_L	-12	12

The scan results are presented in Fig. (6.1), where we show several plots with 2-D projections of the 4-dimensional parameter space as a color map of DM relic density. We considered the parameter space without any theoretical or experimental constraint in the first row, and then, in

the second one we took into account perturbativity (4.19), LEP limits (5.1, 5.2 and 5.3), Higgs decay into two photons (5.12), Invisible Higgs decay (5.13), overabundance DM Relic density (5.28) and Xenon1T Direct Detection constraints.

As we explained previously, and without losing generality, we work in the region where $M_{V1} < M_{V2}$ and therefore $\lambda_4 > 0$. For this reason we exclude the region $M_{V1} > M_{V2}$ as we can see from the gray region in Fig. 6.1(b). The different pattern of colors represent the amount of DM that the model is capable of explain considering a thermal production mechanism, where the dark red color in the low DM mass region ($M_{V1} \lesssim 45$ GeV) of Fig. 6.1(a,b) represent overabundance which we consider as non physical. The dark blue colors are the regions with extreme under-abundance of DM which is more accentuated for large values of λ_L in the zone where $M_{V1} > M_H/2$ after the respective annihilation channels (WW , ZZ and HH) are progressively opened, reflecting the same pattern shown previously in Fig.5.4.

In Fig. 6.1(a,b) the resonant annihilation through the Higgs boson is easily recognized by the vertical separation around $M_{V1} \sim 62.5$ GeV, where a steep break in the color pattern can be seen, changing from an light green to a dark blue. We can also notice the resonant (co)annihilation through the Z boson in the plane (M_{V1}, M_{V2}) of Fig.(6.1)(b) at the region $M_{V1} = M_{V2} \sim 45$ GeV.

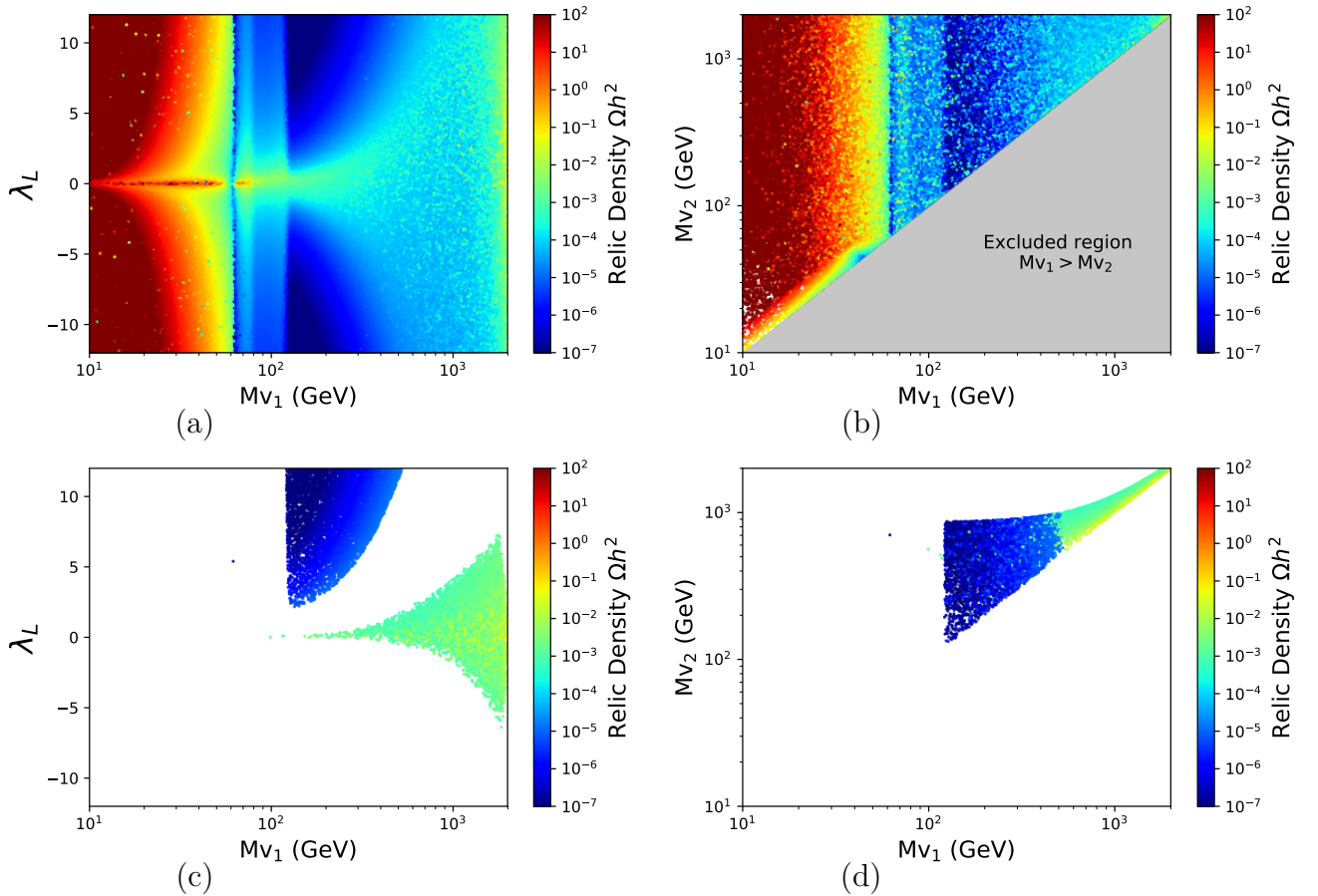


FIGURE 6.1: 2-D projections of the 4-dimensional parameter space presented as a color map of $\Omega_{\text{DM}}h^2$ in two different planes: (M_{V1}, λ_L) plane for Fig.(a,c) and (M_{V1}, M_{V2}) plane for Fig.(b,d). In the first row we present the parameter space without any constraint and in the second one we applied all the theoretical and experimental constraints with exception of DM under-abundance.

Taking into account perturbative restrictions, the region of the parameter space that shows an important mass difference between M_{V1} and M_{V2} is excluded since this large difference increases the values of the quartic coupling beyond the allowed value set by (4.19). This effect can be seen clearly in Fig. (6.1)(d) where the region with $M_{V2} > 900$ GeV for $M_{V1} < 500$ GeV is excluded. Only when the mass difference becomes relatively small, M_{V2} can admit larger values.

By incorporating the restrictions coming from Higgs invisible decay almost all the parameter space for $M_{V1} \lesssim M_H/2$ disappears with exception of a very narrow region where λ_L parameter take small values ($\lambda_L \lesssim 0.02$). This happen because the dominant annihilation channel is through the higgs boson exchange.

The Higgs diphoton rate (5.12) introduce strong restrictions on the parameter space specially for negative values of λ_L . We can see that restriction in the Fig.(6.1)(c) where λ_L is limited from below through the parabolic shape as we increase the values of M_{V1} . The diphoton rate depend explicitly on $\lambda_2 = \lambda_L + 2(M_{V1}^2 - M_{V\pm}^2)/v^2$, where the difference of squared masses is always negative because $M_{V1} < M_{V\pm}$, therefore when the mass difference is large and λ_L takes high negative values, the parameter λ_2 grows in demacy, causing a great deviation from the experimental value of $\mu^{\gamma\gamma}$. This can also be seen as well in Fig. (5.3)(b).

The additional constraint from XENON1T DD experiments removes part of the parameter space contained between $63 < M_{V1} < 125$ GeV where the direct detection rate is more sensitive. This affects the region for positive and negative values of λ_L , however the negative part was removed previously by the Higgs diphoton rate constraint as we can see from Fig.(6.1)(c). The scattering cross section between V^1 and nuclei is through the t-channel with the Higgs boson as a mediator, therefore it depends explicitly on the parameter λ_L . For large values of λ_L the abundance of DM is low, but not low enough to suppress the DM detection rate through DD signal. Only when λ_L is small ($\lesssim 0.02$), the region between $90 < M_{V1} < 200$ GeV of the parameter space is able to bypass the limits of direct detection. When we move to a high DM mass region ($M_{V1} \gtrsim 200$ GeV), where the DD rate is less sensitive, we still have a excluded region with parabolic shape that it is only reached for large values of λ_L . It produces a clear division between a low density of DM zone with the rest of the parameter space. However, in the case of high degeneracy among the vector masses for the region $M_{V1} > 900$ GeV the DD rate is able to restrict parameter space for values of λ_L up to 1, as we will see later in the next subsection.

6.2 Vector Dark Matter as the only source

In the previous paragraphs we considered experimental and theoretical constraints in our parameter space but we maintained the assumption that our DM candidate contributes partially to the DM budget, therefore we relaxed the lower limit of the measurements made by the PLANCK satellite. Here, we show how the model can completely explain the abundance of DM for some special region of the parameter space taking into account both upper and lower PLANCK limits at 1σ (5.28). For that reason, in Fig. 6.2 we present a 2D projection of the 4-dimensional parameter space for the planes (M_{V1}, λ_L) and (M_{V1}, M_{V2}) , where we show all the points which can saturate the PLANCK limit but only the red points survived all the restrictions mentioned above.

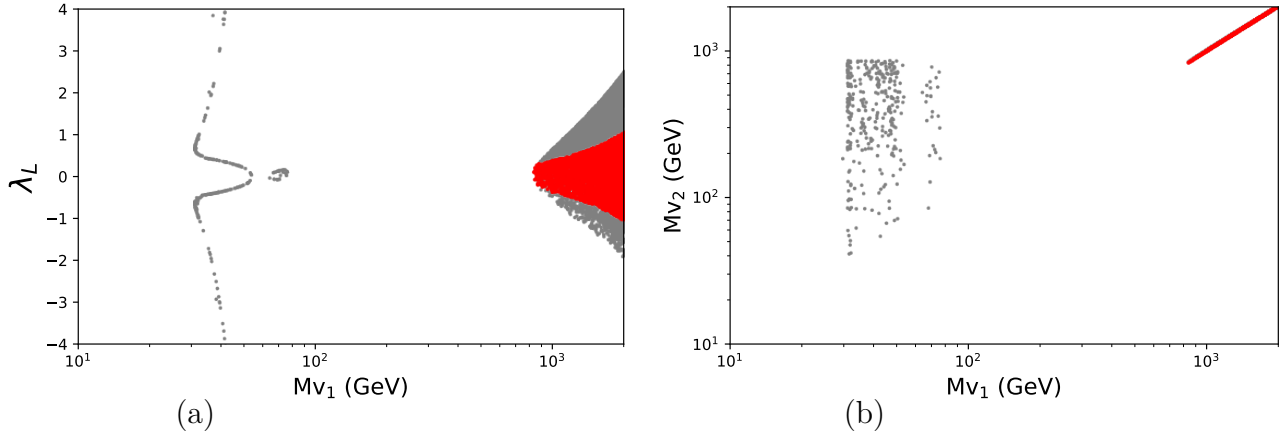


FIGURE 6.2: 2-D projections of the 4-dimensional parameter space in two different planes: (M_{V1}, λ_L) plane in (a) and (M_{V1}, M_{V2}) in (b). We show all the points where the model fulfill the PLANCK limit, but the gray points are constrained by experiments and the red ones survive all the restrictions.

As we discussed earlier, there are two regions where the vector DM reach the experimental limit. The first one happen in the low DM mass region between $35 < M_{V1} < 80$ GeV. However this zone is complete exclude by the experimental constrains. The region of interest which survive after all the restrictions is located the high DM mass zone where $M_{V1} \gtrsim 840$ GeV as we can see from Fig. 6.2. This result contrasts with the one found in references [46, 47] where the dark vector can only explain partially the DM relic abundance. One of the most important features of this regions is the high level of degeneracy between the vector masses showed in the plane (M_{V1}, M_{V2}) of Fig.(6.2)(b) where the mass splitting do not exceeds $\Delta M < 20$ GeV.

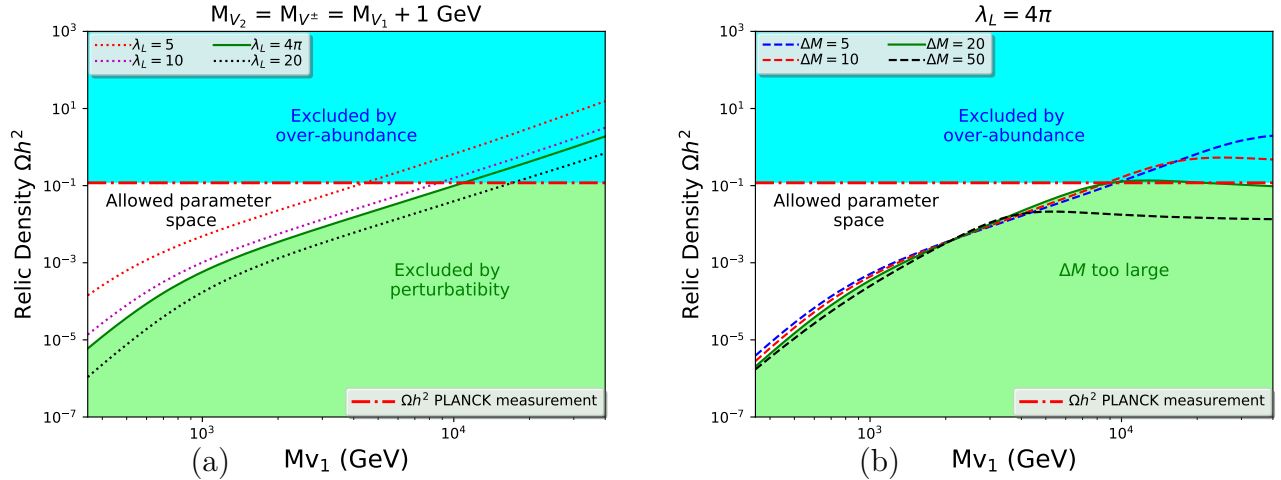


FIGURE 6.3: Closing the parameter space at high values of M_{V1} and λ_L in a quasi-degenerate scenario.

Despite the fact that direct detection experiment are less sensitivity in the zone of high DM mass, the XENON1T constraints are still able to exclude parameter space for $\lambda_L > 0.3$ in this zone. As the value of M_{V1} increases and DD loses sensibility, the allowed region becomes bigger. This effect is appreciated as the gray region in Fig.6.2(a) for $M_{V1} > 840$ GeV.

As we increase the value of M_{V1} in this scenario of high degeneracy, we can notice that λ_L can take larger values. However, when $M_{V1} \sim 10$ TeV we reach the maximum value for λ_L allowed by the perturbability constraints (4.19). Now, with this value of λ_L , the difference of masses between

DM and the other vectors can only reach up to 20 GeV, after that point the quartic couplings become too large making the effective DM annihilation cross section fall below the experimental value of PLANCK. This completely closes the parameter space of the model as we can see from Fig. 6.3.

6.3 Dark matter production at the LHC

The DM double production associated with either mono-jet, $-Z$ or $-Higgs$ are signals expected to be seen at the LHC in the context of dark matter searches. Due to the similarities in the topology of these processes between our model and the well know inert-two-Higgs-doublet-model (i2HDM)¹ we compare the parton level distribution cross section and the missing transverse energy shape those signals². The calculations were done with CalcHEP package, using NNPDF23_lo_as_0130_qed (proton) as parton distribution functions, and a generic transverse momentum cut of 100 GeV on each of the SM particles.

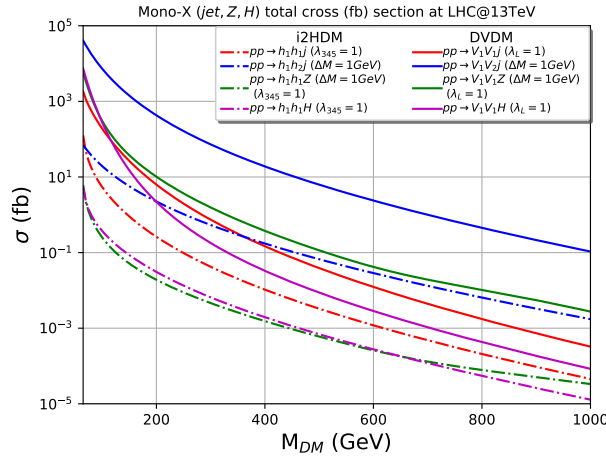


FIGURE 6.4: Mono- X (j, Z, H) cross section as a function of the DM mass. The dashed lines correspond to the scalar case (i2HDM) and the continuous one to the vectorial one (DVDM).

In Fig. 6.4 we show the total cross section for different mono-signals as a function of the DM mass in both models for LHC@13TeV. The continuous lines correspond to the case of vector DM (DVDM), whereas the dashes lines to the scalar case (i2HDM). All the process consider the quasi degenerate mass scenario $\Delta M = 1$ and $\lambda_{345}(\lambda_L) = 1$.

Because the topology of the Feynman diagrams in both models are exactly the same in all the processes studied here, the differences lies mainly in the spin of the final states. The dependence of the cross section on the DM mass is similar in both cases. However the vector case is scaled up over the scalar one by two orders of magnitude approximately. This vector cross section enhancement is due to the fact that the longitudinal polarization of vectors scale as $\sim E/M_V$, implying that the production matrix element receive a significant enhancement in the region of phase space where the DM state is relativistic and either one or both particles are longitudinally

¹The i2HDM has an equivalent spectra but with scalar states: h_1, h_2 and h^\pm . Typically, the lightest odd particle (i.e., the dark matter candidate) is chose to be h_1 , and λ_{345} corresponds to the tree-level coupling between the scalar DM and the Higgs boson.

²Detailed analysis of DM production at LHC considering these processes in the i2HDM see [54], and a more fine analysis for mono-jet signature at the LHC see [68].

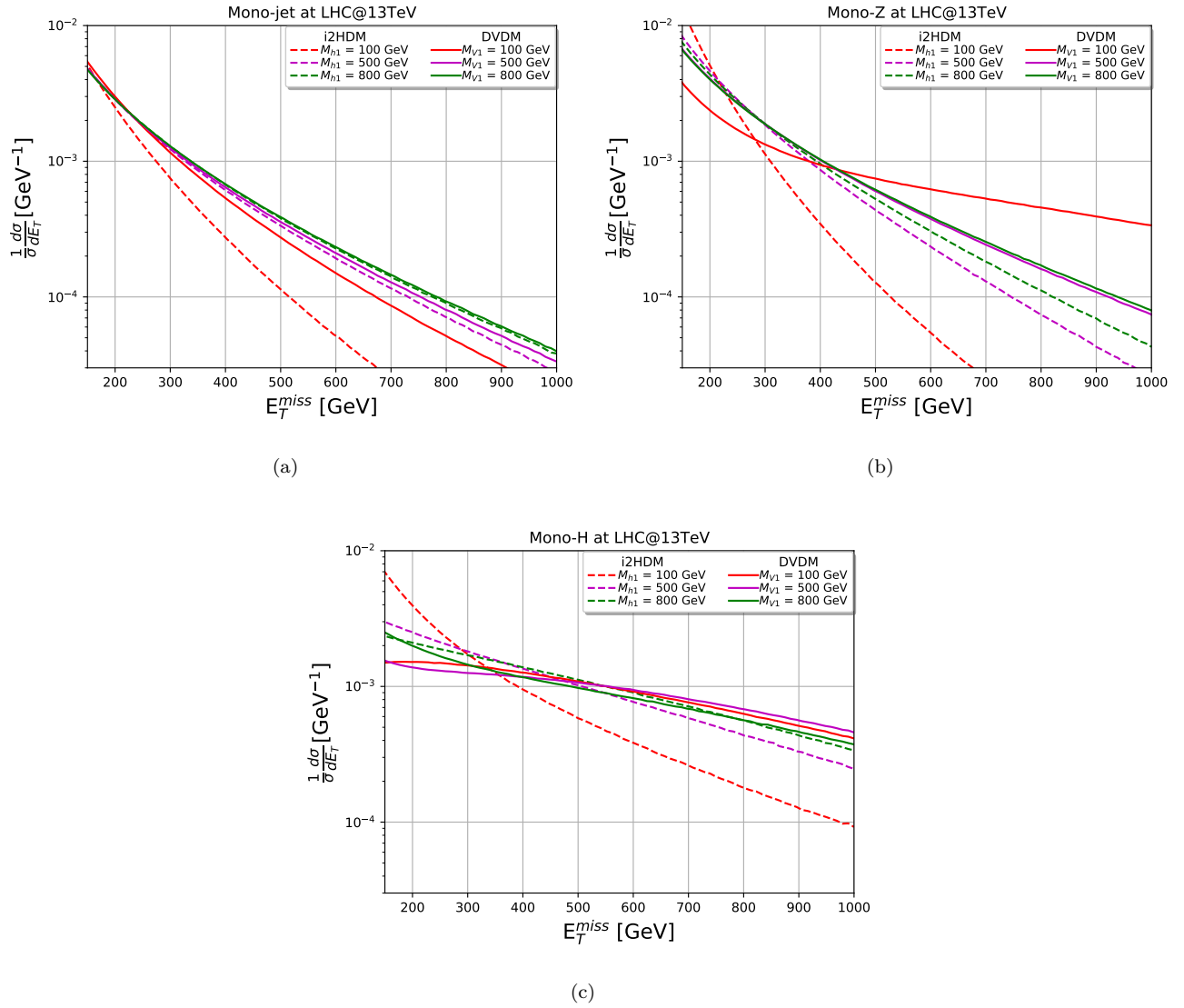


FIGURE 6.5: Normalized differential missing transverse energy cross section for the processes $pp \rightarrow X + \cancel{E}$ ($X = j, Z, H$) in *i2HDM* and *DVDM*. The dashed lines correspond to the predictions of the *i2HDM* and the continuous one in the *DVDM*. All the plots contain different DM mass: 100, 500 and 800 GeV, in the quasi-degenerate case, i.e. $\Delta M = 1$ GeV, $\lambda_{345}(\lambda_L) = 0.1$, and at $\sqrt{s} = 13$ TeV LHC energies. A $p_{T,X} \geq 100$ GeV cut has been applied in all the plots.

polarized.

On the other hand, in Fig. 6.5 are shown the normalized missing transverse energy distribution cross section of each one of the processes at parton level, considering $\Delta M = 1$ GeV and $\lambda_L = 0.1$. In each channel, the distributions for the vector case are always flattened respect to the scalar ones. This behaviour is in agreement with the results presented in [17]. Furthermore, the differences in the shapes are more notorious in the cases in which the new state masses are lower. Considering that mono-jet signals have the higher cross sections, we complement the analysis with the invariant mass distribution of the DM pairs. In Fig. 6.6 we present $M_{\text{inv}}(DM, DM)$ distributions for the scalar and vector cases in the mono-jet case, again normalized to unity for $\sqrt{s} = 13$ TeV LHC energies. From Fig. 6.6, one can see that the $M_{\text{inv}}(DM, DM)$ distributions are better separated for higher masses of scalars and vectors. The scalar distributions are closer

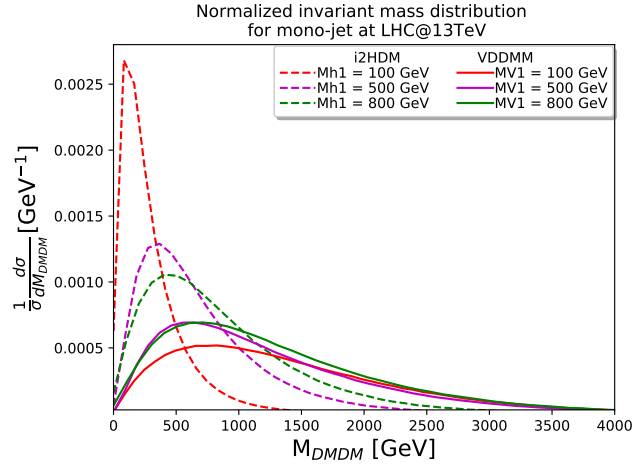


FIGURE 6.6: Invariant mass of DM pair distributions normalized to unity for mono-jet in both *i2HDM* (dashed) and *DVDM* (continuous) at 13 TeV LHC energy. All the results are considering $\lambda_{345}(\lambda_L) = 0.1$, in the quasi-degenerate case, i.e. $\Delta M = 1$ GeV.

to the point $M_{\text{inv}}(DM, DM) = 2M_{\text{DM}}$, whereas the vectorial ones distributions are broader.

TABLE 6.2: Total cross section (fb) for $pp \rightarrow X + \cancel{E}$, ($X = j, Z, H$) with $\lambda_{345}(\lambda_L) = 0.1$, *NNPDF23_1o_as_0130 qed* (proton) as a PDF, and $p_T^X > 100$ GeV. Here, the missing energy is due to the production of V_1V_1 , V_1V_2 and V_2V_2 . The same for the scalar case.

Model	i2HDM			DVDM		
	100	500	800	100	500	800
Mono- j	1.9×10^1	6.6×10^{-2}	6.4×10^{-3}	7.3×10^3	6.2	4.5×10^{-1}
Mono- Z	3.7×10^{-1}	2.9×10^{-3}	3.1×10^{-4}	7.3×10^2	4.1×10^{-1}	2.8×10^{-2}
Mono- H	1.0×10^{-2}	2.0×10^{-5}	2.2×10^{-6}	3.0×10^2	3.1×10^{-3}	9.7×10^{-6}

Conclusions

Unlike most of extensions to the Standard Model which consider new massive vector fields as singlets or triplets under $SU(2)_L$ gauge group, in this work we have explored a different possibility. The new vector degrees of freedom enter into the SM in the fundamental representation of $SU(2)_L$, with hypercharge $Y = 1/2$. Unlike vector triplet case, our model accept a potential composed of many terms coupling the new vector to the Higgs doublet with independent coupling constants. This feature makes the model more similar to the i2HDM than to models with vector triplets. Additionally, due to the quantum numbers assigned to the new vector, it is impossible to couple it to standard fermions through renormalizable operator. The model acquires a Z_2 symmetry in the limit in which the only non-standard dimension three operator is eliminated. This choice is natural in the sense of t'Hooft and allows the neutral vector V^1 to be a good dark matter candidate.

We have performed a detailed analysis constraining the model through LEP and LHC data, DM relic density and direct DM detection. We found that the main experimental constrains are imposed by recent measurement of $H \rightarrow \gamma\gamma$ (mainly when the V^1 is light) and data on direct search of DM obtained by XENON1T. After imposing all the experimental constraints, we found that for a range of masses between $840 \leq M_{V^1} \leq 10^4$ GeV in the highly degenerate case where $\Delta M < 20$ GeV the lightest neutral component of the doublet can reach the relic density measurements 5.28, surviving all the experimental constraints. This contrast with other electroweak vector multiplets models, where the saturation value for DM is above the TeV scale (see e.g. [45, 48]), or other models where the dark vector component never reach the DM budget (see e.g. [46, 47]). Furthermore, if we relax the lower PLANCK limit (5.28) allowing additional sources of dark matter, there is an important sector of the parameter space for $M_{V^1} \gtrsim 100$ GeV that it is still not possible to rule out with the current experiments.

At this point, we want to dedicate some sentences to compare our construction to the recently proposed Minimal Vector Dark Mater model (MVDM) [45]. In both models, the dark matter candidate is a component of a vector field transforming a non-trivial representation of $SU(2)_L$: the adjoint representation in the case of MVDM and the fundamental one in our case. The difference in representations makes an abysmal separation between the two models. The most evident one is related to the number of new vector states (3 for the MVDM and 4 in our case). But more important is what happen with the potential in the Higgs–massive-vector sector. In the MVDM this sector is extremely simple, contributing with only one term to the Lagrangian and only one of the two free parameters of the model. In our case, the scalar-vector potential is richer with three free parameters. This is, in part, the origin of the different ultra-violet behavior reflected in the scale of unitarity violation which is systematically larger in the MVDM. In fact, the structure of the potential of our model makes it more closely related to the i2HDM than to

the MVDM making harder to differentiate our model from the former than from the latter.

In view of the similarities between i2HDM with our model, we compared the parton level cross section and the normalized missing energy differential cross section for mono- $X(\text{jet}, Z, H)$. Mono- X cross section get enhanced in the vectorial case due to their growing energy behaviour of their final state longitudinal polarization. The shapes of the distribution of missing energy results to be flatter in the vectorial cases. This feature may help to distinguish between our model and the i2HDM.

Finally, as a complement to this work, we have shown some results of perturbative unitarity bounds on some scattering amplitudes involving the new states. Our analysis suggest that our effective approach needs an ultraviolet completion at a scale of the order of 3 to 10 TeV.

Inert Two Higgs Doublet Model

The i2HDM is considered one of the most simple extensions to the Standard Model. It consists in the addition of a second scalar ϕ_2 which is a $SU(2)_L$ doublet with hypercharge 1/2. In the unitary gauge, the doublets are

$$\phi_1 = \frac{1}{\sqrt{2}} \begin{pmatrix} 0 \\ v + H \end{pmatrix}, \quad \phi_2 = \frac{1}{\sqrt{2}} \begin{pmatrix} h^+ \\ h_1 + ih_2 \end{pmatrix}, \quad (\text{A.1})$$

where only the neutral component ϕ_1 gets a vacuum expectation value (vev). Due to an imposed Z_2 discrete symmetry, the second scalar doublet transform as

$$\phi_2 \rightarrow -\phi_2, \quad (\text{A.2})$$

with all other fields invariant. This parity imposes natural flavor conservation in the Higgs sector, implying that only ϕ_1 couples to matter.

The Lagrangian of the model is given by

$$\mathcal{L} = |D_\mu \phi_1|^2 + |D_\mu \phi_2|^2 - V(\phi_1, \phi_2), \quad (\text{A.3})$$

with the most general potential

$$\begin{aligned} V(\phi_1, \phi_2) = & -m_1^2 (\phi_1^\dagger \phi_1) - m_2^2 (\phi_2^\dagger \phi_2) + \lambda_1 (\phi_1^\dagger \phi_1)^2 + \lambda_2 (\phi_2^\dagger \phi_2)^2 \\ & + \lambda_3 (\phi_1^\dagger \phi_1) (\phi_2^\dagger \phi_2) + \lambda_4 (\phi_2^\dagger \phi_1) (\phi_1^\dagger \phi_2) + \frac{\lambda_5}{2} \left[(\phi_1^\dagger \phi_2)^2 + (\phi_2^\dagger \phi_1)^2 \right]. \end{aligned} \quad (\text{A.4})$$

The parameter space of the model is relatively small, and typically they are taken as real parameters in order to precludes the CP-violation.

After electroweak symmetry breaking (EWSB) the scalar mass spectrum is given by

$$M_H^2 = 2\lambda_1 v^2, \quad (\text{A.5})$$

$$M_{h^\pm}^2 = \frac{1}{2} [2m_2^2 - \lambda_3 v^2], \quad (\text{A.6})$$

$$M_{h_1}^2 = \frac{1}{2} [2m_2^2 - (\lambda_3 + \lambda_4 + \lambda_5) v^2], \quad (\text{A.7})$$

$$M_{h_2}^2 = \frac{1}{2} [(2m_2^2 - \lambda_3 + \lambda_4 - \lambda_5) v^2], \quad (\text{A.8})$$

where we recognize the H state as the 126 GeV Higgs boson, and the rest as the new scalars. Without loss of generality, the lightest odd particle is considered to be h_1 . A phenomenological

important consequence of the Z_2 symmetry is that the Z_2 -odd particle (LOP) is stable. If further the LOP is either h_1 or h_2 , this (neutral) state can play the role of the DM candidate. The coupling combination $\lambda_3 + \lambda_4 + \lambda_5 \equiv \lambda_{345}$ plays an important phenomenological role, as it governs the Higgs-DM interaction vertex Hh_1h_1 , (see Fig. A.1).

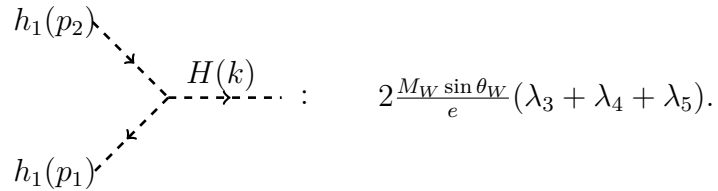


FIGURE A.1: Tree level coupling between the LOP (DM candidate) and the Higgs Boson.

Vector fields and polarizations

In this appendix we are interested to review the high energy behaviour of vector fields. To this end, we must focus in its equation of motion and polarizations.

The equation of motion of a massive free vector field is

$$\partial_\mu F^{\mu\nu} + M_V^2 V^\nu = 0, \quad (\text{B.1})$$

Derivating this equation one obtains the constraint $\partial_\mu V^\mu = 0$. Including this condition in B.1 we obtain the Proca or Klein-Gordon equation for each component

$$(\square + M_V^2)V_\mu = 0. \quad (\text{B.2})$$

The solution to this equation can be written as

$$V_\mu = \sum_i \int \frac{d^3p}{(2\pi)^3} a_i(\vec{p}) \epsilon_\mu^i(p) e^{ipx}, \quad \text{with} \quad p_0 \equiv E = \sqrt{\vec{p}^2 + m^2} \quad (\text{B.3})$$

where ϵ_μ^i is the base four-vector polarization. The i index is undefined, but usually in Minkowsky spacetime is chosen a four dimensional base, i.e., $i = 1, \dots, 4$. Note that the constraint $\partial_\mu V^\mu = 0$ implies $p_\mu \epsilon^{i,\mu}(p) = 0$, for all i , then resulting in three independent polarization vectors. Usually, they are normalized to $\epsilon_\mu^* \epsilon^\mu = -1$.

In the gauge boson rest frame, where $p^\mu = (M_V, 0, 0, 0)$, the longitudinal polarization vector is

$$\epsilon_L^\mu(p) = (0, 0, 0, 1), \quad \text{satisfying} \quad \epsilon_L(p) \cdot \epsilon_L(p) = -1 \quad \text{and} \quad p \cdot \epsilon_L(p) = 0$$

Now let boost the boson. In a gauge boson moving frame (z^+ -axis), the massive vector field has $p^\mu = (E, 0, 0, p_z)$. The vector polarizations can be written as the following: $\epsilon_{T1}^\mu = (0, 1, 0, 0)$, $\epsilon_{T2}^\mu = (0, 0, 1, 0)$ and $\epsilon_L^\mu = \frac{1}{M_V}(p_z, 0, 0, E)$. As the longitudinal polarization depends on the energy, at high energies it behaves as $\epsilon_L^\mu \rightarrow \frac{p^\mu}{M_V} = \frac{E}{M_V}(1, 0, 0, 1)$, which is the origin of dangerous $\frac{E^2}{M_V^2}$ growing amplitudes. However, this is just an approximation since it violates $\epsilon \cdot p = 0$, and actually the expression at high energies is

$$\epsilon_L^\mu(p) = \frac{p^\mu}{M_V} + \mathcal{O}\left(\frac{M_V}{E}\right) \quad (\text{B.4})$$

To be even more general, let us take the gauge boson moving in some arbitrary direction with velocity $\vec{\beta}$. The four-momentum is $p^\mu = E(1, \vec{\beta})$ and it is possible to write the longitudinal

polarization as

$$\epsilon_L^\mu(p) = (\gamma\beta, \gamma\hat{\beta}) \quad (\text{B.5})$$

where $\vec{\beta} = \vec{p}/E$, $\gamma^{-1} = \sqrt{1 - \beta^2} = M_V/E$ and $\hat{\beta} = \vec{\beta}/\beta$. It is easy to check that this form of ϵ_L satisfy the invariant relations $p \cdot \epsilon_L(p) = 0$ and $\epsilon_\mu^* \epsilon^\mu = -1$. In fact, one can show that a better approximation is

$$\epsilon_L^\mu(p) = \frac{p^\mu}{M_V} + \frac{1}{2\gamma^2} \frac{Q^\mu}{M_V} + \dots \quad (\text{B.6})$$

where $Q^\mu = (-E, \vec{p})$. The second term it is suppressed by the energy $\mathcal{O}(M_V/E)$.

Taking into account these considerations in the longitudinal polarizations, there are potentially dangerous growing amplitudes when we consider the scattering of at least two longitudinally polarized gauge bosons. The contraction of their polarization vectors grows as

$$\epsilon_L(p_i) \cdot \epsilon_L(p_j) \cong \frac{s}{2m_i m_j} \gg 1 \quad \text{for} \quad \sqrt{s} \gg m_i, m_j, \quad i \neq j \quad (\text{B.7})$$

in the s channel.

Partial wave amplitudes

Having shown that our model can provide a viable Dark Matter candidate, we want to discuss the validity range of our effective approach. The main theoretical challenge faced by our construction is the eventual violation of perturbative unitarity introduced by the new massive vector states. To this aim, we study the amplitudes, in the high energy regime, of representative and potentially problematic processes like $hV^1 \rightarrow hV^1$ and $ZV^\pm \rightarrow ZV^\pm$. In order to quantify the loss of perturbative unitarity, we decompose the scattering amplitude in terms of partial waves, and then we impose the constraint on it from unitarity principles.

The scattering amplitude can be decomposed in partial waves as

$$\mathcal{M}(s, \theta) = 32\pi \sum_{l=0}^{\infty} (2l+1) a_l P_l(\cos \theta), \quad (\text{C.1})$$

where $P_l(\cos \theta)$ correspond to the Legendre polynomials and s correspond to the center-of-momentum energy, the l -th partial-wave amplitude is given by

$$a_l = \frac{1}{32\pi} \int_{-1}^1 d(\cos \theta) \mathcal{M}(s, \theta) P_l(\cos \theta). \quad (\text{C.2})$$

Denoting each elastic process as $X_1 X_2 \rightarrow X_1 X_2$, where $X_{1,2}$ is one of the particles in the processes of interest, and defining $x \equiv s/(4M_{X_1} M_{X_2})$, the high energy regime is for $x \gg 1$, and in this limit the scattering amplitude can be written as an expansion in x as the following¹

$$\mathcal{M} = Ax^2 + Bx + C + \mathcal{O}(1/x), \quad (\text{C.3})$$

where the coefficients A, B and C can have an angular dependence. Only considering the $l = 0$ (which give the leading contributions), perturbative unitarity set that

$$|a_0(x)| \leq 1. \quad (\text{C.4})$$

In Fig.C.1(a) is shown the maximum energy scale at which the process $hV^1 \rightarrow hV^1$ is valid until perturbative unitarity starts to be violated². As λ_L gets smaller the bigger is the scale energy before the breaking of perturbative unitarity. Additionally, the bound on the energy gets relax as M_{V^1} raises too. For values of M_{V^1} below 100 GeV the scale of unitarity violation is mostly constant and of the order of a few TeV s, whereas for higher masses the dependence on λ_L start to grow, making our model consistent at scales as high as 10 TeV for small values of λ_L . Therefore, from the point of view of unitarity, our construction is perfectly safe for masses of the DM candidate above 200 GeV specially when λ_L to is small. We want to remark that

¹We follow the procedure exposed in [75].

²The explicit expressions of the partial waves are in the Appendix.

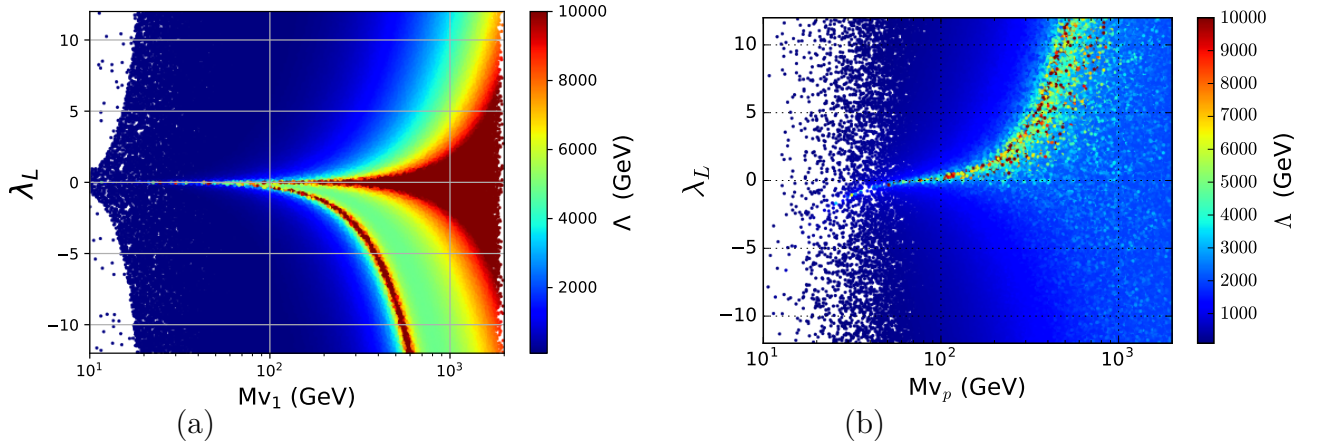


FIGURE C.1: a) Maximum energy-scale Λ until the process $hV^1 \rightarrow hV^1$ starts to violate perturbative unitarity. b) Maximum energy-scale Λ until the process $ZV^\pm \rightarrow ZV^\pm$ starts to violate perturbative unitarity.

phenomenologically interesting region of the space parameter, where our DM candidate saturate the relic density, belongs to the unitarity safe zone.

In Fig. C.1(b) is shown the maximum energy scale in the plane (λ_L, M_{V^\pm}) at which the process $Z_L V_L^\pm \rightarrow Z_L V_L^\pm$ is valid until perturbative unitarity is violated. At masses near 100 GeV and λ_L close to zero, the maximum energy values allowed by perturbative unitarity rises easily above 5 TeV. on the other hand, for values of M_{V^\pm} near 1 TeV, the scale of unitarity violation is of the order of 3 TeV.

These results are consistent with unitarity analysis of some vector dark matter models [30, 45] and suggest that our effective model must meet an ultraviolet completion at a scale between 3 and 10 TeV. For instance, one of the simplest ways to restore unitarity is to embed our model into a larger gauge symmetry spontaneously broken by a new scalar sector [76]. In this sense, our model can be considered as a simplified model [23], retaining just the lightest states predicted in this scenario, and pushing the required new states at scales above the vectorial ones.

Complementary to the the results presented above, we present the results of the same processes but in different planes.

In Fig. C.2 is shown the value of the scale of perturbative unitarity violation (Λ) for the process $hV^1 \rightarrow hV^1$ in the planes (M_{V1}, M_{V2}) , (M_{V1}, M_{V^\pm}) and (M_{V2}, M_{V^\pm}) , respectively. In table(C.1) we resume the zero partial wave for the three possibles elastic scattering of this type. In concordance with the information given by Fig. C.1(a), for lower masses ($\lesssim 200$ GeV), the values of Λ are located around the TeV energy scale for most of the masses combinations allowed by experimental constrains. For higher masses, Λ starts to grow for most of possible combination of masses, and there is a slightly raising in the energy as the degeneracy among the three states becomes similar.

On the other hand, in Fig. C.3 we present different plots showing the values of Λ for the process $ZV^\pm \rightarrow ZV^\pm$. In this case, the degeneracy of the states do not show any raising in the maximum allowed energy value. According to what is shown in Fig. C.1(b), as the masses get near the TeV scale, Λ gets a constant value near 4 TeV, making this process more stringent for masses above ~ 500 GeV than the previous one with the Higgs involved.

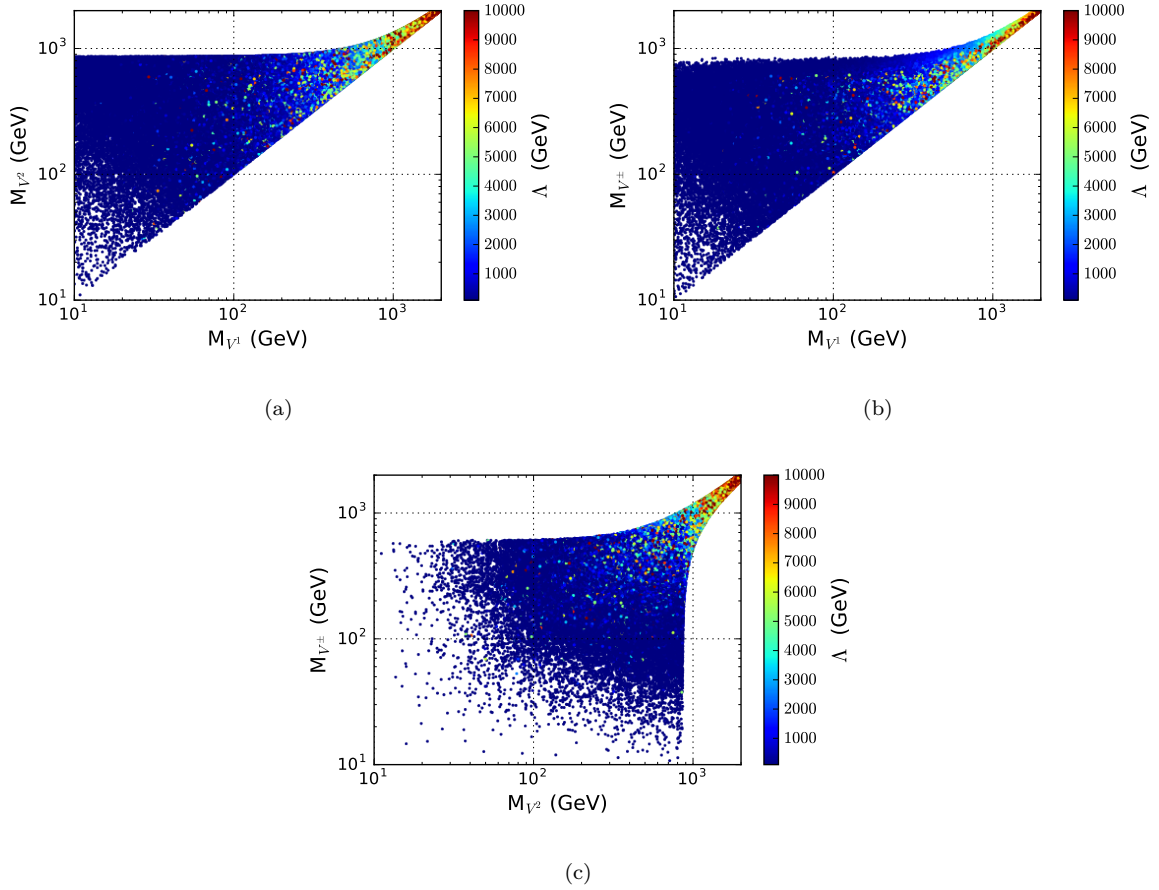


FIGURE C.2: Maximum allowed energy Λ by perturbative unitarity bounds on $hV^1 \rightarrow hV^1$ amplitude. The plots are projected in the planes (M_{V^1}, M_{V^2}) (a), (M_{V^1}, M_{V^\pm}) (b) and (M_{V^2}, M_{V^\pm}) (c).

Finally, we make some comments about the $V_L + V_L \rightarrow V_L + V_L$ amplitudes, for $V = V^1, V^2$ and V^\pm . These processes may introduce strong constraints on the energy scale at which perturbative unitarity breaks down. For example, let us first consider the process $V_L^1 + V_L^1 \rightarrow V_L^1 + V_L^1$. Its zero partial wave is

$$a_0(s) = \frac{g^2(\alpha_2 + \alpha_3)(36M_{V^1}^4 - 24M_{V^1}^2s + 5s^2) + 18\lambda_L^2 M_H^2 M_W^2}{96\pi g^2 M_{V^1}^4}, \quad (\text{C.5})$$

where α_2 and α_3 are the self-couplings among the new states (see (4.9)). The strong growing energy behaviour of the partial wave ($a_0 \sim E^4$) makes that perturbative unitarity breaks down at very low energies for typical masses of a few hundred GeV. For example, for $M_{V^1} = 100$ GeV, $\lambda_L = 1$ and for $\alpha_2 = \alpha_3 = 1$, the breaking of perturbative unitarity is reached at center of mass energies less than 250 GeV. Interestingly, the growing energy behaviour disappears when $\alpha_2 = -\alpha_3$. However, under this last condition, the $V_L^+ + V_L^- \rightarrow V_L^+ + V_L^-$ amplitude still grows with the energy as E^4

$$a_0(s) = \frac{g^2(9(1 - 2c_w^2)^2 M_W^2 s - 4c_w^2 s^2)}{1536\pi c_w^4 M_{V^\pm}^4} + \frac{M_W^2 \lambda_2 s}{32\pi g^2 M_{V^\pm}^4}, \quad (\text{C.6})$$

where λ_2 is a function of λ_L , M_{V^1} and M_{V^\pm} (see eq. (4.16)). Even when the partial wave still grows with the energy, the loss of perturbative unitarity is not as strong as it is in the channels

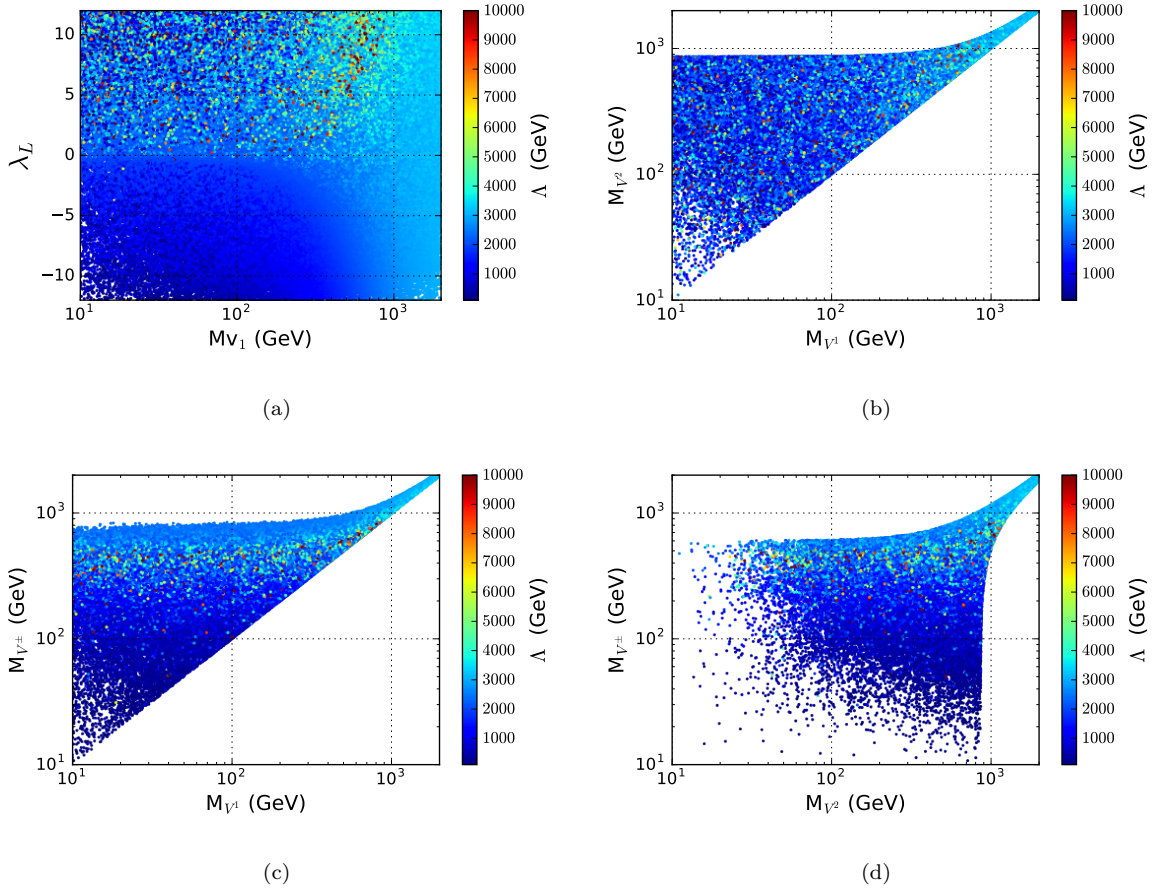


FIGURE C.3: Maximum allowed energy Λ from perturbative unitarity bounds on the processes $ZV^\pm \rightarrow ZV^\pm$ in the planes (a) (M_{V1}, M_{V2}) , (b) (M_{V1}, M_{V^\pm}) and (c) (M_{V2}, M_{V^\pm}) .

which involves a SM gauge boson. Finally, it seems impossible to get rid of the growing energy behaviour with an arbitrarily choose of the free parameters. As we have pointed out above, a possible solution to this problem is to establish the model from a gauge theory in order to generate a gauge cancellation among the s - and t - channels and the contact graph [77].

TABLE C.1: Partial waves for $hV \rightarrow hV$ elastic tree level scatterings processes. Each of the three processes contain a contact diagram.

Process	s-cha	t-cha	Partial wave (a_0)
$hV^1 \rightarrow hV^1$	V^1	H, V^1	$-\frac{\lambda_L s}{64\pi M_{V^1}^2} \left(1 + 2 \frac{\lambda_L}{g^2} \frac{M_W^2}{M_{V^1}^2} \right)$
$hV^2 \rightarrow hV^2$	V^2	H, V^2	$-\frac{\lambda_R s}{64\pi M_{V^2}^2} \left(1 + 2 \frac{\lambda_R}{g^2} \frac{M_W^2}{M_{V^2}^2} \right)$
$hV^\pm \rightarrow hV^\pm$	V^\pm	H, V^\pm	$-\frac{\lambda_2 s}{64\pi M_{V^\pm}^2} \left(1 + 2 \frac{\lambda_2}{g^2} \frac{M_W^2}{M_{V^\pm}^2} \right)$

Bibliography

- [1] W. Buchmuller, R. Ruckl, and D. Wyler, “Leptoquarks in Lepton - Quark Collisions,” [*Phys. Lett.* **B191** \(1987\) 442–448](#). [Erratum: *Phys. Lett.*B448,320(1999)].
- [2] **Particle Data Group** Collaboration, M. Tanabashi *et al.*, “Review of Particle Physics,” [*Phys. Rev.* **D98** no. 3, \(2018\) 030001](#).
- [3] B. Diaz, M. Schmaltz, and Y.-M. Zhong, “The leptoquark Hunter’s guide: Pair production,” [*JHEP* **10** \(2017\) 097](#), [arXiv:1706.05033 \[hep-ph\]](#).
- [4] G. Bertone, D. Hooper, and J. Silk, “Particle dark matter: Evidence, candidates and constraints,” [*Phys. Rept.* **405** \(2005\) 279–390](#), [arXiv:hep-ph/0404175 \[hep-ph\]](#).
- [5] A. C. Fabian and S. W. Allen, “X-rays from clusters of galaxies,” in *Proceedings, 21st Texas Symposium on Relativistic Astrophysics (Texas in Tuscany): Florence, Italy*, pp. 197–208. 2003. [arXiv:astro-ph/0304020 \[astro-ph\]](#).
- [6] **WMAP** Collaboration, G. Hinshaw *et al.*, “Nine-Year Wilkinson Microwave Anisotropy Probe (WMAP) Observations: Cosmological Parameter Results,” [*Astrophys. J. Suppl.* **208** \(2013\) 19](#), [arXiv:1212.5226 \[astro-ph.CO\]](#).
- [7] **XENON** Collaboration, E. Aprile *et al.*, “Dark Matter Search Results from a One Ton-Year Exposure of XENON1T,” [*Phys. Rev. Lett.* **121** no. 11, \(2018\) 111302](#), [arXiv:1805.12562 \[astro-ph.CO\]](#).
- [8] U. Haisch, F. Kahlhoefer, and E. Re, “QCD effects in mono-jet searches for dark matter,” [*JHEP* **12** \(2013\) 007](#), [arXiv:1310.4491 \[hep-ph\]](#).
- [9] F. Kahlhoefer, “Review of LHC Dark Matter Searches,” [*Int. J. Mod. Phys.* **A32** no. 13, \(2017\) 1730006](#), [arXiv:1702.02430 \[hep-ph\]](#).
- [10] **ATLAS** Collaboration, G. Aad *et al.*, “Search for invisible decays of a Higgs boson using vector-boson fusion in pp collisions at $\sqrt{s} = 8$ TeV with the ATLAS detector,” [*JHEP* **01** \(2016\) 172](#), [arXiv:1508.07869 \[hep-ex\]](#).
- [11] **CMS** Collaboration, V. Khachatryan *et al.*, “Searches for invisible decays of the Higgs boson in pp collisions at $\sqrt{s} = 7, 8,$ and 13 TeV,” [*JHEP* **02** \(2017\) 135](#), [arXiv:1610.09218 \[hep-ex\]](#).
- [12] M. Beltran, D. Hooper, E. W. Kolb, Z. A. C. Krusberg, and T. M. P. Tait, “Maverick dark matter at colliders,” [*JHEP* **09** \(2010\) 037](#), [arXiv:1002.4137 \[hep-ph\]](#).
- [13] Y. Bai, P. J. Fox, and R. Harnik, “The Tevatron at the Frontier of Dark Matter Direct Detection,” [*JHEP* **12** \(2010\) 048](#), [arXiv:1005.3797 \[hep-ph\]](#).

- [14] A. L. Fitzpatrick, W. Haxton, E. Katz, N. Lubbers, and Y. Xu, “The Effective Field Theory of Dark Matter Direct Detection,” [*JCAP* **1302** \(2013\) 004](#), [arXiv:1203.3542 \[hep-ph\]](#).
- [15] G. Busoni, A. De Simone, E. Morgante, and A. Riotto, “On the Validity of the Effective Field Theory for Dark Matter Searches at the LHC,” [*Phys. Lett.* **B728** \(2014\) 412–421](#), [arXiv:1307.2253 \[hep-ph\]](#).
- [16] G. Busoni, A. De Simone, J. Gramling, E. Morgante, and A. Riotto, “On the Validity of the Effective Field Theory for Dark Matter Searches at the LHC, Part II: Complete Analysis for the s -channel,” [*JCAP* **1406** \(2014\) 060](#), [arXiv:1402.1275 \[hep-ph\]](#).
- [17] A. Belyaev, L. Panizzi, A. Pukhov, and M. Thomas, “Dark Matter characterization at the LHC in the Effective Field Theory approach,” [*JHEP* **04** \(2017\) 110](#), [arXiv:1610.07545 \[hep-ph\]](#).
- [18] P. J. Fox, R. Harnik, J. Kopp, and Y. Tsai, “Missing energy signatures of dark matter at the lhc,” [*Phys. Rev. D* **85** \(Mar, 2012\) 056011](#).
<https://link.aps.org/doi/10.1103/PhysRevD.85.056011>.
- [19] A. Rajaraman, W. Shepherd, T. M. P. Tait, and A. M. Wijangco, “Lhc bounds on interactions of dark matter,” [*Phys. Rev. D* **84** \(Nov, 2011\) 095013](#).
<https://link.aps.org/doi/10.1103/PhysRevD.84.095013>.
- [20] M. R. Buckley, D. Feld, and D. Goncalves, “Scalar Simplified Models for Dark Matter,” [*Phys. Rev.* **D91** \(2015\) 015017](#), [arXiv:1410.6497 \[hep-ph\]](#).
- [21] O. Buchmueller, M. J. Dolan, and C. McCabe, “Beyond Effective Field Theory for Dark Matter Searches at the LHC,” [*JHEP* **01** \(2014\) 025](#), [arXiv:1308.6799 \[hep-ph\]](#).
- [22] O. Buchmueller, M. J. Dolan, S. A. Malik, and C. McCabe, “Characterising dark matter searches at colliders and direct detection experiments: Vector mediators,” [*JHEP* **01** \(2015\) 037](#), [arXiv:1407.8257 \[hep-ph\]](#).
- [23] J. Abdallah et al., “Simplified Models for Dark Matter Searches at the LHC,” [*Phys. Dark Univ.* **9-10** \(2015\) 8–23](#), [arXiv:1506.03116 \[hep-ph\]](#).
- [24] J. Abdallah et al., “Simplified Models for Dark Matter and Missing Energy Searches at the LHC,” [arXiv:1409.2893 \[hep-ph\]](#).
- [25] M. Cirelli, N. Fornengo, and A. Strumia, “Minimal dark matter,” [*Nucl. Phys.* **B753** \(2006\) 178–194](#), [arXiv:hep-ph/0512090 \[hep-ph\]](#).
- [26] T. Hambye, “Hidden vector dark matter,” [*JHEP* **01** \(2009\) 028](#), [arXiv:0811.0172 \[hep-ph\]](#).
- [27] J. L. Diaz-Cruz and E. Ma, “Neutral SU(2) Gauge Extension of the Standard Model and a Vector-Boson Dark-Matter Candidate,” [*Phys. Lett.* **B695** \(2011\) 264–267](#), [arXiv:1007.2631 \[hep-ph\]](#).
- [28] S. Kanemura, S. Matsumoto, T. Nabeshima, and N. Okada, “Can WIMP Dark Matter overcome the Nightmare Scenario?,” [*Phys. Rev.* **D82** \(2010\) 055026](#), [arXiv:1005.5651 \[hep-ph\]](#).
- [29] A. Djouadi, O. Lebedev, Y. Mambrini, and J. Quevillon, “Implications of LHC searches for Higgs-portal dark matter,” [*Phys. Lett.* **B709** \(2012\) 65–69](#), [arXiv:1112.3299 \[hep-ph\]](#).

-
- [30] O. Lebedev, H. M. Lee, and Y. Mambrini, “Vector Higgs-portal dark matter and the invisible Higgs,” *Phys. Lett.* **B707** (2012) 570–576, [arXiv:1111.4482 \[hep-ph\]](#).
- [31] Y. Farzan and A. R. Akbarieh, “VDM: A model for Vector Dark Matter,” *JCAP* **1210** (2012) 026, [arXiv:1207.4272 \[hep-ph\]](#).
- [32] S. Baek, P. Ko, W.-I. Park, and E. Senaha, “Higgs Portal Vector Dark Matter : Revisited,” *JHEP* **05** (2013) 036, [arXiv:1212.2131 \[hep-ph\]](#).
- [33] J.-H. Yu, “Vector Fermion-Portal Dark Matter: Direct Detection and Galactic Center Gamma-Ray Excess,” *Phys. Rev.* **D90** no. 9, (2014) 095010, [arXiv:1409.3227 \[hep-ph\]](#).
- [34] C. Gross, O. Lebedev, and Y. Mambrini, “Non-Abelian gauge fields as dark matter,” *JHEP* **08** (2015) 158, [arXiv:1505.07480 \[hep-ph\]](#).
- [35] S. Di Chiara and K. Tuominen, “A minimal model for SU(N) vector dark matter,” *JHEP* **11** (2015) 188, [arXiv:1506.03285 \[hep-ph\]](#).
- [36] R. Catena and L. Covi, “SUSY dark matter(s),” *Eur. Phys. J.* **C74** (2014) 2703, [arXiv:1310.4776 \[hep-ph\]](#).
- [37] G. Servant and T. M. P. Tait, “Is the lightest Kaluza-Klein particle a viable dark matter candidate?,” *Nucl. Phys.* **B650** (2003) 391–419, [arXiv:hep-ph/0206071 \[hep-ph\]](#).
- [38] A. Birkedal, A. Noble, M. Perelstein, and A. Spray, “Little Higgs dark matter,” *Phys. Rev.* **D74** (2006) 035002, [arXiv:hep-ph/0603077 \[hep-ph\]](#).
- [39] T. Abe, M. Kakizaki, S. Matsumoto, and O. Seto, “Vector WIMP Miracle,” *Phys. Lett.* **B713** (2012) 211–215, [arXiv:1202.5902 \[hep-ph\]](#).
- [40] G. Busoni, A. De Simone, T. Jacques, E. Morgante, and A. Riotto, “Making the Most of the Relic Density for Dark Matter Searches at the LHC 14 TeV Run,” *JCAP* **1503** no. 03, (2015) 022, [arXiv:1410.7409 \[hep-ph\]](#).
- [41] U. Haisch, F. Kahlhoefer, and T. M. P. Tait, “On Mono-W Signatures in Spin-1 Simplified Models,” *Phys. Lett.* **B760** (2016) 207–213, [arXiv:1603.01267 \[hep-ph\]](#).
- [42] R. D. Young and A. W. Thomas, “Octet baryon masses and sigma terms from an SU(3) chiral extrapolation,” *Phys. Rev.* **D81** (2010) 014503, [arXiv:0901.3310 \[hep-lat\]](#).
- [43] **Planck** Collaboration, P. Ade et al., “Planck 2015 results. XIII. Cosmological parameters,” [arXiv:1502.01589 \[astro-ph.CO\]](#).
- [44] J. McKay, *Constraining dark matter with renormalisation and global fits*. PhD thesis, Imperial Coll., London, 2018. <https://spiral.imperial.ac.uk/handle/10044/1/62642>.
- [45] A. Belyaev, G. Cacciapaglia, J. McKay, D. Marin, and A. R. Zerwekh, “Minimal Spin-one Isotriplet Dark Matter,” [arXiv:1808.10464 \[hep-ph\]](#).
- [46] J. K. Mizukoshi, C. A. de S. Pires, F. S. Queiroz, and P. S. Rodrigues da Silva, “WIMPs in a 3-3-1 model with heavy Sterile neutrinos,” *Phys. Rev.* **D83** (2011) 065024, [arXiv:1010.4097 \[hep-ph\]](#).
- [47] P. V. Dong, D. T. Huong, F. S. Queiroz, J. W. F. Valle, and C. A. Vaquera-Araujo, “The Dark Side of Flipped Trinification,” *JHEP* **04** (2018) 143, [arXiv:1710.06951 \[hep-ph\]](#).

- [48] N. Maru, N. Okada, and S. Okada, “ $SU(2)_L$ Doublet Vector Dark Matter from Gauge-Higgs Unification,” [arXiv:1803.01274 \[hep-ph\]](#).
- [49] M. V. Chizhov and G. Dvali, “Origin and Phenomenology of Weak-Doublet Spin-1 Bosons,” [Phys. Lett. **B703** \(2011\) 593–598](#), [arXiv:0908.0924 \[hep-ph\]](#).
- [50] J. L. Hewett, T. G. Rizzo, S. Pakvasa, H. E. Haber, and A. Pomarol, “Vector leptoquark production at hadron colliders,” in [Workshop on Physics at Current Accelerators and the Supercollider Argonne, Illinois, June 2-5, 1993](#), pp. 0539–546. 1993. [arXiv:hep-ph/9310361 \[hep-ph\]](#).
- [51] S. Tulin and H.-B. Yu, “Dark Matter Self-interactions and Small Scale Structure,” [Phys. Rept. **730** \(2018\) 1–57](#), [arXiv:1705.02358 \[hep-ph\]](#).
- [52] R. Barbieri, L. J. Hall, and V. S. Rychkov, “Improved naturalness with a heavy Higgs: An Alternative road to LHC physics,” [Phys. Rev. **D74** \(2006\) 015007](#), [arXiv:hep-ph/0603188 \[hep-ph\]](#).
- [53] L. Lopez Honorez, E. Nezri, J. F. Oliver, and M. H. G. Tytgat, “The Inert Doublet Model: An Archetype for Dark Matter,” [JCAP **0702** \(2007\) 028](#), [arXiv:hep-ph/0612275 \[hep-ph\]](#).
- [54] A. Belyaev, G. Cacciapaglia, I. P. Ivanov, F. Rojas-Abatte, and M. Thomas, “Anatomy of the Inert Two Higgs Doublet Model in the light of the LHC and non-LHC Dark Matter Searches,” [Phys. Rev. **D97** no. 3, \(2018\) 035011](#), [arXiv:1612.00511 \[hep-ph\]](#).
- [55] A. Semenov, “LanHEP - a package for automatic generation of Feynman rules from the Lagrangian. Updated version 3.1,” [arXiv:1005.1909 \[hep-ph\]](#).
- [56] A. Belyaev, N. D. Christensen, and A. Pukhov, “CalcHEP 3.4 for collider physics within and beyond the Standard Model,” [Comput. Phys. Commun. **184** \(2013\) 1729–1769](#), [arXiv:1207.6082 \[hep-ph\]](#).
- [57] G. Belanger, F. Boudjema, A. Pukhov, and A. Semenov, “micrOMEGAs_3: A program for calculating dark matter observables,” [Comput. Phys. Commun. **185** \(2014\) 960–985](#), [arXiv:1305.0237 \[hep-ph\]](#).
- [58] G. Belanger, F. Boudjema, A. Pukhov, and A. Semenov, “MicrOMEGAs 2.0: A Program to calculate the relic density of dark matter in a generic model,” [Comput. Phys. Commun. **176** \(2007\) 367–382](#), [arXiv:hep-ph/0607059 \[hep-ph\]](#).
- [59] G. Belanger, F. Boudjema, P. Brun, A. Pukhov, S. Rosier-Lees, P. Salati, and A. Semenov, “Indirect search for dark matter with micrOMEGAs2.4,” [Comput. Phys. Commun. **182** \(2011\) 842–856](#), [arXiv:1004.1092 \[hep-ph\]](#).
- [60] Q.-H. Cao, E. Ma, and G. Rajasekaran, “Observing the Dark Scalar Doublet and its Impact on the Standard-Model Higgs Boson at Colliders,” [Phys. Rev. **D76** \(2007\) 095011](#), [arXiv:0708.2939 \[hep-ph\]](#).
- [61] M. Gustafsson, E. Lundstrom, L. Bergstrom, and J. Edsjo, “Significant Gamma Lines from Inert Higgs Dark Matter,” [Phys. Rev. Lett. **99** \(2007\) 041301](#), [arXiv:astro-ph/0703512 \[ASTRO-PH\]](#).
- [62] E. Lundström, M. Gustafsson, and J. Edsjö, “Inert doublet model and lep ii limits,” [Phys. Rev. **D 79** \(Feb, 2009\) 035013](#). <https://link.aps.org/doi/10.1103/PhysRevD.79.035013>.

-
- [63] A. Pierce and J. Thaler, “Natural Dark Matter from an Unnatural Higgs Boson and New Colored Particles at the TeV Scale,” *JHEP* **08** (2007) 026, [arXiv:hep-ph/0703056 \[HEP-PH\]](#).
- [64] **DELPHI** Collaboration, P. Abreu *et al.*, “Search for neutralino pair production at $s^{*(1/2)} = 189\text{-GeV}$,” *Eur. Phys. J.* **C19** (2001) 201–212, [arXiv:hep-ex/0102034 \[hep-ex\]](#).
- [65] **OPAL** Collaboration, G. Abbiendi *et al.*, “Search for chargino and neutralino production at $S^{*(1/2)} = 189\text{-GeV}$ at LEP,” *Eur. Phys. J.* **C14** (2000) 187–198, [arXiv:hep-ex/9909051 \[hep-ex\]](#). [Erratum: *Eur. Phys. J.* **C16**,707(2000)].
- [66] **ATLAS** Collaboration, M. Aaboud *et al.*, “Measurements of Higgs boson properties in the diphoton decay channel with 36 fb^{-1} of pp collision data at $\sqrt{s} = 13\text{ TeV}$ with the ATLAS detector,” [arXiv:1802.04146 \[hep-ex\]](#).
- [67] W. J. Marciano, C. Zhang, and S. Willenbrock, “Higgs Decay to Two Photons,” *Phys. Rev.* **D85** (2012) 013002, [arXiv:1109.5304 \[hep-ph\]](#).
- [68] A. Belyaev, T. R. Fernandez Perez Tomei, P. G. Mercadante, C. S. Moon, S. Moretti, S. F. Novaes, L. Panizzi, F. Rojas, and M. Thomas, “Advancing LHC Probes of Dark Matter from the Inert 2-Higgs Doublet Model with the Mono-jet Signal,” [arXiv:1809.00933 \[hep-ph\]](#).
- [69] **Planck** Collaboration, P. A. R. Ade *et al.*, “Planck 2013 results. XVI. Cosmological parameters,” *Astron. Astrophys.* **571** (2014) A16, [arXiv:1303.5076 \[astro-ph.CO\]](#).
- [70] **XENON** Collaboration, E. Aprile *et al.*, “First Dark Matter Search Results from the XENON1T Experiment,” *Phys. Rev. Lett.* **119** no. 18, (2017) 181301, [arXiv:1705.06655 \[astro-ph.CO\]](#).
- [71] N. G. Deshpande and E. Ma, “Pattern of symmetry breaking with two higgs doublets,” *Phys. Rev. D* **18** (Oct, 1978) 2574–2576. <https://link.aps.org/doi/10.1103/PhysRevD.18.2574>.
- [72] A. Goudelis, B. Herrmann, and O. Stal, “Dark matter in the Inert Doublet Model after the discovery of a Higgs-like boson at the LHC,” *JHEP* **09** (2013) 106, [arXiv:1303.3010 \[hep-ph\]](#).
- [73] A. Arhrib, Y.-L. S. Tsai, Q. Yuan, and T.-C. Yuan, “An Updated Analysis of Inert Higgs Doublet Model in light of the Recent Results from LUX, PLANCK, AMS-02 and LHC,” *JCAP* **1406** (2014) 030, [arXiv:1310.0358 \[hep-ph\]](#).
- [74] A. Ilnicka, M. Krawczyk, and T. Robens, “Inert Doublet Model in light of LHC Run I and astrophysical data,” *Phys. Rev.* **D93** no. 5, (2016) 055026, [arXiv:1508.01671 \[hep-ph\]](#).
- [75] J. C. Romão, “The need for the Higgs boson in the Standard Model,” 2016. [arXiv:1603.04251 \[hep-ph\]](#). <https://inspirehep.net/record/1427433/files/arXiv:1603.04251.pdf>.
- [76] F. Kahlhoefer, K. Schmidt-Hoberg, T. Schwetz, and S. Vogl, “Implications of unitarity and gauge invariance for simplified dark matter models,” *JHEP* **02** (2016) 016, [arXiv:1510.02110 \[hep-ph\]](#).
- [77] B. W. Lee, C. Quigg, and H. B. Thacker, “Weak Interactions at Very High-Energies: The Role of the Higgs Boson Mass,” *Phys. Rev.* **D16** (1977) 1519.